Fluxon readout for superconducting flux qubits

Zur Erlangung des akademischen Grades eines
DOKTORS DER NATURWISSENSCHAFTEN
von der Fakultät für Physik des
Karlsruher Institut für Technologie (KIT)

genehmigte

DISSERTATION

von

M. Sc. Kirill Fedorov
aus Nizhny Novgorod

Tag der mündlichen Prüfung: 26.04.2013

Referent: Prof. Dr. Alexey Ustinov

Koreferent: Prof. Dr. Wulf Wulfhekel

Contents

Introduction **1**

1 From zero-resistivity to Josephson vortices **5**
1.1 Quantum mechanics and superconductivity phenomenon 5
1.1.1 Zero resistivity and Meissner effect 5
1.1.2 Theory of superconductivity 6
1.1.3 Flux quantization 13
1.2 Josephson effect 14
1.2.1 Semi-phenomenological approach 15
1.2.2 Microscopic approach 17
1.3 Conclusions 18

2 On fluxons and flux qubits **19**
2.1 Fluxons 19
2.1.1 RSCJ model 19
2.1.2 sine-Gordon equation 21
2.1.3 Josephson vortices 25
2.1.4 Excitations in long Josephson junctions 26
2.1.5 Dynamics of fluxons 28
2.1.6 Detecting a fluxon 31
2.1.7 Creating a fluxon in annular Josephson junctions 33
2.1.8 Resonant modes in long Josephson junctions . . 34
2.2 Flux Qubit 37
2.2.1 Quantum bits and quantum computing 37
2.2.2 Persistent current qubit 38
2.2.3 Flux Qubit Potential 39
2.2.4 Quantum mechanical description 40
2.2.5 Driven qubit 44

2.2.6 Qubit readout techniques 45
2.3 Conclusions 50

3 Measurements of fluxon radiation 53
3.1 Experimental setup and technique 54
3.1.1 Sample design and fabrication 54
3.1.2 Sample holder 62
3.1.3 Cryogenic setup 63
3.2 Experimental results 70
3.2.1 Zero-field step measurements 70
3.2.2 Fine structure of zero-field steps 75
3.2.3 Radiation linewidth 84
3.2.4 Phase-locking of a fluxon oscillator 89
3.3 Conclusions 95

4 Fluxon readout for flux qubits 97
4.1 Scattering of a fluxon on a current dipole 100
4.1.1 Perturbation approach 101
4.1.2 Numerical simulation 105
4.1.3 Flux qubit as a current dipole 107
4.2 Experimental results 109
4.2.1 Fluxon and flux qubit: weak coupling 109
4.2.2 Fluxon and flux qubit: strong coupling 120
4.2.3 Back-action 123
4.3 Conclusions 129

Conclusion and Outlook 131

References 135

List of publications 142

Introduction

To understand - means to simplify. Said by many, origin unknown. When taking a complex phenomenon a physicist tends to break it into smaller and simpler parts. Or, from other side, we build a complex and useful object by taking simple and well studied components and binding them together. Funny things start to happen with understanding when a complexity by itself is an object. The latter happens often in nonlinear physics and chaos along with solitary waves are best representatives. The second one from this pair is going to be the main object of study of this thesis in the form of flux solitons or *Josephson vortices*.

Josephson vortices

A Josephson vortex, or *fluxon*, is a magnetic quasi-particle existing in distributed Josephson junctions. It was discovered through an occurrence of specific voltage steps on current-voltage characteristics of long Josephson junctions [FD73]. The fluxon in underdamped Josephson transmission line (JTL) has properties of a relativistic particle carrying a magnetic flux quantum $\Phi_0 = h/2e$. The size of a vortex can vary from few to several hundreds of microns, depending on the critical current density j_c and its velocity u inside the junction. By applying a bias current, the vortex can be accelerated up to the Swihart velocity c_0, which is the speed of light in JTL. The dynamical properties of a fluxon resemble a classical particle with a well-defined mass and velocity. Nevertheless, at sufficiently low temperatures, quantum properties of fluxons such as tunneling and energy level quantization can be observed [WLU03].

Another distinctive property of the Josephson vortex in JTL is that it has properties of a topological soliton [DJ89]. In other words, a fluxon is a self-reinforcing solitary wave. Solitons are caused by a mutual can-

celation of nonlinear and dispersive effects in the medium and possess weird properties. The most notable of them is an ability of solitons to emerge from a collision with each other unchanged, except for a phase shift.

There were a number of various applications exploiting fluxons and their distinctive properties. One of the most significant is the so-called rapid superconducting single flux quantum (RSFQ) electronics. The low-temperature RSFQ logic employs magnetic fluxons in Josephson transmission lines as basic logic bits for classical computation [Lik12, And10]. RSFQ clock frequencies can reach 770 GHz [CRL99] and, thus, RSFQ can easily outperform modern room temperature computers.

Quantum computing

The idea of quantum computers has emerged at the end of 20-th century. Generally, it was rather the idea of building a simulator for quantum systems than solving classical problems with quantum mechanics [Fey82]. However, later, some more practical applications of quantum computing to a classical world were found. The best example to the present time is a so-called Shor's quantum factoring algorithm [Sho97] which allows one to find the prime factors of an n-digit integer N in only polynomial time of the order n. In comparison, all known classical algorithms for this problem require time exponentially rising with $t \sim \exp n$. Thus, the usefulness of quantum computers became obvious for everyone (especially for military and banks, as both rely heavily on public-key cryptography based on impossibility of factoring large numbers). So, the quest for building a full scale quantum computer began.

Most important building block for every quantum computer is a so-called quantum bit or *qubit*. It is called by analogy to classical bits composing the basis of all modern computers. The main difference between these two is that the qubit can be in a quantum superposition of state 0 and state 1. Essentially, for physicists it means that a quantum two-level system is needed in order to realize such the qubit. It took some time to build the first real quantum bit in a real experiment with a charge qubit [NPT99] with the coherence times of several nanoseconds and a bit later with a flux qubit [Moo99]. Two years later, the first

simple realization of Shor's quantum factoring algorithm was demonstrated with the use of nuclear magnetic resonance techniques and spin qubits [VSC01]. After this, all kinds of experiments with qubits poured as from the horn of plenty. Many other types of quantum bits were invented and investigated [MMS01, YN05, CW08, Mar09].

Merging classical and quantum

Nowadays, quantum computing is a well developed field with many distinct branches and directions of research. Qubits are no mystery anymore and the main remaining problem with them is their limited decoherence times which have reached these days 100 μs threshold [RGS12]. As the decoherence times are improving new challenges arise. One of them is the problem of the appropriate interface between the quantum bits and the classical control computer which should process huge amounts of data to readout the qubit entangled states in order to perform quantum computation. There are several possible solutions to this task - one of them is to use a so-called frequency division technique to access every single qubit via slightly detuned microwave resonators and, thus, build a multiplexing readout [JPU12]. Another intriguing approach is to directly link qubits to the existing low-temperature RSFQ electronics via implementing a *fluxon readout*. Experimental investigating of the latter approach will be the grand goal of the current thesis.

Basically, the challenge is to directly link a single RSFQ logic bit - a fluxon - and a flux qubit, preserving the quantum dynamics of the latter and obtaining useful information from the former, all at the same time. Performing such an experiment may open the road to construction of a full-scale quantum computer as it allows to build both the quantum part and the classical control counterpart (in the form of RSFQ digital computer) on the same chip.

Thesis outlook

The thesis is organized as follows. In the first chapter, a general introduction into superconductivity and related problems is given. It is mainly dedicated for an unprepared reader and can be easily skipped if necessary.

The first part of the second chapter provides the required theoretical basis of Josephson vortices and long Josephson junctions. The sine-Gordon equation, governing the dynamics of fluxons in JTLs, is derived from first principles. Possible excitations of sine-Gordon equation are discussed as well as their interactions with fluxons. In the second part of the second chapter, the basics of flux qubits are given. Classical and quantum mechanical descriptions are provided.

The third chapter presents experimental results on creation and detection of single fluxons in annular Josephson junctions via various methods. A fine structure of resonant zero-field steps are discussed. The measurements of fluxon radiation linewidths are presented. Results on a phase-locking of a single fluxon in the annular Josephson junction are shown.

Finally, the fourth and last chapter presents results on an actual fluxon readout of a flux qubit. First of all, the required theory of fluxon interaction with a current dipole is developed and analyzed. Using this theory, the discussed fluxon readout can be performed. A direct spectroscopy of quantum energy levels of a flux qubit via the fluxon readout is implemented.

1 From zero-resistivity to Josephson vortices

The main purpose of the present chapter is to provide a consistent and simple introduction to the Josephson physics for an unprepared reader (though the reader has to remember some basic facts from electrodynamics and quantum mechanics). It will start from the general phenomenon of superconductivity, proceed with basic theories and facts, and end up with Josephson nonlinear physics.

1.1 Quantum mechanics and superconductivity phenomenon

One could say that the last century in physics passed under the sign of quantum mechanics. Since the development of the axioms of quantum mechanics by Nils Bohr, Erwin Schrödinger, and Werner Heisenberg, huge progress was made on the way of understanding and manipulating the world of micro- and nano-sizes where the laws of quantum mechanics dominate over classical physics. Superconductivity, without any doubts, belongs to one of the areas which benefited most from the development of quantum mechanics and, virtually, may be a synonym of the word "quantum".

1.1.1 Zero resistivity and Meissner effect

Zero resistivity and thus perfect conductivity is the property which gave the name to the phenomenon of superconductivity. Superconductivity has been known already for more than 100 years. It was discovered in 1911 by H. Kamerlingh-Onnes who studied the temperature dependence of the resistance of a mercury sample and found its very surprising behavior: at a temperature of $T_c = 4$ K, the resistance abruptly dropped to zero and remained unmeasurably small at temperatures below T_c. This temperature dependence of the resistance is schematically illustrated in

Fig. 1.1. It is important to notice that the resistance at temperatures below T_c is not just very small, but is exactly zero! Thus, any small electrical current which may occur in the superconducting sample will not decay and persists as long as the sample temperature is kept below T_c.

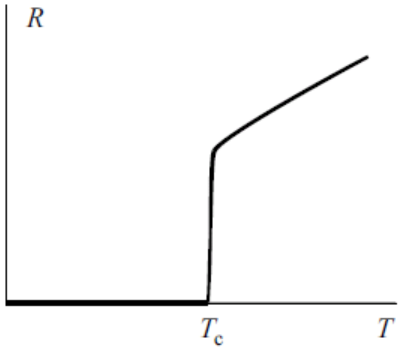

Figure 1.1: Temperature dependence of resistance R for a typical superconductor.

For some time, people have believed that a superconductor is simply a perfect conductor with zero losses. In fact, the reality happened to be a bit more complicated as it was found that superconductors also have the wonderful property of expeling magnetic field. Thus, a superconductor appears to be an ideal diamagnet. This property was experimentally discovered in 1933 by W. Meissner and R. Ochsenfeld and since then is called the *Meissner effect*. What is important for the description of the Meissner effect is that for the final state of a superconductor it does not matter whether the magnetic field was switched on for $T > T_c$ or for $T < T_c$ (see Fig. 1.2).

1.1.2 Theory of superconductivity

The first approach to describe the electrodynamics of superconductors was the phenomenological theory of the London brothers (1935). Basically, it was just a modification of the Maxwell equations in order to take into account the absolute diamagnetism and the absence of dc-resistivity

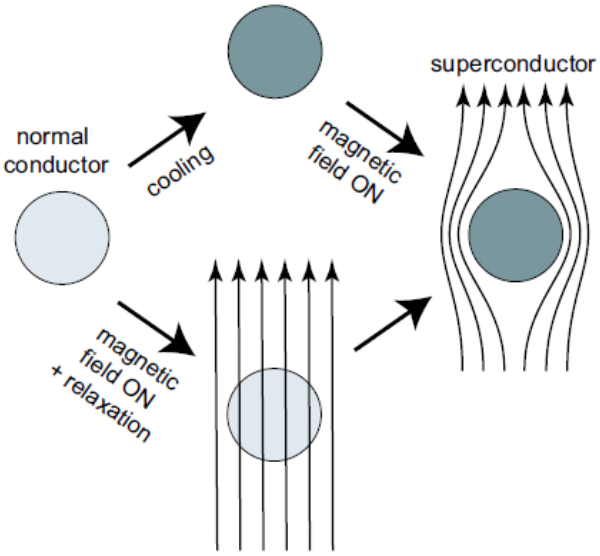

Figure 1.2: Meissner effect in a superconductor. An external magnetic field is always expelled from the interior of the superconductor as it is cooled through T_c. Taken from [UstNP].

in superconductors. According to the London theory, electrons were considered as a mixture of two components: a superconducting one and a normal one. Real superconductor in this theory is modeled by a parallel connection of a normal resistor and an ideal conductor. The ideal conductor in this scheme should also have some finite inductance in order to describe inertial properties of the superconducting electrons. The London equations gave a basic description of the behavior of superconductors in permanent and variable electromagnetic fields. However, in the late 1940-s, it became obvious that London theory gives a wrong answer at least on one question. From this theory followed that the surface energy between superconducting and normal phases should be negative $\sigma_{ns} < 0$. This means, that in the presence of external magnetic field it is energetically favorable for a superconductor to split into a configuration of alternating normal and superconducting phases with the largest surface area possible. This clearly contradicted certain experimental results which showed $\sigma_{ns} > 0$ for superconductor materials

as lead or aluminum.

This contradiction was lifted by the Ginzburg-Landau theory (1950), which essentially was also a phenomenological one, but also took into account quantum effects. The need to consider quantum effects stemmed from the fact that on a boundary between normal and superconducting phases there should always be a finite gradient of a wavefunction of superconducting electrons (more details on this statement and the following derivations can be found in [Sch97]). As it is well known from quantum mechanics, the gradient of a wavefunction $|\nabla\Psi|^2$ is proportional to the density of kinetic energy. This means that by taking into account quantum effects, we consider an additional positive energy stored in the NS-boundary. Thus, quantum effects can allow us to obtain a positive surface energy $\sigma_s > 0$.

The behavior of superconducting electrons in the framework of Ginzburg-Landau (GL) theory is described by some efficient wavefunction $\Psi(\vec{r})$, the origin of which was not known at that time. It was postulated that the superconducting state was a more ordered state than the normal one and that the transition between them is a phase transition of second order (when the state of the system changes continuously but its symmetry undergoes an abrupt change). So, the low-temperature phase is a less symmetric state with a larger degree of order. Another major step made by Ginzburg and Landau was to choose the wavefunction of superconducting electrons $\Psi(\mathbf{r})$ as the order parameter itself. Moreover, lets set the normalization of this wavefunction equal to the density of superconducting electrons

$$|\Psi(\vec{r})|^2 = \frac{n_s}{2}. \tag{1.1}$$

Around T_c and in the presence of magnetic field, the expansion of Gibbs free energy in powers of Ψ takes the following form:

$$G_{sH} = G_n + \alpha|\Psi|^2 + \beta|\Psi|^4 + \frac{1}{2m^*}|-i\hbar\vec{\nabla}\Psi - \frac{2e}{c}\vec{A}\Psi|^2 + \frac{H^2}{8\pi} - \frac{\vec{H}\vec{H}_0}{4\pi}, \tag{1.2}$$

where G_n is the superconductor density of free energy in the normal state and $\vec{H}_0$ is a homogeneous external magnetic field. To obtain the first equation of the GL theory we integrate Eq.(1.2) over the full superconductor volume V and then solve a variational problem with respect

to Ψ for the free energy. At the end, we obtain the sought-for equation and the boundary condition for it:

$$\alpha\Psi + \beta\Psi|\Psi|^2 + \frac{1}{4m}(i\hbar\vec{\nabla} + \frac{2e}{c}\vec{A})^2\Psi = 0, \tag{1.3}$$

$$(i\hbar\vec{\nabla}\Psi + \frac{2e}{c}\vec{A}\Psi)\vec{n}\Big|_S = 0, \tag{1.4}$$

where **n** is the unitary vector, perpendicular to the surface of superconductor S. Solving the same variational problem on the vector potential $\vec{A}$ we get the second equation of GL theory:

$$\vec{j_s} = -\frac{i\hbar e}{2m}(\Psi^*\vec{\nabla}\Psi - \Psi\vec{\nabla}\Psi^*) - \frac{2e^2}{mc}|\Psi|^2\vec{A} \tag{1.5}$$

These two equations compose the skeleton of the GL theory. Despite their phenomenological nature they are extremely efficient for the analytic description of superconductors and rather simple to employ. Applying GL theory to superconductor alloys it is possible to predict the existence of two types of superconductors: those with positive and those with negative surface energies σ_{ns}, which correspond to the first and the second type superconductors, respectively.

However, neither the London theory nor the Ginzburg-Landau theory gave an answer to the question what those mysterious superconducting electrons are and what the microscopic reason for their existence is. The decisive step was proposed by L. Cooper - the idea was that if two electrons in a normal metal, with opposite spins and in the close vicinity of the Fermi surface, by any reason, are being attracted to each other, then they assemble a bound state no matter how weak this attraction is. It was followed by the renowned theoretical paper [BCS57] by J. Bardeen, L. Cooper, and J. Schrieffer, which has developed the foundations of microscopic theory of superconductivity - the so-called Bardeen-Cooper-Schrieffer (BCS) theory.

In BCS theory it was shown that the electron-phonon interaction in solids can lead, under certain conditions, to attraction between electrons. Let us pretend the following situation: a free electron in a metal propagates through a crystal lattice with the certain wavevector $\vec{k}_1$. Then, at some moment of time, it emits a phonon with a wavevector

$\vec{q}$ which is, shortly after, absorbed by another electron with the initial wavevector $\vec{k}_2$. Such a scattering process can be described by the diagram (see Fig. 1.3) or by the law of momentum conservation:

$$\vec{k}_1 + \vec{k}_2 = \vec{k}_1' + \vec{k}_1' \tag{1.6}$$

When an electron moves from the state $\vec{k}_1$ into the state $\vec{k}_1'$, oscillations

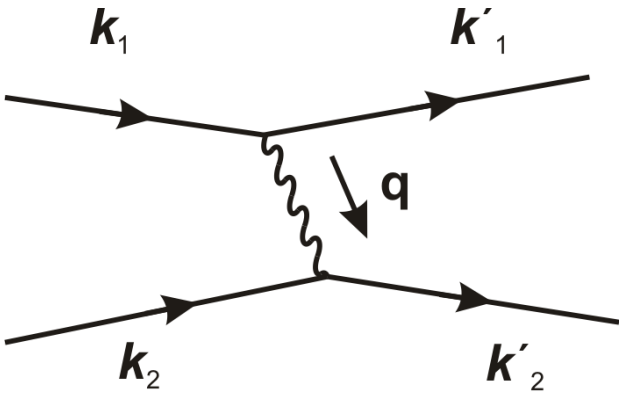

Figure 1.3: The diagram illustrating the scattering process of two electrons by means of a phonon emission and a consecutive absorbtion.

of electron density with the frequency $\omega = (\epsilon_{\vec{k}_1} - \epsilon_{\vec{k}_1'})/\hbar$ arise, where ϵ_1 and ϵ_1' are energies in the states $\vec{k}_1$ and $\vec{k}_1'$ respectively. If, as the result of these oscillations, at this place a local increase of electron density occurs, then ions of the crystal lattice are attracted to this place to compensate the excessive negative charge. This motion continues even when the excessive negative charge will disappear due to a large ion inertia and, thus, an overcompensation can happen. So, in this place an excessive positive charge can arise and the second electron with the wavevector $\vec{k}_2$ is effectively attracted to the first electron. This is one of the possible scenarios of attractive interaction between electrons in the solids, which can only happen when lattice oscillations occur in phase with a "driving" force (which is determined by the electron density oscillations). The latter is only possible when the oscillation frequency of the driving force is less than the eigenfrequency of the crystal lattice $\omega < \omega_D$, where ω_D is Debye frequency. For an electron to move from the state $\vec{k}_1$ to the

state $\vec{k}_1'$, it is required that the latter state is non-occupied - because of the Pauli principle. This means, that the described interaction is realizable in the vicinity of a Fermi surface only. Summarizing all said above in the form of a matrix element of electron interaction $V_{\vec{k}\vec{k}'}$ we can write a basic law of the BCS theory:

$$V_{\vec{k}\vec{k}'} = \begin{cases} -V, (|\epsilon_{\vec{k}} - \epsilon_F| \leq \hbar\omega_D) \parallel (|\epsilon_{\vec{k}'} - \epsilon_F| \leq \hbar\omega_D), \\ 0, (|\epsilon_{\vec{k}} - \epsilon_F| > \hbar\omega_D) \parallel (|\epsilon_{\vec{k}'} - \epsilon_F| > \hbar\omega_D). \end{cases} \tag{1.7}$$

Then, the full energy of the superconductor in the state described by some arbitrary $v_{\vec{k}}$ distribution is:

$$E_s = \sum_{\vec{k}} 2\epsilon_{\vec{k}} v_{\vec{k}}^2 + \sum_{\vec{k},\vec{k}'} V_{\vec{k}\vec{k}'} v_{\vec{k}'} u_{\vec{k}} v_{\vec{k}} u_{\vec{k}'}, \tag{1.8}$$

where the first part gives the full kinetic energy ($\epsilon_{\vec{k}} = \hbar^2\vec{k}^2/2m - \hbar^2\vec{k}_F^2/2m$ - is the electron energy counted from Fermi level), $v_{\vec{k}}$ is a probability that the couple of states $(\vec{k}, -\vec{k})$ are occupied, $u_{\vec{k}}^2 = 1 - v_{\vec{k}}^2$. Minimizing the energy E_s with respect to $v_{\vec{k}}$ we obtain:

$$v_{\vec{k}}^2 = \frac{1}{2}(1 - \frac{\epsilon_{\vec{k}}}{\epsilon_{\vec{k}}^2 + \Delta_0^2}), \tag{1.9}$$

where

$$\Delta_0 = V \sum_{\vec{k}'}{}' v_{\vec{k}} u_{\vec{k}}. \tag{1.10}$$

The summation in Eq.(1.10) is carried only over the states $\vec{k}$ which lay in the spherical layer nearby the Fermi surface, where the matrix element $V_{\vec{k}\vec{k}'}$ is nonzero. Putting Eq.(1.9) into Eq.(1.10) and substituting the summation over $\vec{k}$ by integration over the respective energy scale, we obtain at the end:

$$\Delta_0 \simeq 2\hbar\omega_D \exp(-\frac{1}{N(0)V}), \tag{1.11}$$

where $N(0)$ is the density of states near the Fermi level. The full energy difference of a normal metal state and a superconducting state at zero temperature $T = 0$ can be defined as:

$$W = E_s - E_n. \tag{1.12}$$

Substituting Eq.(1.8) into Eq.(1.12) (the energy of the normal metal state is simply defined by the kinetic energy of the Fermi sphere $E_n = \sum_{\vec{k}\leq\vec{k}_F} 2\epsilon_{\vec{k}}$ and taking into account Eq.(1.11), results in:

$$W = -\frac{1}{2}N(0)\Delta_0^2. \tag{1.13}$$

Thus, the difference between the energies of the superconducting and the normal states is negative which means that the superconducting state is preferred at $T = 0$. Using the same approach, one obtains the

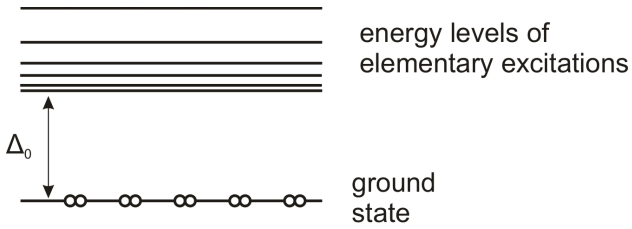

Figure 1.4: The energy gap Δ_0 separates the area of elementary energy excitations from the ground state of superconductor.

energy $w_{\vec{q}}$ required to add a single unpaired electron with momentum $\vec{q}$ to a superconductor. This energy turns out to be:

$$w_{\vec{q}} = \sqrt{\epsilon_{\vec{q}}^2 + \Delta_0^2}. \tag{1.14}$$

This is a very important formula for explaining superconductivity as it tells us that when one electron is added to the superconductor in the ground state, we increase the total energy at least by the amount of Δ_0. It means that the spectrum of elementary excitations is separated from the superconductor ground state by the value Δ_0, also called the "superconductor energy gap" (see Fig. 1.4). This property is very important for understanding of physics of superconductors and explains the existence of the mysterious superconducting electrons. The latter are simply the electron Cooper pairs condensed into the ground state. As an energy larger than twice the gap $E > 2\Delta_0$ is needed to tear apart a single Cooper pair, it means that all inelastic scattering processes with an energy difference smaller than $2\Delta_0$ are impossible in the superconducting state and therefore do not give rise to a finite resistance.

1.1.3 Flux quantization

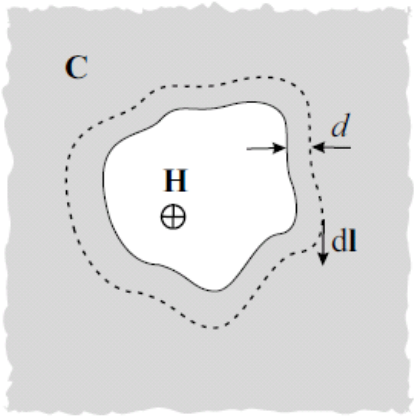

Figure 1.5: A superconductor with a hole and magnetic field H. Taken from [UstNP].

The quantization of magnetic flux is an important phenomenon in physics of superconductors. It can be derived from the following assumptions: the charge carriers in superconductors are Cooper pairs which are formed by two separate electrons, thus the elementary charge is equal to $2e$. The second idea is that all electron pairs form a condensate which is described by a wave-function Ψ and share a common energy level:

$$\Psi = \sqrt{\frac{n_s}{2}} \exp(i\theta(r)). \tag{1.15}$$

The continuity equation in quantum mechanics gives us the expression for an effective particle flow:

$$\frac{n_s}{2}\vec{v_s} = \frac{i\hbar}{2m}(\Psi\vec{\nabla}\Psi^* - \Psi^*\vec{\nabla}\Psi). \tag{1.16}$$

The canonical momentum of a Cooper pair in the magnetic field $\vec{H} = \vec{\nabla} \times \vec{A}$ is given by:

$$\vec{p} \equiv \hbar\vec{\nabla}\theta = 2m\vec{v_s} + 2e\vec{A} \tag{1.17}$$

Taking the equations Eqs. (1.15),(1.16) and substituting them into Eq. (1.17) results in the quantum-mechanical generalization of the second London

equation in the gauge invariant form:

$$\vec{J_s} = n_s e \vec{v_s} = \frac{1}{\Delta_0}(\frac{\Phi_0}{2\pi}\vec{\nabla}\theta - \vec{A}) \tag{1.18}$$

where

$$\Phi_0 = \frac{\pi\hbar}{e} = 2.0678 \times 10^{-15} Wb \tag{1.19}$$

is the *magnetic flux quantum*. Let us consider a situation with a superconductor with a hole as shown in Fig. 1.5. First, a magnetic field $\vec{H}$ is applied perpendicular to the plane of superconductor at a temperature $T > T_c$. Then, the superconducting state is achieved by lowering the temperature $T < T_c$ in the presence of constant external magnetic field $\vec{H}$. One can estimate a total flux Φ inside the hole by integrating (1.18) along the contour **C**, which yields:

$$\frac{\Phi_0}{2\pi}\oint_C \vec{\nabla}\theta d\vec{l} = \oint_C \vec{A}d\vec{l} = \Phi. \tag{1.20}$$

The wave function (1.15) must have a single value at any point of the superconductor. This requires that $\exp(i\theta) = \exp(i\theta + 2\pi k)$, where $k = 0,\ \pm 1,\ \pm 2,\ ...$ is an integer. Finally, it gives us:

$$\Phi = k\Phi_0, \tag{1.21}$$

i.e. the magnetic flux in the hole is quantized.

1.2 Josephson effect

The Josephson effect was predicted by Bryan David Josephson in 1962 in his classic paper [Jos62]. He stated a hypothesis that a tunnel junction between two superconductors should allow a small non-dissipative current flow through it because of the tunneling of Cooper pairs. He also predicted that an application of a constant voltage V to such a junction will cause the current to oscillate with a frequency $\nu = 2eV/h$. Back at that time, it was a pretty arguable result which has created turbulent discussions. It seemed, that if an amplitude of tunneling probability for a single electron is equal to $\exp(-a) \ll 1$, so that the tunneling probability is $\exp(-2a)$, then the tunneling amplitude for two

electrons would be $\exp(-2a)$ and, consequently, the tunneling probability of Cooper pairs would be negligible with respect to single electron tunneling $\exp(-4a) \ll \exp(-2a)$. However, such reasoning does not take into account the coherence of Cooper pairs tunneling, because of which the tunneling current of a pair becomes proportional to $\exp(-2a)$. The first experimental evidence for the Josephson effect was found by Anderson and Rowell [AR63].

1.2.1 Semi-phenomenological approach

There are many ways of deriving Josephson equations. It is very useful and simple to use the semi-phenomenological approach proposed by Feynman [FLS65]. Lets consider the tunneling system: superconductor - tunnel barrier - superconductor, as illustrated in Fig. 1.6. If the current

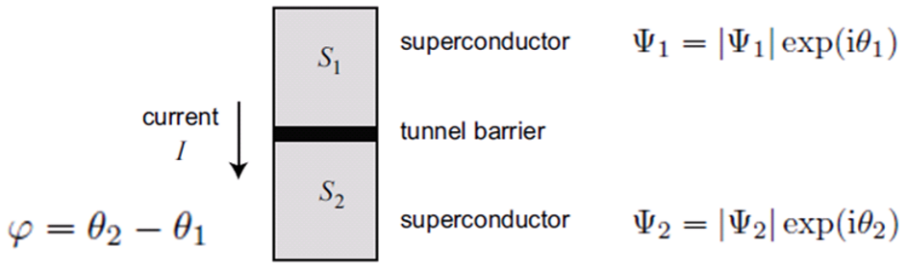

Figure 1.6: General model of a Josephson junction as a tunnel barrier between two bulk superconductors S_1 and S_2.

flowing through the tunnel barrier is large enough, $I > I_c$, a finite voltage V appears across the junction. The energetic spectrum of the Josephson junction with applied voltage V is shown in Fig. 1.7. If our system can exist only in discrete energy states, then the system wave function can be expanded into the full basis:

$$\Psi(t) = \sum_i c_i(t)\psi_i. \tag{1.22}$$

A transition of a Cooper pair from the ground level of S_1 to the ground level of S_2 is defined by the matrix element of a system Hamiltonian:

$$H_{ij} = \int \Psi_i^* \hat{H} \Psi_j dV, H_{12} = H_{21} = K. \tag{1.23}$$

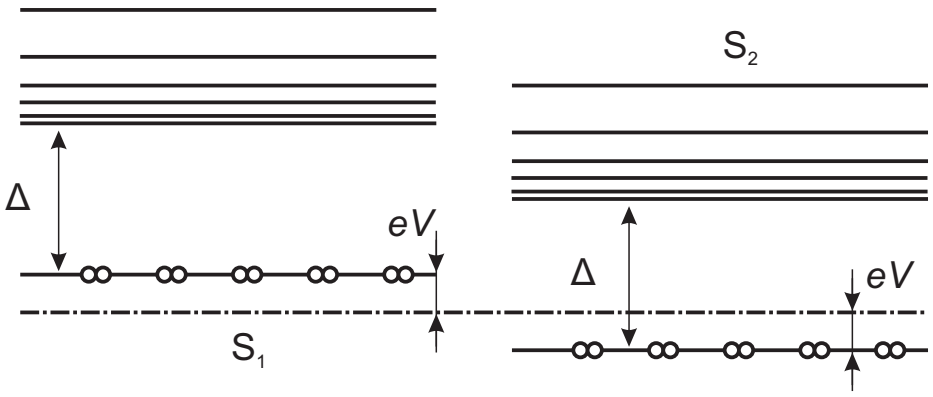

Figure 1.7: The energy spectrum of a tunnel Josephson junction with an applied voltage V. The ground states of S_1 and S_2 are separated by the voltage $2eV$.

Substituting (1.22) into the time-dependent Schrödinger equation and taking into account (1.23), we get:

$$i\hbar\frac{dc_1}{dt} = eVc_1(t) + Kc_2(t), i\hbar\frac{dc_2}{dt} = Kc_1(t) - eVc_2(t). \tag{1.24}$$

Now, we recall that we are dealing with superconductors and c_1 and c_2 are the state amplitudes of Cooper pairs on the ground levels of S_1 and S_2, respectively. This means that $|c_1|^2$ and $|c_2|^2$ are normalized in a way to give the mean density of superconducting electrons $|c_1|^2 = |c_2|^2 = n_S$. Here, for simplicity, we assume that S_1 and S_2 superconductors are made from the same material. Introducing amplitudes c_1 and c_2 as follows:

$$c_1 = \sqrt{n_S}\mathrm{e}^{i\theta_1}, c_2 = \sqrt{n_S}\mathrm{e}^{i\theta_2}, \tag{1.25}$$

substituting them into (1.24) and separating real and imaginary parts, we obtain the following equations:

$$\frac{dn_S}{dt} = \frac{2Kn_S}{\hbar}\sin\ \varphi, \tag{1.26}$$

$$\frac{d\theta_1}{dt} = -\frac{K}{\hbar}\cos\ \varphi - \frac{eV}{\hbar}, \tag{1.27}$$

$$\frac{d\theta_2}{dt} = -\frac{K}{\hbar}\cos\ \varphi + \frac{eV}{\hbar}, \tag{1.28}$$

where $\varphi = \theta_2 - \theta_1$. The current through the junction is proportional to the time derivative of the superconducting electron density $I \sim dn_S/dt$ (see [Tin75] for details). Then, from Eq. (1.26), we immediately obtain the first Josephson equation:

$$I = I_c \ \sin \ \varphi. \tag{1.29}$$

Subtracting Eq. (1.27) from Eq. (1.28), we obtain the second Josephson equation:

$$V(t) = \frac{h}{2e}\frac{d\varphi}{dt}. \tag{1.30}$$

.

1.2.2 Microscopic approach

The derivation of the Josephson relations made above is sufficient for the phenomenological explanation of weak superconductivity. However, for the microscopic deciphering of constants such as the Josephson critical current I_c, the microscopic approach of the Bardeen-Cooper-Schrieffer (BCS) theory is required. It is based on the tunneling Hamiltonian H_T written in terms of creation and annihilation operators:

$$H = H_L + H_R + H_T, \tag{1.31}$$

where H_L and H_R are the Hamiltonians of left and right superconducting electrodes, $H_T = \sum\limits_{\vec{k}\vec{q}p} [T_{\vec{k}q} c^+_{\vec{k}p} d_{\vec{q}p} + T^*_{\vec{k}q} d^+_{\vec{q}p} c_{\vec{k}p}]$ corresponds to the tunneling interaction and is responsible for the transfer of electrons between superconducting electrodes ($c^+_{\vec{k}p}(c_{\vec{k}p})$ is the operator of creation (annihilation) of an electron with momentum $\vec{k}$ and spin p in the left electrode, $d^+_{\vec{q}p}(d_{\vec{q}p})$ is the operator of creation (annihilation) of an electron with momentum $\vec{q}$ and spin p in the right electrode, $T_{\vec{k}q}$ is the matrix element defining the probability of electron transfer from the left state $\vec{k}$ into the right state $\vec{q}$). The derivation of the Josephson relations is reduced to the calculation of this tunneling matrix $T_{\vec{k}p}$. This is a rather long and complex procedure, not suited well for the theory introduction of this experimental thesis, so I will proceed right away to the main results of such a derivation.

One of the most important results from the BCS calculation of the Josephson current is the estimate of the Josephson critical current based on microscopic parameters versus temperature for the case of two similar superconductors forming the Josephson junction. This calculation has been done for the first time by V. Ambegoakar and A. Baratoff [AB63] and concludes as:

$$I_c(T) = \frac{\pi\Delta(T)}{2eR_n}\text{th}\left(\frac{\Delta(T)}{2k_BT}\right), \tag{1.32}$$

where R_n is the normal state resistance of the Josephson junction. It is important for us to remember this formula as it fuses together two of the most important quantities for superconductors as a function of electron temperature T: the critical current I_c and the energy gap Δ.

Another interesting result arises during the direct calculation of a Josephson current through the BCS theory. The resulting formula for the current through the junction, derived from the Hamiltonian (1.31), for a finite applied voltage, reads [Jos62]:

$$I(t,V,T) = I_c(V,T)\ \sin\varphi(t) + V\sigma_0(V,T)\left[1+\epsilon(V,T)\ \cos\varphi(t)\right], \tag{1.33}$$

where the first part of the equation describes the supercurrent, while the second - a quasiparticle current in the finite voltage regime which, surprisingly, contains the cos φ contribution. It is interesting to mention that the parameter ϵ, which determines the sign of this additional contribution, is roughly $\epsilon \simeq -1$ (basically this contribution is absent and non-observable) as found from various experiments [PFL72, FPT73] while it should vary from -1 to 1 based on different theoretical predictions. This mysterious problem of the cos φ term has stayed unsolved despite many publications on-topic.

1.3 Conclusions

This chapter presented a simplified introduction into the physics of conventional superconductors and Josephson junctions. The concepts of flux quantization, superconducting energy gap, and Josephson equations were developed. For a more detailed exposition of the general physics of superconductivity and Josephson effects, the reader is advised to address one of the following textbooks [Sch97, Tin75, Lik86].

2 On fluxons and flux qubits

In this chapter, a basic description on Josephson vortices or *fluxons* and flux qubits as well as the idea of fluxon based readout of superconducting qubits is given.

2.1 Fluxons

Quantization of magnetic flux is the well-known phenomenon for superconductors (see Section 1.1.3). Magnetic flux quanta Φ_0 can exist in an isolated form of magnetic particles in long Josephson junctions. They are known as Josephson vortices or *fluxons*. Physically, each fluxon is formed by a screening current, circulating between two electrodes of a long Josephson junction (illustrated below in Fig. 2.3). Since the discovery of Josephson vortices in 1972 [FD73], a lot of efforts were put into the investigations of fluxon physics and related topics. Detailed research of current-voltage characteristics (so-called zero field steps), caused by the fluxon motion, and their fine structure has received a lot of attention [MBM93, BMU96, MMF98, WUV00, PAU08]. Advanced experiments have also showed the quantum limited behavior of single Josephson vortices [WLU03].

A theoretical description of fluxons can be given via considering a long Josephson junction as a medium for propagation of electromagnetic waves and applying Josephson relations to it, thus obtaining a model in terms of the Josephson phase. To do so, it is useful first to describe the dynamics of the Josephson phase in a point-like Josephson junction.

2.1.1 RSCJ model

To understand and describe physical processes in a single lumped Josephson junction it is helpful to use the equivalent schematic approach de-

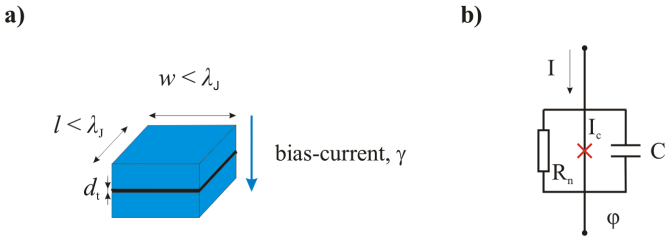

Figure 2.1: a) Sketch of a lumped Josephson junction. **b)** Equivalent circuit representation of a lumped Josephson junction.

picted in Fig. 2.1. The electrodynamics of a small Josephson junction can be accurately described neglecting a variation of the phase difference across the junction area. This approximation is valid given the lateral junction dimensions are less than the characteristic length scale of magnetic field screening inside the Josephson junction - the so-called Josephson penetration depth λ_J - and given that external magnetic fields are small enough. In this limit, a small junction is accurately described by the lumped circuit model shown in Fig. 2.1. The junction is modeled by a parallel connection of an ideal Josephson junction with a certain critical current I_c, a resistor R_n and a capacitor C. Writing down the Kirchoff laws for the equivalent circuit, the total current through the junction can be represented as:

$$I = I_c \sin \varphi + \frac{V}{R_n} + C\frac{dV}{dt}. \tag{2.1}$$

Equation (2.1) can be rewritten in terms of the superconducting phase difference φ using the Josephson equations (1.30) and (1.29):

$$I = I_c \sin \varphi + \frac{\Phi_0}{2\pi R_n}\frac{d\varphi}{dt} + \frac{\Phi_0 C}{2\pi}\frac{d^2\varphi}{dt^2}. \tag{2.2}$$

This model is called the resistively, capacitively shunted junction (RCSJ). It maps the described Josephson junction to another system which is a driven and damped pendulum. In other words, it corresponds to a motion of a point-like particle in a tilted sinusoidal potential, which is also sometimes called a *wash-board potential*. The rich and non-linear

dynamics of such a system can be investigated by means of Josephson junctions.

The Josephson energy stored inside a junction can be derived using $U = \int IV dt$ and the Josephson relations (1.29), (1.30), yielding:

$$U(\varphi) = E_J \left(1 - \cos\varphi\right), \tag{2.3}$$

where $E_J = \hbar I_c/2e$. The constant of integration is chosen in such a way that $U(\varphi)$ has a minimum of 0 in the case of vanishing phase difference, which is the case in a bulk superconductor.

In a situation when an alternating current is applied, the Josephson junction can be considered as a non-linear inductor. One can estimate the Josephson self inductance $L_J(\varphi)$ by recalling, again, the Josephson relations (1.29), (1.30) and applying the response relation of a linear inductor $V = -LdI/dt$:

$$L_J(\varphi) = \frac{\Phi_0}{2\pi I_c \cos\varphi}. \tag{2.4}$$

2.1.2 sine-Gordon equation

The wave equation governing electrodynamics of a long Josephson junction (LJJ) can be derived from the RCSJ model discussed above. For this we separate the LJJ in many elementary cells as depicted in Fig. 2.2 and write a system of Kirchoff equations while taking the flux quantization (1.19) into account:

$$\varphi_{k+1} - \varphi_k = \Phi_k = \frac{2\pi}{\Phi_0}(\Phi_{ext} - I_{Lk}L), \tag{2.5}$$

where $\Phi_{ext} = \mu_0 H \Lambda \Delta x$ is the flux threading the k-th loop cell (Λ is a magnetic penetration length deep into the superconducting electrodes). In the limit $\Delta x \to 0$ we can write:

$$\frac{\varphi_{k+1} - \varphi_k}{\Delta x} = \frac{\partial\varphi}{\partial x} = \frac{2\pi}{\Phi_0}(\mu_0 \Lambda H - L_d I_L), \tag{2.6}$$

where $L_d = L/\Delta x$. Differentiating Eq. (2.6) with respect to the space variable we find:

$$\frac{\partial^2\varphi}{\partial x^2} = \frac{2\pi}{\Phi_0}(\mu_0 \Lambda \frac{\partial H}{\partial x} - L\frac{\partial I_L}{\partial x}). \tag{2.7}$$

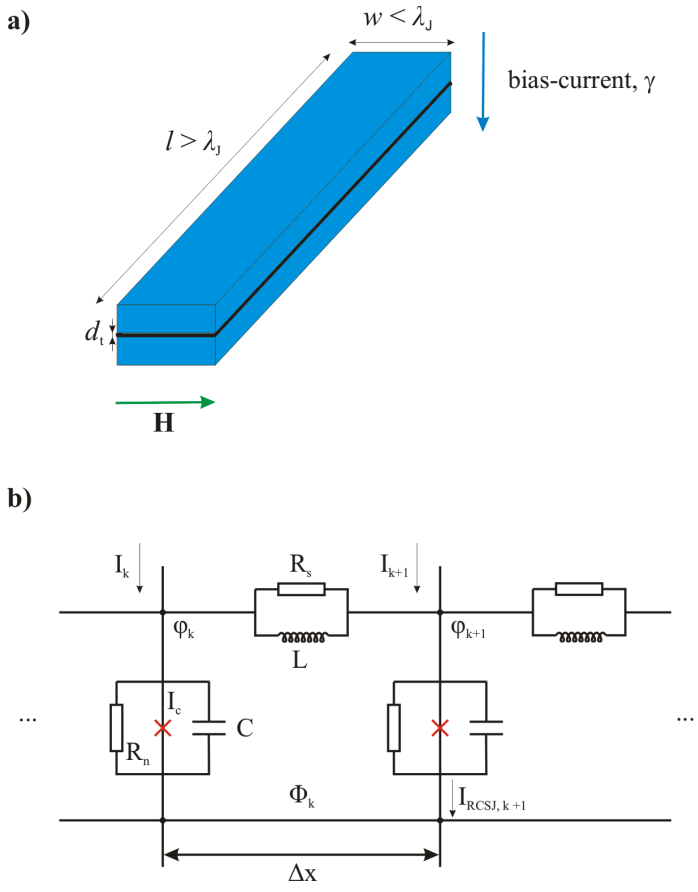

Figure 2.2: a) Sketch of a long Josephson junction. **b)** The lumped elements model of a long Josephson junction. The superconducting phase difference at the node k is given by φ_k. Φ_k is the total flux enclosed in the k-cell.

From the Kirchoff law at the node $k+1$ we get:

$$\frac{\partial I_L}{\partial x} = j - j_{RCSJ} - \frac{\partial I_{R_s}}{\partial x}, \tag{2.8}$$

where $j = I/\Delta x$ and $j_{RCSJ} = I_{RCSJ}/\Delta x$. Substituting in Eq. (2.8), $I_{R_s} = -1/\rho_s \partial V/\partial x$, the RCSJ current density from Eq. (2.2) and considering a homogeneous external magnetic field $\partial \vec{H}/\partial x = 0$, we derive the following equation:

$$\frac{\Phi_0}{2\pi L_d}\frac{\partial^2 \varphi}{\partial x^2} = -j + j_c \sin\varphi + \frac{V}{\rho_n} + C_d\frac{\partial V}{\partial t} - \frac{1}{\rho_s}\frac{\partial^2 V}{\partial x^2}, \tag{2.9}$$

where $C_d = C/\Delta x$, $\rho_n = R_n \Delta x$ and $\rho_s = R_s \Delta x$. Expressing voltages in terms of phase using the second Josephson relation results in the one-dimensional non-linear wave equation for the superconducting phase difference $\varphi(x,t)$, the so-called *perturbed sine-Gordon equation* (PSGE):

$$\frac{\Phi_0}{2\pi L_d}\frac{\partial^2\varphi}{\partial x^2} - \frac{\Phi_0 C_d}{2\pi}\frac{\partial^2\varphi}{\partial t^2} - j_c \sin\varphi = -j + \frac{\Phi_0}{2\pi\rho_n}\frac{\partial\varphi}{\partial t} - \frac{\Phi_0}{2\pi\rho_s}\frac{\partial^3\varphi}{\partial x^2 \partial t}, \quad (2.10)$$

where ρ_n is the quasiparticle resistance per unit length, ρ_s is the surface resistance of the superconducting electrodes per unit length, L_d is the specific inductance of the junction, C_d is the specific capacitance, j_c is the critical current density, and j is the bias current density. This equation provides us with the main tool of describing the behavior of long Josephson junctions in various regimes. The electric and magnetic fields between junction electrodes can be expressed in terms of phase difference as:

$$E = \frac{\Phi_0}{2\pi d_t}\frac{\partial\varphi}{\partial t}, \quad (2.11)$$

$$H = \frac{\Phi_0}{2\pi L_d}\frac{\partial\varphi}{\partial x}. \quad (2.12)$$

The characteristic inductance and capacitance of the junction are given by:

$$L_d = \mu_0 d, \quad (2.13)$$

$$C_d = \frac{\epsilon_0 \epsilon_t}{d_t}, \quad (2.14)$$

where d is the magnetic thickness of the junction. In the limit of thick electrodes (thicker than λ_L), it is given by:

$$d = 2\lambda_L + d_t. \quad (2.15)$$

Dividing Eq. (2.10) by the critical current density j_c and introducing the characteristic screening length of magnetic field, which is the Josephson penetration depth λ_J, and the characteristic plasma frequency ω_p:

$$\lambda_J = \sqrt{\frac{\Phi_0}{2\pi L_d j_c}}, \quad (2.16)$$

$$\omega_p = \sqrt{\frac{2\pi j_c}{\Phi_0 C_d}}, \quad (2.17)$$

the PSGE can be rewritten in a clearer format:

$$\lambda_J^2 \frac{\partial^2 \varphi}{\partial x^2} - \frac{1}{\omega_p^2} \frac{\partial^2 \varphi}{\partial t^2} - \sin \varphi = -\frac{j}{j_c} + \frac{1}{\omega_p^2 C_d \rho_n} \frac{\partial \varphi}{\partial t} - \frac{\lambda_J^2 L_d}{\rho_s} \frac{\partial^3 \varphi}{\partial x^2 \partial t}. \quad (2.18)$$

From the form of this wave equation it is easy to see that the phase velocity of linear waves in the considered system is given by:

$$c_0 = \omega_p \lambda_J = c \sqrt{\frac{d_t}{\epsilon_t d}}, \quad (2.19)$$

where c_0 is usually called the *Swihart velocity* [Swi61] and c is the phase velocity of light in vacuum. Typically, in long Josephson junctions, c_S is only a few percent of c.

For theoretical studies and especially for numerical applications it is useful to normalize the PSGE by redefining the time and space as follows:

$$\tilde{t} = \omega_p t, \quad (2.20)$$

$$\tilde{x} = \lambda_J^{-1} x. \quad (2.21)$$

Then, the PSGE equation takes the form:

$$\frac{\partial^2 \varphi}{\partial \tilde{x}^2} - \frac{\partial^2 \varphi}{\partial \tilde{t}^2} - \sin \varphi = -\gamma + \alpha \frac{\partial \varphi}{\partial \tilde{t}} - \beta \frac{\partial^3 \varphi}{\partial \tilde{x}^2 \partial \tilde{t}}. \quad (2.22)$$

The perturbation terms in the right part of Eq. (2.22) are defined as:

$$\gamma = \frac{j}{j_c}, \quad (2.23)$$

$$\alpha = \sqrt{\frac{\Phi_0}{2\pi j_c C_d}}, \quad (2.24)$$

$$\beta = \frac{\omega_p L_d}{\rho_s}, \quad (2.25)$$

where the first term γ in equation (2.22) is the normalized bias current, the second one is the damping due to quasiparticle resistance and the last one is the damping due to surface losses in the superconducting electrodes.

2.1.3 Josephson vortices

Quantization of magnetic flux is a well-known phenomenon in superconductivity. The same applies to long Josephson junctions. Magnetic flux quanta Φ_0 can exist there in a form of specific magnetic particles. These are known as Josephson vortices or *fluxons*. Physically, each fluxon can be treated as a screening current, circulating between two electrodes of a long Josephson junction (see 2.3). Since the discovery of Josephson vortices in 1972 [FD73] a lot of efforts were put into detailed investigations of fluxon's physics and related topics. Particular experiments have also shown the quantum limited behavior of a single Josephson vortex [WLU03].

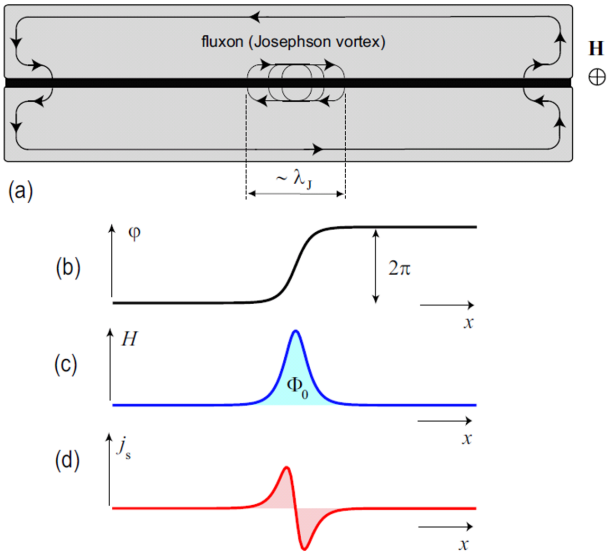

Figure 2.3: Schematic cross section **(a)** of a distributed Josephson junction with a fluxon (Josephson vortex) located deep inside it. Spatial profiles shown below are **(a)** the phase difference φ, **(b)** the normalized magnetic field $H \sim d\varphi/dx$, and **(c)** the supercurrent density $j_s \sim \sin\ \varphi$. Taken from [UstNP].

2.1.4 Excitations in long Josephson junctions

Different types of excitations (including fluxons) in long Josephson junctions can be explained by means of the sine-Gordon equation. For this we can take the normalized PSGE (2.22) and consider the situation of a linear infinitely long Josephson junction with the following boundary conditions (from here on we omit the tilde sign ˜ on top of space and time variables in the normalized sine-Gordon equation and other related formulas):

$$\frac{\partial\varphi}{\partial x}|_{x=\pm\infty} = 0. \tag{2.26}$$

Neglecting all perturbation terms in the PSGE, Eq. (2.22) becomes

$$\frac{\partial^2\varphi}{\partial x^2} - \frac{\partial^2\varphi}{\partial t^2} - \sin\varphi = 0, \tag{2.27}$$

which has an exact solution:

$$\varphi_f(x,t) = 4\arctan\left[\exp\left(\pm\frac{x-ut-x_0}{\sqrt{1-u^2}}\right)\right]. \tag{2.28}$$

This solution describes a *kink* or *antikink* in the phase difference φ (depending on the polarity of the sign in the exponent) moving with a certain velocity $0 \leq |u| < 1$. In Fig. 2.3 we can see the magnetic field profile of such an excitation. Integrating the magnetic field over the profile of a single vortex (antivortex) we obtain that the total amount of magnetic flux carried by the kink equals exactly one flux quantum $\Phi_f = \Phi_0$. Therefore, such a kink is usually called *fluxon* or *Josephson vortex*.

Kinks in the sine-Gordon system have all properties of *solitons*. One of the most amazing properties of solitons is that after the collision of two solitons, they sustain their respective velocities and shapes. Collision usually results only in a slight time delay (or, in a phase shift, in other words). Solitonic solutions usually appear in a media with strong nonlinear effects and finite dissipation. A fluxon in the long Josephson junction is a *topological soliton* as there are no dynamical restrictions of its existence. This is in contrast to dynamical solitons, which have to have a certain energy to exist. The latter usually arises in media where energy pumping stimulates non-linear effects (for instance, such a situation occurs in optical fibers).

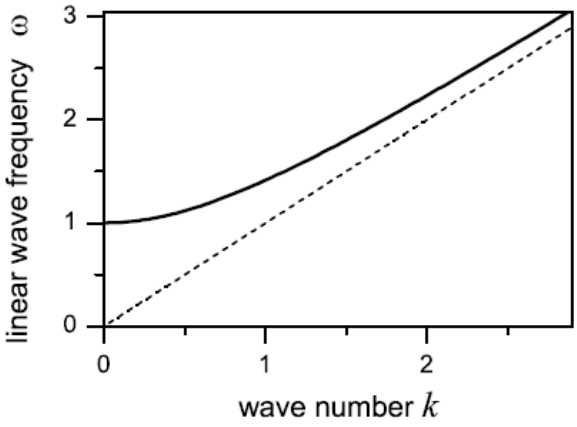

Figure 2.4: The dispersion relation for Josephson plasma waves.

Solutions of the PSGE in the form of topological solitons (2.28) may be the most beautiful ones but the simplest possible solution of Eq. (2.29) is trivial small amplitude oscillations $|\varphi| \ll 1$ in the form of *plasma waves*:

$$\varphi_{pw} = A \exp[i(kx - \omega t)], \tag{2.29}$$

where k is the wave number, ω is the frequency of the linear wave with the dispersion relation (also see Fig. 2.4):

$$\omega = \sqrt{1 + k^2}. \tag{2.30}$$

Another interesting analytic solution of Eq. (2.27) describes the bound kink-antikink (or fluxon-antifluxon) state. This so-called *breather* solution has the form:

$$\varphi_{br} = 4 \arctan \left[\tan\theta \frac{\sin(t\cos\theta)}{\cosh(x\sin\theta)} \right], \tag{2.31}$$

where $0 < \theta < \pi/2$ is the initial phase of the breather. Basically, this solution describes bound oscillations of a fluxon-antifluxon pair around a certain point (see Fig. 2.5). The breather cannot decompose into separate fluxons because its total energy is less than the rest energy of two separated solitons.

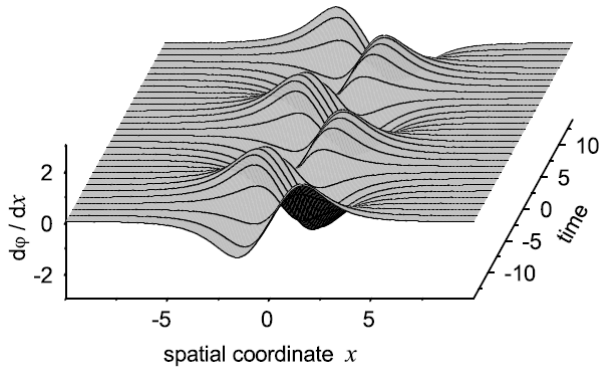

Figure 2.5: Breather solution of the unperturbed sine-Gordon model with $\theta = 1$ and initial velocity $v = 0$. Taken from [UstNP].

Unfortunately, it is difficult to observe Josephson breathers as they tend to decay in the presence of perturbations in the sine-Gordon model (for instance, finite damping for high frequencies, which is, in fact, always present in real systems, kills these oscillations rather quickly). So far, there is no confirmed direct observation of breathers in continuous long Josephson junctions but there are many speculations and theories about them. However, there are confirmations of observance of analogous breathers (so-called *rotobreathers*) in discrete systems, e.g. discrete Josephson junction ladders [BAZ00].

At last, there are many other more sophisticated solutions of the perturbed sine-Gordon system and even more of them for the full PSGE equation. Most of them can be treated as various non-linear superposition of different number of fluxons or antifluxons, plasma waves, breathers, etc. The details of these solutions can be found elsewhere [BP82, Lik86].

2.1.5 Dynamics of fluxons

A Josephson vortex can be driven by external forces, for an example by a bias current applied to the junction. The bias gives rise to a Lorentz force acting on the fluxon, resulting in acceleration of a Josephson vortex along the junction. Due to the presence of quasiparticle dissipation,

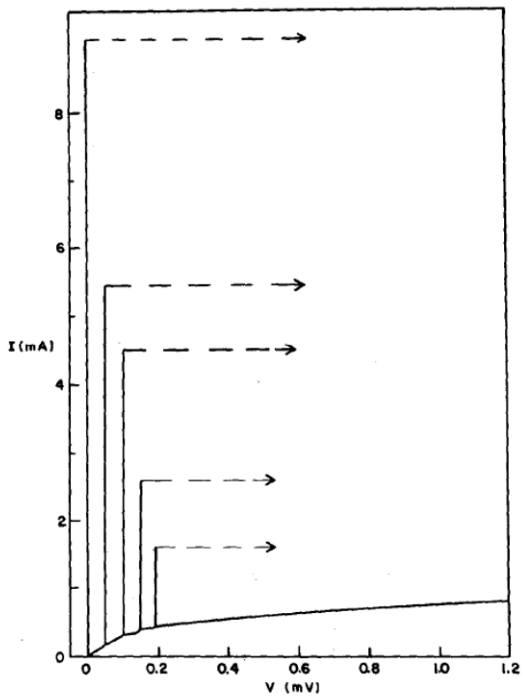

Figure 2.6: The I-V characteristic of a quasi-one-dimensional Pb-PbO_x-Pb junction (0.80 mm $\times$ 0.10 mm) at 4.2 K, measured by Chen, Finnegan and Langenberg in 1971 [CFL72, CL72].

the driving force and the damping are balanced for a certain vortex velocity, leading to a steady motion of a kink and, therefore, due to the AC Josephson relation, to the emergence of a finite voltage drop across the Josephson junction.

This motion usually appears on the IVC of the junction as an almost vertical voltage step (see Fig. 2.6). These steps were discovered in the past as anomalous dc current singularities [CFL72, CL72]. Such singularities appear in Josephson junctions with lateral dimensions much greater than λ_J. Later, the name of "zero field steps" was applied to these peculiarities underlining the absence of any external magnetic field needed to observe them.

More generally, for a single Josephson vortex, an ideal current-voltage

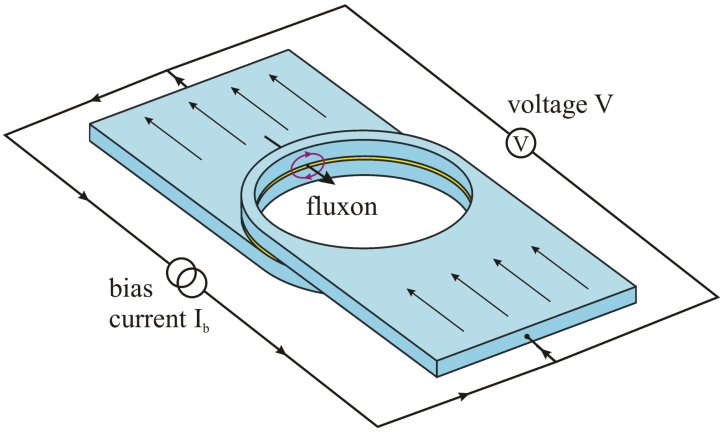

Figure 2.7: A four-pole measurement scheme of an annular Josephson junction in the "Lyngby" geometry. This type of electrodes supposes to organize a homogeneous bias current in the AJJ and, thus, a homogeneous Lorentz force acting on a fluxon.

characteristic looks like as it is shown later in Fig. 2.8. The underlying physical picture here is rather simple: for small bias currents $\gamma = I_b/I_c \ll 1$ the fluxon behaves as a purely classical particle moving under an external force in a medium with viscous losses; for larger biases $\gamma \sim 1$, the fluxon velocity approaches the phase speed of light in the long Josephson junction and therefore the fluxon starts to undergo Lorentz contraction as well as other relativistic effects. It is possible to calculate the precise form of the I-V curve for the single fluxon taking into account losses in the form of viscous damping with a coefficient α and energy insertion in the form of a homogeneous bias current γ. For every bias current value γ a certain equilibrium fluxon's velocity v_{fluxon} exists for which the energy input by bias current is exactly compensated by losses. This calculus has been done by McLaughlin and Scott [MS78]. The resulting formula of the equilibrium fluxon velocity has the following form:

$$u = \frac{1}{\sqrt{1 + (4\alpha/\pi\gamma)^2}}. \tag{2.32}$$

2.1.6 Detecting a fluxon

For experiments with fluxons it is convenient to use so-called annular Josephson junctions (AJJs) rather than the linear ones. A sketch of such an AJJ is shown in Fig. 2.7. A convenience of AJJs lies in the absence of boundaries for the fluxon moving inside. Further, due to the closed topology of the annular Josephson junctions, it is possible to permanently trap the fluxon in it and study fluxon dynamics with minimum complications. Various techniques for creation and detection of fluxons in the AJJ will be discussed below.

There are several means of detecting Josephson vortices in the annular Josephson junctions. The simplest is to measure a current-voltage characteristic using the scheme depicted in Fig. 2.7. Characteristic vertical current step for a small non-zero voltage indicate trapped a fluxon inside the AJJ (see Fig. 2.8). In the case of several oscillating fluxons in the AJJ, the characteristics form of the current-voltage dependence stay the same but the maximum voltage scales proportionally with the fluxon number $V_{max} = (n\Phi_0 c_0)/L$.

Critical current diffraction patterns

Another method for fluxon detection is to measure a dependence of the critical current of the AJJ versus an in-plane magnetic field $\vec{H}$. Observation of a characteristic minimum of the critical current around the zero magnetic field (see Fig. 2.9) also provides an evidence of having the Josephson vortex inside the AJJ [MMF98].

Microwave radiation measurements

The third way can be realized by detecting a direct microwave radiation of the resonant fluxon motion inside the annular Josephson junction. As the fluxon carries a net Φ_0 magnetic flux, its oscillations with the frequency ν in the AJJ create cyclotron radiation at the same frequency. This radiation can be detected by coupling a microwave antenna to the AJJ. The obvious problem here is that the power of radiation from the single fluxon oscillations can be very low so the use of a low-noise microwave amplifier with sufficient gain is required to resolve a tiny microwave signal.

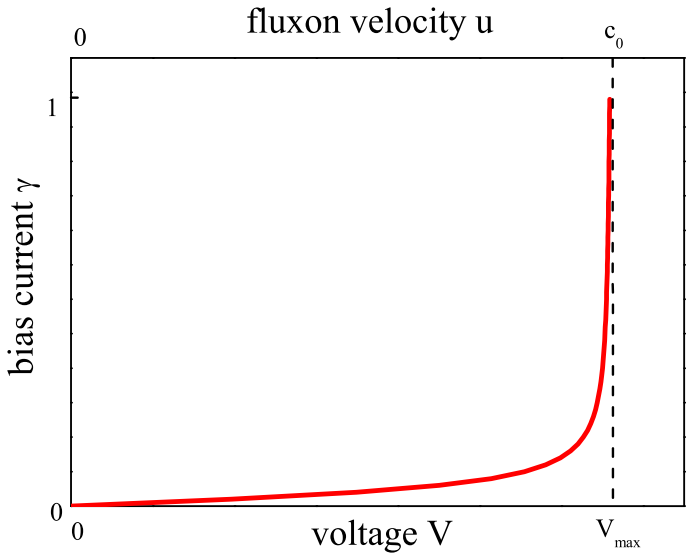

Figure 2.8: An ideal current-voltage characteristics of the annular Josephson junction with a trapped fluxon inside for the damping $\alpha = 0.025$. Calculated numerically using the perturbed sine-Gordon equation (2.22).

Measurements of current-voltage characteristics for AJJs is a simple and reliable technique of investigating fluxon dynamics. However, in case of long junctions with $L \sim 1$ mm and longer, it is hard to extract all needed information from simple IVCs as it becomes progressively complex to measure accurately enough small voltages on the scale of nanovolts across the AJJ with a single oscillating fluxon. Such detection of the single fluxon radiation has been performed in the case of a linear Josephson junction in [MBM93]. To our knowledge, there were no experiments conducted on detection of fluxon radiation from the AJJ and comprehensive studies of the later. The only know research which involves this topic was described in [KV05], where the AJJ was used in order to construct a low-temperature microwave clock generator. There, the oscillating fluxon was employed as a heterodyne on-chip microwave source with a specific microwave antenna coupled to the junction. The detailed results on microwave radiation measurements of fluxon oscilla-

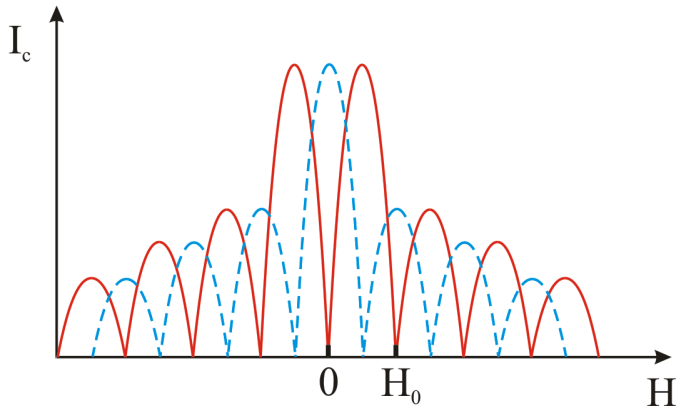

Figure 2.9: A typical Fraunhofer diffraction pattern for the critical current of an AJJ versus the in-plane magnetic field H. The blue dashed line depicts the situation of the fluxon-free AJJ. The red line corresponds to the case with a single fluxon trapped in the AJJ.

tions in the AJJ will be presented in the Chapter 3.

2.1.7 Creating a fluxon in annular Josephson junctions

One can create a single Josephson vortex inside ring-shaped Josephson junctions by different means. The simplest one is to cool down the sample several times in a small magnetic field and hope to trap a single fluxon during one of these cooldowns [MAK08] (a so-called "try and pray" method). Another approach is to apply a certain dc current to the current injectors into the top electrode of the AJJ [Ust02]. The later way is much more reliable than the first one.

However, the injection current creates an additional inhomogeneity in the junction and perturbs the current-voltage characteristics, thus, making the task to analyze the internal fluxon dynamics more complex. The simple understanding of this one can obtain from considering the current injectors as an additional current (magnetic) dipole in the AJJ. Due to solitonic nature of the fluxon, it does not interact with the mentioned dipole except for a phase shift. However, other excitations

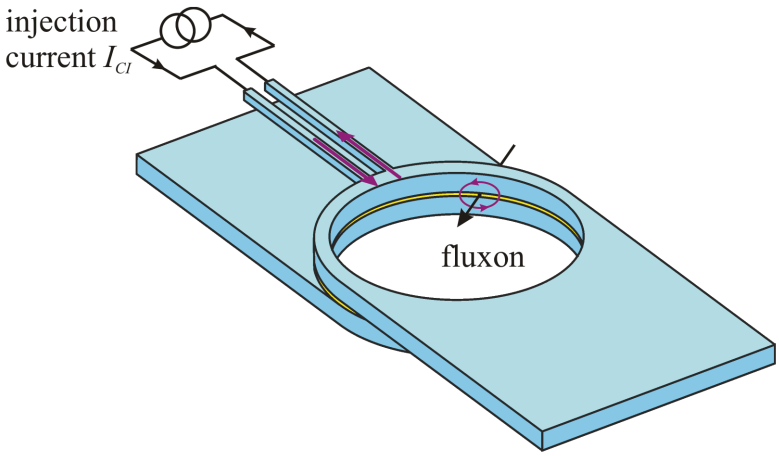

Figure 2.10: Fluxon creation in an annular Josephson junction by a local current dipole. Purple lines show the flow of electrical currents.

as, for example, plasma waves can emerge and serve as intermediate interaction medium between the dipole and the fluxon. Thus, the whole fluxon dynamic and the final structure of the zero-field step can become complicated.

The third method, the most complicated and reliable at the same time, considers using a low-temperature laser (or electron) scanning microscope in order to create a local hot-spot in the AJJ and, thus, locally breaking superconductivity. Applying a small magnetic field, at the same time, allows to insert a fluxon through this local hot-spot. Then, the laser is switched off, the hot spot vanishes and superconductivity recovers leaving the fluxon trapped inside the annular Josephson junction.

2.1.8 Resonant modes in long Josephson junctions

Resonant modes in long Josephson junctions can arise due to several reasons. In the case of linear junctions, the simplest reason is the pres-

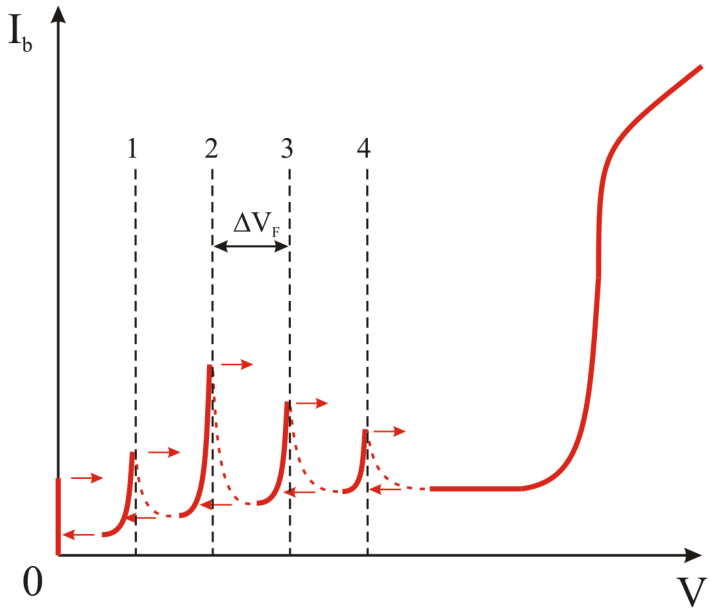

Figure 2.11: The schematic view of Fiske steps on current-voltage curve of a long Josephson junction at a nonzero in-plane magnetic field. Dashed lines show instable parts of the curves. Arrows indicate voltage jumps.

ence of the junction boundaries which can effectively form a distributed Fabri-Perot resonator for electromagnetic waves in the junction [Fis64]. These resonances appear as vertical voltage steps when the frequency of the Josephson currents (spatially modulated in the case of nonzero in-plane magnetic field) matches the frequencies of electromagnetic standing waves in the junction (see Fig. 2.11). The series of Fiske steps appear at voltages $V_n = (n\Phi_0 c_0)/(2l)$ so they are equidistant with a voltage separation $\Delta V_F = (\Phi_0 c_0)/(2l)$.

For the annular Josephson junctions, the situation changes a bit due to the absence of boundaries (and absence of corresponding reflections) which can form a cavity for electromagnetic waves. One cannot insert the fluxons into the junction by applying the in-plane magnetic field.

Plasma waves resonances

The Josephson vortex is predicted [MS79] to excite plasma modes in a long Josephson junction with spatially periodic potential if it moves at a velocity higher than a certain threshold value:

$$u_{thr} = 1/\sqrt{1 + (2\pi/a)^2}, \tag{2.33}$$

where a is the potential period (or, $a = l$ in the case of the ideal uniform AJJ in the in-plane magnetic field, which creates an additional non-uniform potential for the fluxon). At velocities above this threshold, a frequency and a wavenumber of the excited plasma waves depend on the fluxon velocity. The excited plasma waves form a certain additional effective potential for a moving fluxon and can provide attractors for certain fluxon frequencies. This interaction occurs only when the fluxon is able to emit plasma waves by itself. Once the wavelength of excited plasma waves times an integer equals the length of the junction, a resonance occurs. This resonant-like interaction leads to an appearance of series of vertical constant voltage (or frequency) steps arising from the smooth ideal zero-field step at fluxon velocities:

$$u_m = \sqrt{\left(1 - \frac{b}{ma}\right)^2 + \left(\frac{b}{2\pi m}\right)^2}, \tag{2.34}$$

where m is an integer, b is the spatial period of the fluxon chain ($b = l$ in the case of a single fluxon), a is the spatial period of inhomogeneities in the AJJ (again, $a = l$ in the case of the non-uniform AJJ) [UMG99].

In the same paper it was mentioned that for very low damping $\alpha \ll 1$ the higher fluxon harmonics may contribute to the excitation of plasma waves (2.35). Thus, the radiation threshold relation transforms into:

$$u_{thr} = 1/\sqrt{1 + (2\pi n/a)^2}, \tag{2.35}$$

where n is the harmonic number. An interesting idea can be to upgrade the theory of the fluxon fine structure (2.34) in respect of this new threshold value (2.35). This is especially relevant for milli-Kelvin temperatures where the fluxon damping is extremely low, so many high harmonics can contribute to the excitation process of plasma waves.

Whispering gallery modes

Another possibility to generate plasma waves is to use a wide annular Josephson junction which is effectively two-dimensional. As the Josephson vortex is a topological soliton, the vortex phase string moves almost rigidly across the junction's width. At a certain threshold fluxon velocity, the tangential projection of the phase velocity of the outer edge of the string can exceed the Swihart velocity while the average speed of the fluxon is still below c_0. This gives rise to a well-known Cherenkov radiation of linear plasma waves in the AJJ [KYV98, WUV00]. Such type of resonances are usually called *whispering gallery modes* as they originate from the similar acoustic resonances in the famous Whispering gallery of St. Paul's Cathedral.

2.2 Flux Qubit

A qubit is a quantum system with two states which can be distinguished by a measurement. Natural two-level system are rare and can be found in photonic crystals, or as two-level fluctuators and nuclear spins in solids. Other approaches for artificial qubits rely on employing a nonlinear energy spectrum to isolate two lowest quantum states. Josephson junctions are a reasonable choice for making a qubit because of inherent nonlinearity, absence of dissipation and well developed fabrication techniques. Generally, at least three types of superconducting qubits can be distinguished: charge qubits, phase qubits and flux qubits. All of them are exploiting the Josephson nonlinear physics to some extent.

2.2.1 Quantum bits and quantum computing

Quantum bits are considered as analog of classical bits in quantum mechanics. Their main difference is that while a classical bit can have only two states: 0 and 1, a quantum bit can sustain any linear superposition of 0 and 1. Any two-level quantum system can serve as a qubit which basically means - anything can work as a qubit, so the problem is not to find or create a qubit but to find a **good** one. To be a **good** qubit means to fulfill a number of certain conditions introduced by DiVincenzo [DiV00] and, accordingly the called DiVinchenzo criteria:

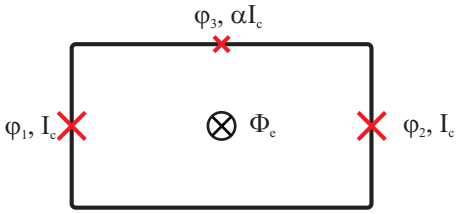

Figure 2.12: Sketch of a flux qubit. The red crosses denote Josephson junctions, the black line denotes a superconducting loop.

1) a scalable physical system with well characterized qubits;

2) the ability to initialize the state of the qubits;

3) long relevant coherence times, much longer than the gate operation times;

4) a "universal" set of quantum gates;

5)a qubit-specific measurement capability.

The flux qubit possesses (at least, potentially) all of these qualities. The main advantage of the flux qubit in comparison with the phase and the charge ones is that its coherence times are considerably longer. At the same time, the flux qubits are relatively small which allows to achieve better scalability on-chip.

2.2.2 Persistent current qubit

The flux qubit, or the persistent current qubit, was initially proposed and developed by Hans Mooij and his colleagues [Moo99, CNM03]. This superconducting quantum bit is based on the tunneling process of a Josephson phase between two neighboring shallow potential wells. Due to the such specific process, also illustrated by the Fig. 2.14, it is possible to realize a two-level quantum system. In reality, such an object can be implemented as a superconducting loop separated by three Josephson junctions: two of the same critical current $I_{c1} = I_{c2} = I_c$ and one with the critical current alpha times smaller than others $I_{c3} = \alpha_q I_c$ (see Fig. 2.12).

2.2.3 Flux Qubit Potential

Using the flux quantization condition (1.18) for the superconducting loop intersected by the three Josephson junctions (Fig. 2.12) one can write:

$$\Sigma\varphi_i + \frac{2\pi\Phi_e}{\Phi_0} = 2\pi N, \tag{2.36}$$

where N is the number of flux quanta trapped inside the qubit loop. Combining this equation with the Josephson potential energy (2.3) yields the total energy U of the qubit loop:

$$U = E_J \left(2 + \alpha - \cos\varphi_1 - \cos\varphi_2 - \alpha\cos(2\pi f - \varphi_1 - \varphi_2)\right), \tag{2.37}$$

where E_J is the Josephson energy of each of the large junctions and $f = \Phi_e/\Phi_0$ is the magnetic frustration. Here, we neglect the energy stored in the magnetic field generated by the geometrical inductance of the flux qubit loop. This assumption is valid if the geometrical inductance is much smaller than the Josephson inductance $L_g \ll L_J$.

The potential given by (2.37) does not depend on the number of trapped flux quanta, has two internal degrees of freedom and is 2π periodic in both. By means of mathematical analysis it can be shown that the two-well configuration (see Fig. 2.13), required for the flux qubit, is achievable only within the range $0.5 < \alpha < 1$.

A magnetic moment generated by the current in the flux qubit loop can be coupled to a external magnetic field (flux bias) and tilt the double well potential. This happens for all flux biases $f \sim 0.5$ when the two persistent current states are no longer degenerate and their energy difference is:

$$\hbar\epsilon = 2I_p(\Phi_e - \Phi_0/2) = 2I_p\Phi_0(f - 0.5), \tag{2.38}$$

where ϵ is also called the *asymmetry energy*.

The dynamics of the flux qubit system is described by an additional kinetic energy term T. To derive this, the charge energy of the islands between the Josephson junctions should be taken into account:

$$T = \frac{1}{2}\sum_i C_i V_i^2 = \frac{1}{2}\left(\frac{\Phi_0}{2\pi}\right)^2 \sum_i C_i\dot{\varphi}^2, \tag{2.39}$$

where C_i denotes the Josephson junction capacitance while neglecting the capacitances of the islands to the ground.

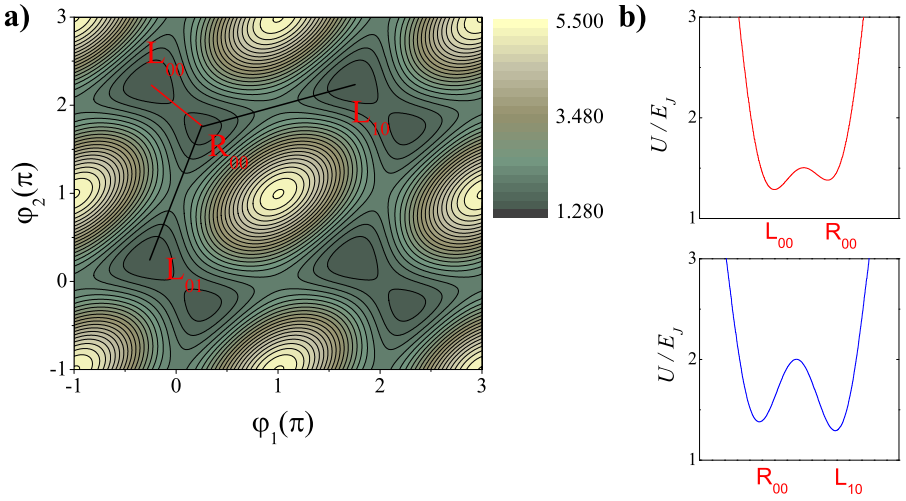

Figure 2.13: Josephson energy of a flux qubit in phase space for $\alpha = 0.75$ and $f = 0.490$. **a)** Energy is plotted as a function of the Josephson phase differences φ_1 and φ_2. There are two minima in each unit cell (with the periodicity of 2π) denoted with R_{00} and L_{00}. **b)** Energy profiles along the red and black trajectories. The trajectory between R_{00} and L_{00} is indicated in red; between R_{00} and L_{10} - in blue. For the chosen parameters the tunneling rate between different cells is greatly suppressed.

2.2.4 Quantum mechanical description

Knowing the kinetic energy term T and the potential energy U, the classical Hamiltonian of the flux qubit can be derived. Considering the classical phases and their conjugate momenta as operators, the following quantum mechanical Hamiltonian can be obtained:

$$H = \frac{1}{2}\frac{P_m^2}{M_m} + \frac{1}{2}\frac{P_p^2}{M_p} + E_J\left(2 + \alpha - 2\cos\hat{\varphi}_m\cos\hat{\varphi}_p - \alpha\cos(2\pi f + 2\hat{\varphi}_m)\right), \tag{2.40}$$

where the momentum operators are $P_p = -i\hbar\partial/\partial\varphi_p$ and $P_m = -i\hbar\partial/\partial\varphi_m$, the mass terms are $M_p = 2C(\Phi_0/2\pi)^2$ and $M_m = 2C(1+2\alpha)(\Phi_0/2\pi)^2$ and the phases are defined as follows:

$$\hat{\varphi}_m = (\hat{\varphi}_1 - \hat{\varphi}_2)/2, \hat{\varphi}_p = (\hat{\varphi}_1 + \hat{\varphi}_2)/2. \tag{2.41}$$

By numerical simulation of (2.40) the eigenstates and eigenenergies

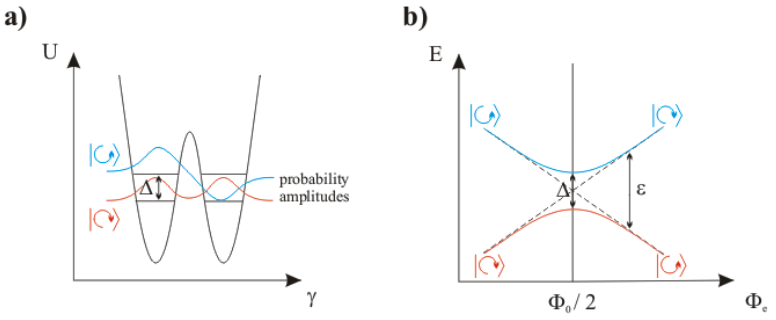

Figure 2.14: a) The cross section of the flux qubit potential in the L_{00}-R_{00} direction. The red (the ground state) and the blue (the first excited state) lines illustrate an approximate Josephson phase probability amplitudes. The minimum energy difference between these two states is Δ. **b)** The energy diagram for the first two quantum levels in the flux qubit. The symbols in *bra* and *ket* show the sign of the corresponding persistent current, ΔE is the energy splitting of the flux qubit detuned from the frustration point.

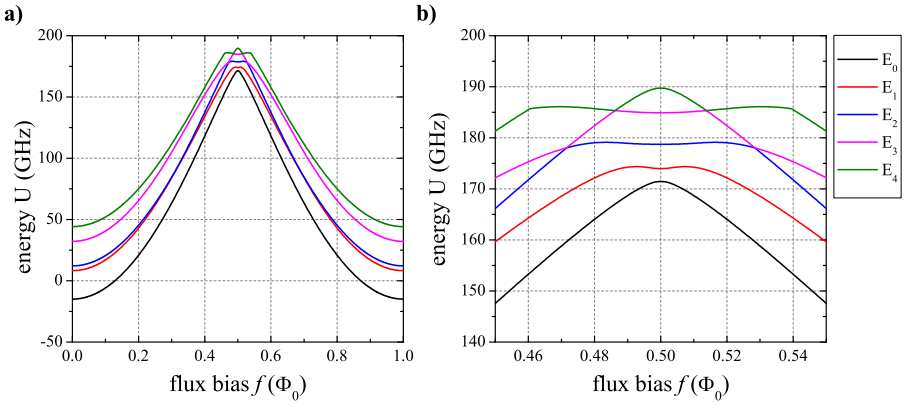

Figure 2.15: a) The typical dependence of energy levels for the flux qubit versus the flux bias. The modeled qubit parameters are: $\alpha = 0.54$ and $I_c = 380$ nA. The whole picture is Φ_0 periodic. **b)** Zoom into the area around the half frustration point $f = 0.5$.

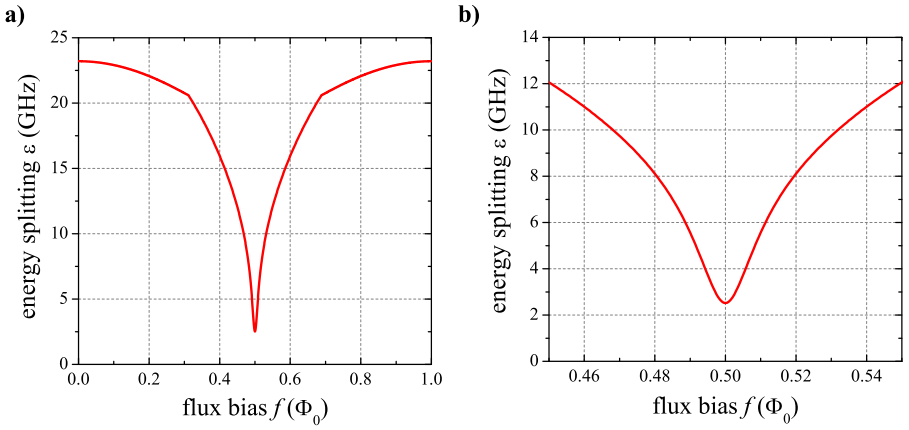

Figure 2.16: **a)** The dependence of the energy splitting $\Delta E = E_1 - E_0$ between the ground (zero) and the first excited (one) flux qubit states. The modeled qubit parameters are: $\alpha = 0.54$ and $I_c = 380$ nA. **b)** Zoom into the area around the frustration point $f = 0.5$. The minimum qubit splitting is around $\Delta = 2.3$ GHz.

of the flux qubit can be found. This simulation is based on a truncation of H to a discrete grid in a phase space and numerical diagonalization of the resulting Hamiltonian matrix. The result of such numerics is illustrated in Fig. 2.15 for the eigenenergies of the flux qubit versus the flux bias. As it can be seen, the qubit potential is symmetric at half frustration and the two persistent currents of the ground.

From the point of view of quantum computing, we are interested in the two lowest ground states which we would like to use as a qubit basis. The energy splitting ΔE between these two state are shown in Fig. 2.16 for the typical flux qubit parameters. The lowest possible energy splitting is usually called the qubit gap and is denoted as Δ in reference to the notation used for the description of tunneling systems (which basically the flux qubit is).

It is also possible to calculate the averaged amplitudes of the persistent current in the flux qubit loop corresponding to different states. This knowledge is particularly important for the fluxon readout. Illustrations for persistent currents of the ground and the first excited states are given in Fig. 2.17. In the classical situation, at half frustration these

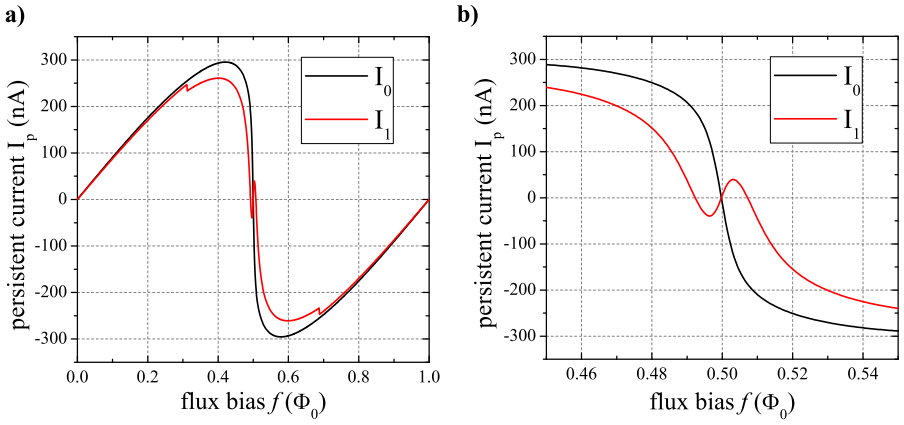

Figure 2.17: a) The dependence of the persistent current I_p for the ground (black line) and the first excited (red line) flux qubit states. The modeled qubit parameters are: $\alpha = 0.54$ and $I_c = 380$ nA. **b)** Zoom into the area around the frustration point $f = 0.5$

two states (clockwise and counterclockwise currents) are degenerate as the potential is symmetric at this point. In the quantum mechanical description, the degeneracy is lifted.

To simplify the description of qubits, the truncation to the two lowest energy levels is commonly used. This approach is based on the assumption that the transition between the first two levels requires the energy which is, at least, several times less than the energy required to reach the qubit's second excited state. This usually holds in the vicinity of the degeneracy point for the flux qubits. A two-level Hamiltonian can be constructed using the gap Δ and the asymmetry energy ϵ:

$$H = \frac{\hbar}{2}\Delta\sigma_x + \frac{\hbar}{2}\epsilon\sigma_z = \begin{pmatrix} \epsilon & \Delta \\ \Delta & -\epsilon \end{pmatrix}, \tag{2.42}$$

where σ_x and σ_z are the first and the third Pauli matrices. This Hamiltonian also corresponds to a 1/2-spin particle in an external magnetic field and can be diagonalized by a unitary rotation around y axis $A = \exp(i\theta\sigma_y)$ by the angle $\tan(2\theta) = \Delta/\epsilon$. In the rotated basis, the flux qubit Hamiltonian reads:

$$\tilde{H} = A^\dagger H A = \frac{\hbar}{2}\sqrt{\Delta^2 + \epsilon^2}\sigma_z, \tag{2.43}$$

where the qubit transition frequency is identified as $\omega_q = \sqrt{\Delta^2 + \epsilon^2}$.

2.2.5 Driven qubit

An external drive is usually required to excite transitions between the quantum levels in a qubit. In the case of a flux qubit, it is usually implemented as a microwave signal coupled to the former. This signal is an oscillating electromagnetic field and can be treated as such in the Hamiltonian:

$$H_d = \frac{A}{2}\cos(\omega_d t + \phi)\sigma_z, \tag{2.44}$$

where A is the amplitude of the drive. One can apply a rotation transformation to H_d as it was done in (2.43):

$$\tilde{H_d} = A^\dagger H_d A = \frac{A}{2}\cos(\omega_d t + \phi)\left[\frac{\epsilon}{\omega_q}\sigma_x + \frac{\epsilon}{\omega_q}\sigma_z\right]. \tag{2.45}$$

By adding the drive Hamiltonian $\tilde{H_d}$ to the flux qubit Hamiltonian $\tilde{H}$ in the rotated frame and applying the so-called *rotation wave approximation* [MMS01] to the full Hamiltonian one can find the solution for the qubit state in the following form:

$$U(t) = \exp(-i\vec{\Omega}t \cdot \vec{\sigma}/2), \vec{\Omega} = \begin{pmatrix} \frac{A\Delta}{2\hbar\omega_q}\cos\phi \\ \frac{A\Delta}{2\hbar\omega_q}\sin\phi \\ \omega_q - \omega_d \end{pmatrix}, \tag{2.46}$$

where $\vec{\Omega}$ defines the rotation axis. In the case of a resonant drive, when $\omega_q = \omega_d$, the state vector describes rotations with the frequency:

$$\Omega = \frac{A\Delta}{2\hbar^2\omega_q}, \tag{2.47}$$

which is known as the Rabi frequency. The rotations occur around the x- or y-axis depending on the starting phase ϕ of the drive signal. In a more general situation of an off-resonant drive $\omega_q \neq \omega_d$, the state vector also precesses around the quantization axis of the rotation frame and the generalized Rabi frequency is:

$$\Omega = \sqrt{\left(\frac{A\Delta}{2\hbar^2\omega_q}\right)^2 + (\omega_q - \omega_d)^2}. \tag{2.48}$$

A simple and important application of the presented results is that, if one applies a continuous resonant drive in the ground state $\psi = |0\rangle$, the qubit oscillates between the ground and the first excited states and its average corresponds to a mixed state $\psi = (|0\rangle + |1\rangle)/\sqrt{2}$. Obviously, the persistent current of the mixed state is different from the one of the ground state and this allows to detect the quantum excitation the qubit in experiment.

2.2.6 Qubit readout techniques

An essential part of any qubit circuit is a readout scheme. It is extremely important for quantum computation that a given readout method of a qubit is of high-fidelity, fast and weakly perturbing. Since the invention of quantum bits, scientists have actively searched for new and better ways of acquiring information from quantum bits.

Some of the ways to readout the qubit are called *destructive* as they destroy the quantum state during the readout process. For instance, the readout process of a phase qubit [Mar09] through an escape of a Josephson phase from a potential well in rf-SQUID is the classic example of a destructive readout. Other, so-called *non-destructive*, methods allow to learn something about a quantum system without complete destruction of its state. These methods are usually based on a dispersive interaction between the qubit and some other well-defined classical subsystem, the state of which is dependent on the state of the investigated qubit. This second system can be, for instance, a classical harmonic oscillator (an electromagnetic resonator) whose frequency slightly depends on the qubit state. Thus, measuring the amplitude or the phase of this oscillator at a particular frequency, we project the qubit quantum state onto a certain basis and acquire information about it. Ultimately, such a readout usually destroy the phase of the qubit during the projection but leaves the qubit energy unperturbed, thus holding the name of *non-destructive* readout (which is not completely true, as the qubit phase is usually changed after the readout).

Destructive readout

The typical example of a destructive readout is the one used for the phase qubits formed by a Josephon junction enclosed in a loop. By tilting the phase qubit potential by an external magnetic field, one may force a tunneling event of the Josephson phase linked with the quantum state of the phase qubit. This tunneling event can be recorded by measuring a magnetic field generated by the qubit. Different quantum states correspond to different external fields required for the tunneling events to happen. Thus, by placing a sensitive magnetic detector (a dc-SQUID, for instance) nearby the phase qubit and measuring the magnetic field of the qubit versus the tilt of the qubit potential, one can distinguish different quantum states. Details of the described procedure can be found elsewhere [Mar09].

Unfortunately, once the tunneling event in the phase qubit happens, the quantum state is destroyed. This is why this method for reading out of the phase qubit is called destructive.

Dispersive readout

Another approach can be realized with the use of so-called dispersive readout. Usually, it is based on a coupling of an investigated qubit with an electromagnetic LC resonator, in other words, with a harmonic oscillator [WSS05, SVD06]. The coupling can be magnetic or electric, depending on the type of the qubit. For flux qubits, the magnetic coupling is preferable because of a significant magnetic dipole moment of the flux qubits.

By exciting the resonator and measuring its resonance frequency, one projects the qubit state onto the energy basis of the coupled resonator. In this case, different quantum states in the qubit directly correspond to the slightly different resonance frequencies of the resonator. One can explain this by taking into account a variable inductance of the Josephson junctions in the flux qubit loop which depends on the quantum state of the flux qubit itself. Thus, a change in the quantum state of the qubit introduces a small deviation in a total inductance of the coupled resonator, shifting its respective resonance frequency.

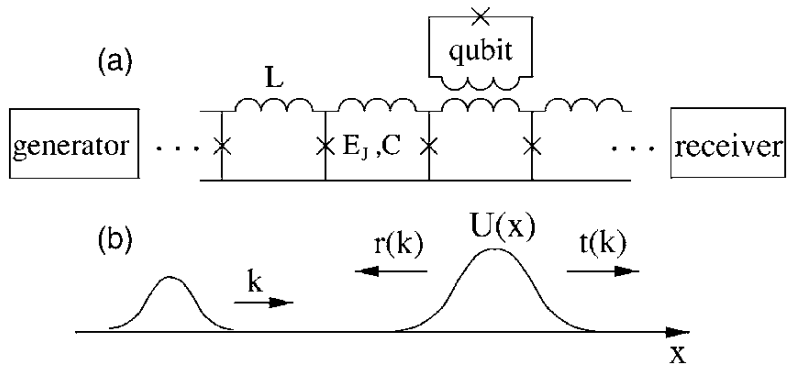

Figure 2.18: Illustration of the initial idea by Averin et al. [ARS06] of a fluxon readout of a flux qubit. The fluxons are meant to be periodically injected in the JTL with momentum k by the generator and their scattering characteristics (transmission and reflection coefficients $t(k)$ and $r(k)$ are registered by the receiver. The potential $U(x)$ is controlled by the measured qubit.

The Fluxon Readout

Our interest is to develop a new type of dispersive readout for flux qubits. It is based on magnetic coupling between a flux qubit and a moving fluxon. This approach should preserve most of the advantages of the non-destructive readouts and, at the same time, provide a better shielding of a qubit from noisy environment and a compatibility with rapid single flux quantum (RSFQ) superconducting electronics. The latter is viewed as a major step towards a full-scale implementation of a quantum computer. Chapter 4 is fully dedicated to theoretical and experimental investigations of this path.

Initially, the idea of fluxon readout was proposed in Ref. [ARS06]. A theoretical treatment for a problem of ballistic fluxon scattering on the flux qubit potential was given in this paper. Figure 2.18 illustrates this process. An important peculiarity is that a Josephson transmission line is considered to be discrete which matches better the general

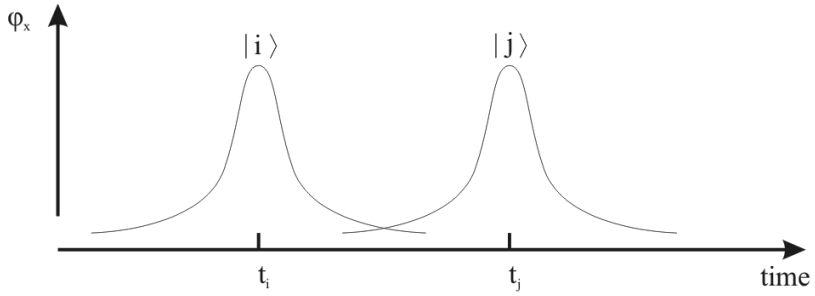

Figure 2.19: Illustration of the information acquisition process by the fluxon readout in the time-delay mode. The fluxon packet is shifted in time (frequency) by the time t_i dependent on the state $|i\rangle$ of the measured qubit.

RSFQ approach. It is assumed that one can inject separate fluxons at a fixed rate f into this JTL by a specific generator and then detect them by a receiver at the other end without any reflections. The qubit is considered to be inductively coupled to the JTL (see Figure 2.18). In each qubit's state $|i\rangle$, there is a different scattering potential $U(x)$ for the fluxons propagating through the JTL. Different realizations $U(x)$ produce different scattering coefficients $t(k)$ and $r(k)$. Since they depends on the state $|i\rangle$ of the measured system, scattered fluxons carry information about the qubit state.

Naturally, two regimes of the fluxon readout can be distinguished: a time-delay detection mode and a transmission detection mode. Figure 2.19 provides an illustration for the time-delay mode, when the qubit is weakly coupled to the JTL. The transmission detection mode operates in the regime than a useful signal is provided by the presence (successfully propagated through the JTL) or the absence (reflected by the qubit potential) of the fluxon at the detector. Obviously, this regime requires strong coupling (and a strong unwanted fluxon backaction on the studied qubit) of the qubit with the JTL or (and) extremely low kinetic energies of the fluxon itself. Overall, the time-delay method is preferable over the transmission detection for the fluxon readout in most circumstances.

The fluxon readout potentially can also have several working regimes depending on the velocity of fluxons in the JTL. The best one (from the theoretical point of view) is the situation when the fluxon is in the "nonrelativistic" regime with its kinetic energy E_f smaller than the lowest plasmon energy $\hbar\omega_p$:

$$E_f = \hbar\omega_p(2u/c_0\beta)^2, \tag{2.49}$$

where the parameter $\beta^2 = (4e^2/\hbar)\sqrt{L/C}$ is the wave resistance of the JTL. Here, $\beta^2 \ll 1$ should be small enough in order to preserve the quasi-classical dynamics of fluxons. In case when $\beta^2 \geq 8\pi$, $\sqrt{L/C} \geq h/e^2 \sim 25$ kΩ, quantum fluctuations of the field φ completely destroy the quasiclassical excitations of the junction [Raj82]. Equation (2.49) suggests that for $u < c_0\beta/2$ the fluxon cannot emit a plasmon even when it is scattered by inhomogeneities of the JTL. The latter is especially good for the qubit protection as it shields the qubit from outer world excitations which may come through the JTL itself. This happens because the plasma gap in the dispersion relation of JTLs for linear waves does not allow the propagation of waves with the frequencies below plasma one $\omega < \omega_p$ and, at the same time, for the considered case of "nonrelativistic" fluxons, plasma waves cannot be emitted due to the fluxon scattering on imperfections in the JTL. Thus, the JTL works as a specific filter, allowing the qubit to be disturbed by fluxons only. The latter is considered as a major advantage of the fluxon readout versus the dispersive readouts via linear resonators, where linear excitations can, in principle, propagate via the resonator line.

The fluxons in the JTL can also be quantum objects as it was already proven in experiment [WLU03] and the fluxon readout can be in quantum regime for the case of "nonrelativistic" fluxons. For this one should consider a couple of limitations: the fluxon energy should be larger than the ambient temperature $E_f > k_BT$, and the fluxon size in the discrete JTL should not be smaller than a single JTL cell. The latter imposes another restriction on the fluxon energy $E_f < (e^2/C)(\lambda_J/4)$. Unfortunately, for the standard niobium trilayer process, it is possible to meet these both requirements only by implementing Josephson junctions with sub-micron lateral sizes.

Also, the authors of Ref. [ARS06] showed an intriguing possibility to

use the fluxon as an ultimate quantum non-demolition readout when the fluxon injection frequency is matched to the qubit oscillation frequency, so that the individual acts of measurements are done when the qubit density matrix is nearly diagonal in the σ_z basis, and the measurement back action does not introduce a dephasing in the oscillation dynamics of the flux qubit.

Using the described model [ARS06], in Ref. [HFS07] useful estimations of fluxon readout parameters employing RSFQ type of discrete JTLs were given. In particular, the dephasing time due to perturbation of the flux qubit by passing fluxons for reasonably long transmission lines were estimated to be of the order of $T_2 \sim 20$ μs.

In the case of relativistic fluxons, with the respective velocities close to the Swihart velocity $u \sim c_0$, the fluxon can also generate linear plasma waves while scattering on the JTL inhomogeneities [MS79]. This may decrease coherence times of the coupled qubit, however, there is also a hidden experimental advantage of relativistic fluxons is that they are much more stable at low temperatures $T \sim 50$ mK required for the qubit experiments. The latter turns out to be crucial for an experimental implementation of the fluxon readout.

In our experiments, continuous annular Josephson junctions were used instead of the discrete JTL. This provides a simpler experimental set-up as there is no need in complex RSFQ drivers required for creation and detection of fluxons. At the same time, such an approach preserves the general scheme of the fluxon readout and allows to study physical principles of the latter.

2.3 Conclusions

In the first part of this chapter, the classical theory on Josephson vortices and their implications in dynamics of long Josephson junctions have been presented. Various creation and detection schemes for fluxons were discussed. The problem of fluxon resonant modes and their interaction with linear plasma waves was described.

In the second part, the quantum mechanical theory of the flux quantum bit has been introduced. It was shown that, under the external resonant drive, the flux qubit oscillates between its ground and first

excited states with the Rabi frequency which depends on the drive amplitude and the detuning of the drive frequency from the qubit transition frequency. Conventional readout techniques for qubits were briefly described and the idea of fluxon readout was introduced.

3 Measurements of fluxon radiation

As theoretically described in the previous chapter, magnetic flux quanta Φ_0 can exist in an isolated form in long Josephson junctions. They are known as Josephson vortices or *fluxons*. To employ the fluxon readout scheme for superconducting qubits, it is important to learn how to experimentally create, control and detect fluxons in long Josephson junctions.

In this chapter, experiments on the first-time detection of a single fluxon's radiation from an annular Josephson junction (AJJ) are described leaving the topic of an actual interaction of a fluxon with a superconducting qubit for the next chapter. In the first section a brief description on the fabrication techniques of niobium Josephson junctions, experimental methods and equipment is given. In the second part of this chapter, actual measurements of zero-field steps in various samples are presented along with theories required for a proper explanation and understanding of observed phenomena. A possibility to resolve a fine structure of zero-field steps via measurements of microwave radiation of the oscillating fluxon in the AJJ is demonstrated. Studies of the fluxon radiation linewidth are carried out. Finally, a phase-locking experiment for the fluxon oscillator capable of locking single fluxon oscillations to an external reference signal were performed.

The first task in order to build a working fluxon readout is to detect the microwave radiation from oscillatory movement of the fluxon in the AJJ. The proposed experimental scheme is illustrated in Fig. 3.1. All later experiments will be based on the shown scheme. Specially designed current injectors were used in order to controllably create and destroy fluxons in the AJJ. A microstrip line, capacitively coupled to the AJJ, functions as a microwave antenna, allowing to pick up electromagnetic radiation from the moving fluxons.

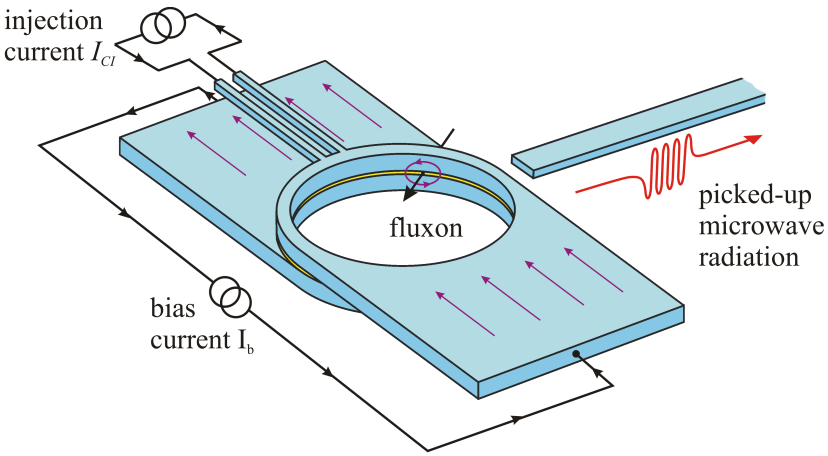

Figure 3.1: The schematic view of an annular Josephson junction with current injectors for creating fluxons and a capacitively coupled microstrip antenna for receiving fluxon microwave radiation.

3.1 Experimental setup and technique

For a theoretician in physics, usually it is enough to invent an idea and describe it in reasonable mathematical terms to be successful. For an experimentalist, besides the idea itself, it is needed to build some robust manifestation of this idea, stable enough to survive in the imperfect real world. In the area of superconducting thin film technology, this enterprize starts from understanding a particular fabrication process allowing one to fabricate a structure similar to the one shown in Fig. 3.1. Then, it continues with making estimations for the suitable designs, fabricating them and, finally, measuring them with a carefully built experimental setup.

3.1.1 Sample design and fabrication

The conventional processes of fabricating long Josephson junctions make use of thin-film technology, historically developed for the semiconductor

industry. It includes making metal masks with photolithography, using the latter for exposing photoresist masks on silicon chips and patterning structures. Subsequent sputtering of certain metal allows one to create a thin multilayer of different compounds with the desired dimensions. In our case, several external foundries have been used in order to fulfil this important task. Mainly, two have been used. The first one was Hypres Inc., Elmsford, NY 10523, USA, which is a commercial company specialized in delivering superconducting schemes for rapid single flux quantum (RSFQ) electronics. The second one was the IPHT "FLUXONICS" foundry in Jena, Germany, with the same type of specialization. Both foundries employ the conventional $Nb/AlO_x/Nb$ trilayer process in order to form Josephson junctions with additional three layers of metallization for wiring purposes.

Fabrication process

Here, a brief technical description of the conventional $Nb/AlO_x/Nb$ trilayer process for the critical current density of $j_c \sim 1$ kA/cm^2 is given. The process exploited at the IPHT Jena foundry is used as a reference. The layer structure for IPHT Jena and for Hypres is almost the same, however, some particular numbers for layers thicknesses, minimal lateral widths and some other parameters may differ. For other typical critical current densities like $j_c \sim 30$ A/cm^2 the layer structure is usually the same, with insignificant deviations.

The general picture of a cross section of a superconducting thin-film structure consisting of two layers of metallization, a Josephson junction, a resistive shunt and a bonding pad is shown in Fig. 3.2. The third layer of metallization and a ground plane (a special "zero" layer of metallization) are omitted here because they do not add anything new to the whole structure (only complicate it). Also they have been rarely used for the real designs. The fabrication of such a chip usually begins from taking a silicon substrate (usually 400-500 μm thick) with an oxidized surface (shown in grey color). During the next step, one usually patterns and sputters the layer M1 made of superconducting niobium (shown in red color) and the trilayer structure $Nb/AlO_x/Nb$ (shown in blue color) on top of it. Building of the trilayer usually consists of sev-

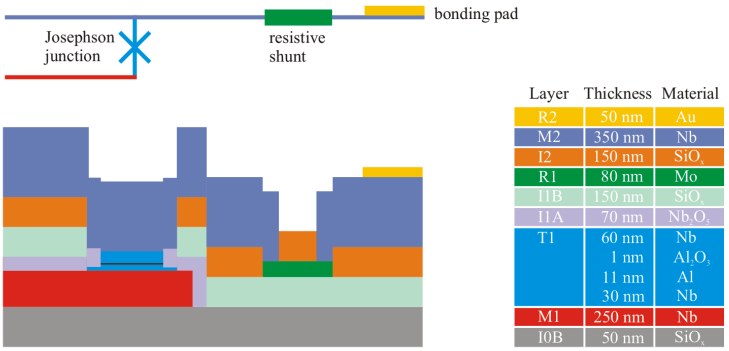

Figure 3.2: Cross section of RSFQ sandwich for the conventional $Nb/AlO_x/Nb$ trilayer process with two layers of metallization. The equivalent scheme of the presented cross section is depicted on top.

eral steps: at the beginning one sputters a thick base Nb electrode, then an additional thin Al layer on top, then oxidize the aluminum to create a $d \sim 1$ nm thin tunnel barrier and concludes the process by sputtering a top niobium electrode. This comparatively complex process was chosen because of its reproducibility and good parameters of output Josephson junctions (j_c, R_N). The main reason for using aluminum for making Josephson junctions in niobium process is that it gives almost perfectly smooth tunnel barriers which are hardly achievable with other superconducting materials (including niobium).

After depositing the trilayer onto the chip, one usually performs spin-coating with a photoresist, patterning, chemical etching and a subsequent oxidization of the top electrode idle regions in order to create the isolation layer I1A made of Nb_2O_5 (shown in light purple color) to avoid parasitic superconducting shorts in parallel with the Josephson junction. This is a very important step for the whole process as these shorts may completely disrupt the performance of Josephson junctions. To ensure the insulation between M1 and the other metallization layers, the second layer of insulation I1B made of SiO_x is sputtered on top. When needed, structures out of a normal metal (here it is molybdenum

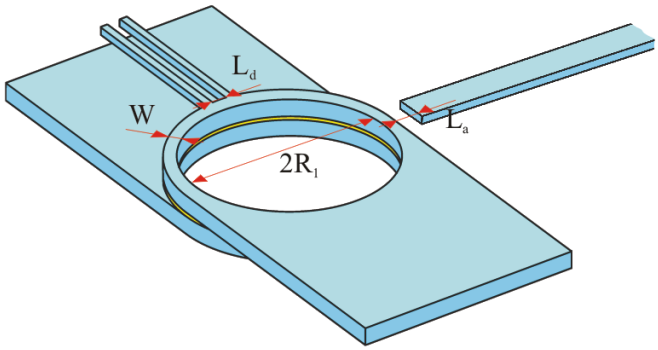

Figure 3.3: The general view of an annular Josephson junction, with current injectors for creating fluxons and a capacitively coupled microstrip antenna for detecting fluxon microwave radiation.

R1, shown in green color) may be placed to create resistive shunts. This may be used when it is necessary to break superconducting loops on the chip by inserting a normal metal shunt. The next step includes making the second layer of metallization M2 on top of the other layers. M2 connects the top electrodes of Josephson junctions with resistive shunts R1 and subsequent gold bonding pads R2. A more detailed description of these fabrication processes can be found elsewhere [FF, Hyp].

Designs and estimations

The general structure of samples for experiments is shown in Fig. 3.3. They usually consist of an annular Josephson junction with bias leads, current injectors, one or two microwave antennas and a specially designed loop for a later coupling of a superconducting qubit to the AJJ (not shown in Fig. 3.3). The next important step is to determine the preferred parameters and sizes of the described structures.

In order to estimate the fluxon properties in the annular Josephson junction, we need several parameters (see Section 2.1.1): the critical current density j_c, the specific capacitance of the Josephson junctions C_s, the normal state resistance R_N as well as the width of the long Josephson junction W and its length L. For the Hypres process, the

specific capacitance C_s can be estimated using the following approximation formula:

$$C_s = \frac{1.0}{24.7 - 2.0 \cdot \ln j_c} \ (\mathrm{pF}/\mu\mathrm{m}^2), \tag{3.1}$$

where j_c is the critical current density in $\mu A/\mu m^2$. This gives roughly $C_s = 0.05\ pF/\mu m^2$ for $j_c = 1\ kA/cm^2$ and $C_s = 0.037\ pF/\mu m^2$ for $j_c =$ 30 A / cm^2. These values are in good agreement with the experimental data.

For an experimental detection of the fluxon oscillations, the AJJ needs to be designed in such a way that the fluxon oscillation frequency lies in the acceptable range. The maximum oscillation frequency of the fluxon in the AJJ is:

$$\nu_0 = c_0/L, \tag{3.2}$$

where L is the circumference of the annular Josephson junction and c_0 is the Swihart velocity (the phase speed of light in the long Josephson junction). One also should keep in mind the frequency range of available low-noise cryogenic microwave amplifiers to make sure that the fluxon frequencies are in the working range. Basic available (at the time of designing first samples) cryogenic amplifiers had a bandwidth from 4 to 8 GHz and from 8 to 12 GHz. According to Eq. 2.19 we estimate the maximum velocity c_0 of the fluxon in the long Josephson junction for the given parameters and, thus, the maximum frequency of fluxon oscillations in the AJJ. For the process with the critical current density $j_c = 30$ A / cm^2 and $C_s = 0.037\ pF/\mu m^2$, using Eqs. 2.16,2.17,2.19, one gets:

$$\omega_p/2\pi = 25 \text{ GHz}, \lambda_J = 69\ \mu\text{m}, c_0 = 0.036\ c. \tag{3.3}$$

Then, it is easy to calculate that an AJJ length (full circumference) of about $L \simeq 1$ mm corresponds to a maximum fluxon oscillation frequency $\nu_r \simeq 11$ GHz. For the process with the higher critical current density $j_c = 1$ kA / cm^2 and $C_s = 0.05\ pF/\mu m^2$, one gets:

$$\omega_p/2\pi = 124 \text{ GHz}, \lambda_J = 12\ \mu\text{m}, c_0 = 0.031\ c. \tag{3.4}$$

It corresponds to the maximum fluxon oscillation frequency $\nu_r \sim 9.4$ GHz for the same junction length $L \sim 1$ mm.

The initial goal was to design the samples with the fluxon resonant frequency at about 10 GHz. In order to avoid samples with too high characteristic fluxon oscillation frequencies and being unable to adequately measure them, the length of AJJs in the first batch of samples was set to be $L = 1.3$ μm for the $j_c = 30$ A/cm^2 process and therefore the maximum fluxon oscillation frequency should have been at about $\nu \sim 8$ GHz. The reason for this was that we had amplifiers for the lower frequency band but not for the higher one.

The design of other pieces of layouts (such as current injectors, bias electrodes, microwave antennas) were mainly defined by the limitations of the fabrication process. As described in Refs. [Ust02, GSK04], the smaller the distance d between the current injectors, the larger injection current is needed to create a fluxon. The minimum distance between two separate electrodes in the M2 layer was set by design rules to be at $\delta_{M2} = 2.5$ μm due to the photolithography resolution limit. This minimal distance was used as the spacing between the current injectors assigned to create fluxon in the AJJ. Same applies to the microwave antennas for picking up radiation from the oscillating fluxon. Most antennas were designed using capacitive coupling to the Josephson transmission line. To increase this coupling, one needs to increase the capacitance or to decrease the distance between the antenna and the Josephson transmission line (a galvanic coupling was initially avoided because of risk of parasitic ground loops and an interference with the bias current distribution in the superconducting leads). This distance was again set at the minimum achievable by the current technology $\delta_{M1} = 2.5$ μm to obtain the best coupling possible. Retrospectively, that was crucial for the samples with the low critical current $j_c \sim 30$ A/cm^2. However, for the samples with the high critical current $j_c \sim 1$ kA/cm^2 it was not important at all as the radiation power of the fluxon was relatively large and even with weakly coupled antennas there was no problem to detect the fluxon radiation.

Later samples were designed and fabricated in the process with the high critical current density $j_c \sim 1$ kA/cm^2 because of a better stability of the fluxon resonance step for this j_c at low temperatures $T \sim 100$ mK and the higher microwave power emitted by the fluxon. For this j_c, a shift towards smaller AJJ diameters and, therefore, also higher fluxon

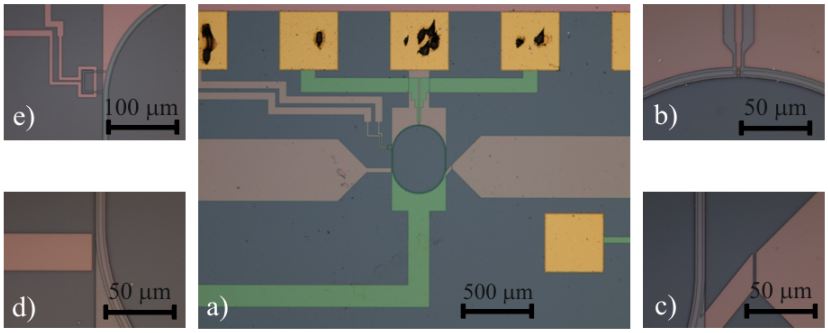

Figure 3.4: Photo of the first test sample fabricated in the process with $j_c = 30$ A/cm^2. **a)** Overview of the whole structure with the bonding pads (the black spots on the latter is the remnants of bonding wires). **b)** The current injectors for creating the fluxon. **c)**,**d)** The capacitively coupled microwave antennas. **e)** The coupling loop and the control line for a future qubit.

frequencies was made. This was done in order to make the structures a bit smaller and, thus, more compact on-chip. Also, the availability of a broadband $6 - 20$ GHz low-noise cryogenic amplifiers from the Low Noise Factory (Sweden) solved most of problems with the bandwidth limitation imposed by the older types of cryo-amplifiers. Thus, for $j_c \sim 1$ kA/cm^2, for the chosen radius of the AJJ $R_1 = 140$ μm the maximum resonance frequency should be at about $\nu \sim 12.5$ GHz. All the other parameters stayed the same.

Physical layouts and its functionality

The first designed and fabricated samples were implemented in the $j_c \sim 30$ A/cm^2 process. The optical photo of it is given in Fig. 3.4 with additional zooms into its separate important areas - the area of current injectors, microwave antennas and a qubit coupling loop.

Later samples contained various minor improvements (see Fig. 3.5) as: microwave antennas with better coupling and different geometry (bi-coplanar instead of microstrip), additional precautions in the form of patterned arrays of square holes in the bias leads in order to decrease

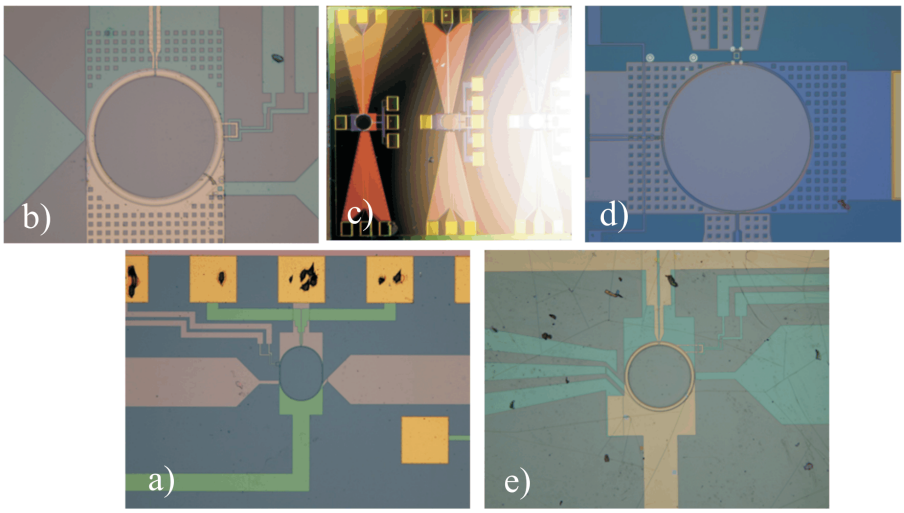

Figure 3.5: Optical photograph of various samples containing annular Josephson junctions with microwave antennas of different types (microstrip - **a)**, **b)**; bi-coplanar - **c)**, **d)**, **e)**), current injectors, qubit coupling loops and other features as rectangular holes in bias leads for Abrikosov vortices trapping(**b)** and **d)**).

magnetic noise in the AJJs due to a random movement of Abrikosov vortices, qubit coupling loops with different coupling strengths etc.

Both types of antennas demonstrated approximately the same measured microwave power of the fluxon signal. The notable advantage of the bi-coplanar antennas was the absence of many parasitic resonances, which are commonly present for the case of microstrip antennas. This happens due to a much smaller "crosstalk" of the microwave signal for the bi-coplanar antennas. Patterned holes for Abrikosov vortices trapping allowed to slightly decrease low-frequency fluctuations in the fluxon spectrum (basically, the long term stability of fluxon oscillation frequency was improved). Unfortunately, a try to organize inductive biasing of the current injectors through an additional loop (one can roughly see it in Fig. 3.5,**c)**) was not successful, presumably, because of a large "crosstalk" between the biasing magnetic field and the AJJ itself. The influence of the qubit coupling loops with different strength will be discussed in the next Chapter.

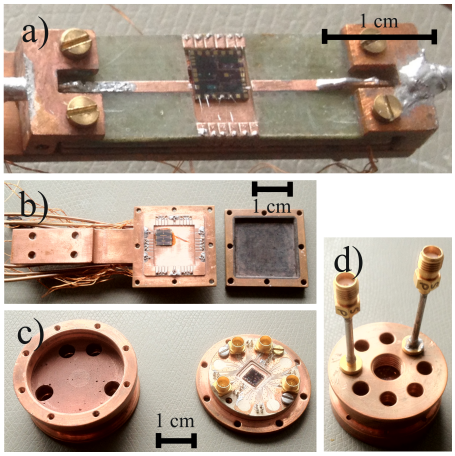

Figure 3.6: Different types of the sample holders. **a)**The mostly used type of sample holders compatible with microstrip microwave antennas. **b)** Old type of a sample holder compatible with bi-coplanar microwave lines. **c)** "New" generation of sample holders for bi-coplanar microwave lines. The interior view. **d)** Same holder as presented in c), the exterior view of the closed sample holder with the attached rigid microwave cables.

3.1.2 Sample holder

The next step for preparing the experiment was to attach the sample to external wires (low-frequency dc lines and high-frequency microwave lines). This was done with the use of so-called sample holders. Different types of sample holders were used in experiments depending on the sample under test (see. Fig. 3.6). As most of the samples employed the microstrip microwave lines, the sample holder of the type presented in Fig. 3.6.a) has been typically used. However, as microstrip lines usually have more problems with crosstalk [Sim49] and noise than bi-coplanar waveguides, some of the samples were redesigned to utilize the latter and therefore required another type of sample holders shown in Fig. 3.6.b),c). These holders were also better in terms of electromagnetic shielding as they provide additional metallic encasing around the sample. Importantly, these holders were also covered from inside by epoxy mixed with copper powder in order to reduce the reflection coefficient for electromagnetic waves and damp parasitic volume resonances

inside the sample holder. The absence of volume resonances inside of the sample holders is especially important for the qubit experiments as the former tend to couple directly to the qubit, decrease its coherence times and broaden a characteristic spectroscopy line.

Bonding a chip

The actual connection of a chip to sample holders were done with the IPT HB06 ultrasonic wire bonding machine. An aluminum wire with a diameter of $d = 25$ μm were ultrasonically welded to the chip to provide a good galvanic contact between the bonding pads of the sample and the sample holder. These wires can be seen in Fig. 3.6.a) as thin metallic threads between the sample and the sample holder. For microwave lines, where a characteristic impedance matching is crucial, aluminum ribbon is often used or many thin wires in parallel to reduce the total inductance of the bonds and provide minimum reflections in GHz range.

Magnetic shielding

To improve the quality of the experiments it is important to protect the sample from all kinds of noise. Magnetic fluctuations present the first obstacle for the current experiments as the fluxon is a magnetic particle by itself and, thus, is easily disturbed by the tiniest magnetic fields (which also has a benefit of being a good detector for anything magnetic sitting around, for example - a superconducting flux qubit). The magnetic shielding is designed to cancel out the stray magnetic fields (Earth's self-field, fields from working pumps all around the laboratory, fields of weakly magnetic microwave connectors etc.). The shielding was implemented as shown in Fig. 3.7. Usually, two shields have been employed: a smaller superconducting shield made of lead and a bigger μ-metal shield made of cryoperm.

3.1.3 Cryogenic setup

After bonding the chip to the chosen sample holder, closing it and protecting by various magnetic shields, the next task was to place it into a cryostat and then cool it down. There are at least several types of

Figure 3.7: a) Sample glued and bonded to a sample holder. Set of dc twisted pairs and a couple of microwave lines are exploited. b) Sample holder covered by a superconducting led shield. c) Sample holder with the second μ-metal shield attached, ready to be inserted into a cryostat.

cryostats which can be used for testing niobium samples with the temperature of superconducting transition around $T_c \sim 9$ K. The simplest one is the so-called dipstick which is a simple metallic tube that is inserted into a dewar with liquid helium at $T = 4.2$ K. It allows one to quickly test the basic properties of the chips and with minimal efforts required for the preparation. It is the most convenient and fast measurement test which was available for niobium Josephson junctions. The general scheme of fluxon radiation detection type of experiments is shown in Fig. 3.8. However, for more interesting measurements of fluxon dynamics at low temperatures and especially for qubit measurements, the temperature should be at least less than the critical temperature of the aluminum forming the qubit $T < 1.2$ K. To observe the actual quantum dynamics of the qubit and its interaction with the fluxon, the temperature should be lowered even further to stay below the energy splitting between ground and first excited states of the qubit

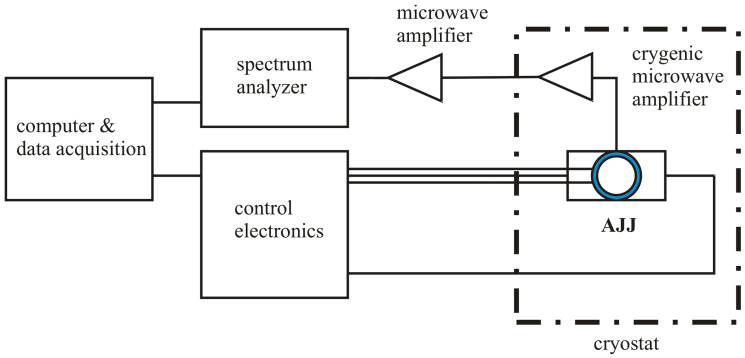

Figure 3.8: The general scheme of all measurements of fluxon radiation from the AJJ.

$T \ll \Delta E$ which, usually, corresponds to the temperatures of about $T \sim 30\text{mK} \ll 300$ mK.

He-3 cryostat

For testing of superconducting aluminum samples one needs to achieve a temperature below the superconducting transition temperature of aluminum $T < T_{Al} = 1.2$ K. A so-called He-3 cryostat offers an appropriate possibility to do so. Its working principle is based on the evaporation cooling of liquid He-3 [Whi87]. It is possible, in principle, to use He-4 for the same type of cooling method but its vapor pressure rapidly drops below 2 K point and the cooling process becomes inefficient, limiting the minimum reachable temperature with this method to about 1.5 K. As He-3 is the lighter isotope, its vapor pressure is two orders of magnitude greater than that of He-4 below 1 K. A well isolated bath of liquid He-3 may be boiled under the pressure of about $P \sim 10^{-3}$ mbar which corresponds to the temperatures of about 300 mK. This allows to cover the temperature range $1 - 0.3$ K with pumping on liquid He-3.

The general scheme of experiments stayed the same as for the dipstick measurement (see Fig. 3.8).

Dilution refrigerator

To get access to even lower temperature it is required to use more sophisticated techniques than simple evaporation cooling or its combinations. There are many ways for reducing the temperature to 30 mK though not all of them are reasonable for solid-state experiments. The most popular one is the adiabatic dilution of He-3 in liquid He-4. This technique was proposed by London, Clarke and Mendoza in 1962. It is based on the big difference of entropies between liquid He-3 and He-4, so it is possible to reduce the ambient temperature by adiabatic dilution of He-3 in He-4 when the former expands and thus cools down the whole mixture [Whi87]. Cryostats working on this principle are commercially available and have a base temperature of about 15 mK. We have used dilution refrigerator produced by Oxford Instruments with a cooling power of 100 μW at a temperature of 100 mK. While the general scheme for measurements stay the same as it was shown in Fig. 3.8, the inner wiring inside the cryostat becomes extremely important. The overview of the experimental wiring in the Oxford dilution refrigerator is given in Fig. 3.9.

The wiring consisted of two microwave lines (in and out of the dilution refrigerator) and a set of low-frequency twisted pairs (see Fig. 3.10). The radiation from the AJJ was picked up by the capacitively coupled microwave antenna and fed through a low-loss superconducting Nb cable to a broadband cryogenic LNF6-20 amplifier thermally anchored to the $T = 4.2$ K stage with a gain $G_1 = 31$ dB and an equivalent noise temperature $T_1 \simeq 9$ K. A cryogenic circulator Pamtech PTC1351K7 in the range $8-18$ GHz with an isolation of -20 dB has been used in order to protect the sample from the backaction of the cryogenic amplifier at the 4.2 K stage. The cryogenic amplifier was usually followed by Mini-Circuit room temperature amplifier ZVA-183-S+ with a gain $G_2 = 26$ dB and a noise temperature $T_2 = 600$ K. The total noise temperature can be estimated using Friis formula [Fri44]:

$$T_{noise} = T_1 + T_2/G_1 \simeq 9.6 \text{ K}. \tag{3.5}$$

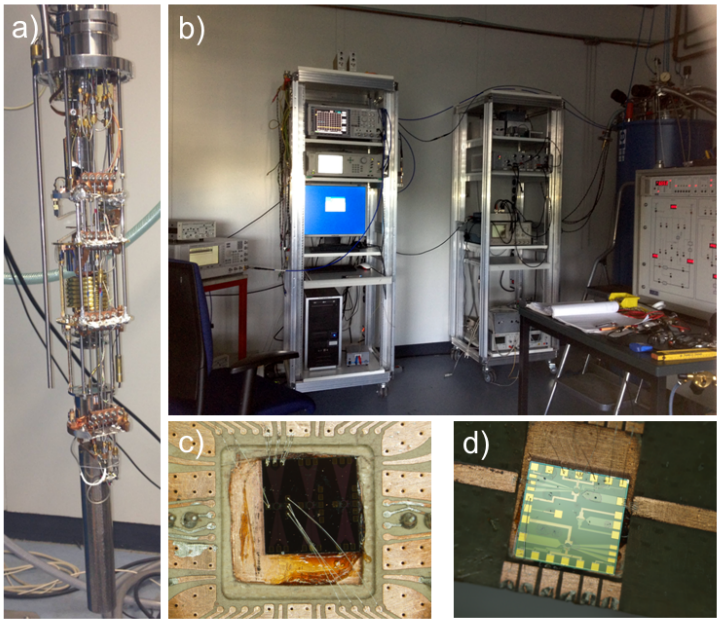

Figure 3.9: Photo of the experimental setup: **a)** Insert of the dilution refrigerator with the attached sample holder (covered by magnetic shields) in the lowest part. **b)** Racks with room temperature high-frequency (left one) and dc control electronics (right one) connected to the dilution refrigerator. **c)**, **d)** Bonded samples (size 5x5 mm) in different sample holders used in experiments.

As it can be seen, T_{noise} is dominated by the noise temperature of the first amplifier in the chain what makes it crucial to have a good low-noise cryogenic amplifier.

Filtering

To accurately measure current-voltage characteristics of the samples and to detect clear resonance radiation spectra from the fluxon oscillations in the AJJ one needs to filter both low frequency and microwave lines. For dc lines low-pass RC and LC filters have been used with additional specific copper powder filters. The latter are essentially well-

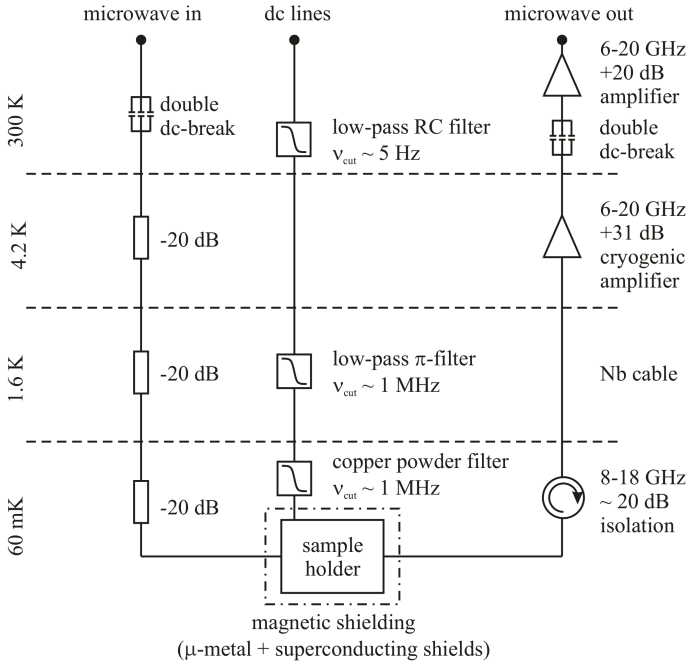

Figure 3.10: Experimental wiring inside the dilution refrigerator. The temperature stages are shown on the left hand side.

known LC π-filters with the one addition: the inductance in this filter is implemented using a long twisted wire immersed in epoxy with copper powder [LU08]. This allows one to effectively reduce the amplitude of electromagnetic waves with a frequency higher than 100 MHz (where the actual resonant properties of the LC filter does not bring an attenuation).

In some measurements, the current dividing technique was used to reduce thermal Johnson Ű Nyquist noise below the room temperature level. At the same time, it is also useful for filtering out technical noise of the current source. This is implemented by dividing the current I by the fixed factor $n = T_1/T_2$ through a cold resistor at temperature

$T_2 < T_1$ and feeding the rest current I/n to the sample under test (basically, introducing a standard microwave attenuator but to a low-frequency line). This trick allows one to bring the level of thermal fluctuations from T_1 to T_2. The described simple approach is valid only in the case when the load has the same resistance (impedance) as the current source. The latter is usually true for microwave devices and high-frequency lines. In case of low frequencies and dc-lines, ideally, one should also take into account a difference in resistances at different temperature levels to calculate precisely RMS current fluctuations $I_n = \sqrt{4k_BT/R}$ due to Johnson - Nyquist noise, but the general approach of the current dividing still remains the same.

Unfortunately, the current dividing technique was not very useful for our experiments as it imposed heavy technical constraints on the experimental setup - as the bias currents we routinely needed were rather high, about 10 mA. To reduce thermal noise in the bias current from ambient room temperature $T = 300$ K to the base temperature of the dilution refrigerator $T_{base} = 30$ mK, one would need to apply an initial current of 100 A which was not possible due to extreme overheating of the whole cryogenic setup. However, sometimes, particular improvement by current dividing was possible when smaller currents were used (for example, in the case of the samples with low critical current density $j_c \sim 30$ A/cm^2).

Microwave lines were filtered using bandpass filters when necessary. Typically, VHF-6010+ Mini-Circuits filters with a bandpass of $6.3-15.0$ GHz have been used. Double dc-breaks were always used for all microwave lines to galvanically decouple high-frequency room temperature electronics from the cryostat. Essentially, every of these double dc-breaks is a piece of a microwave cable with both an inner electrode and a ground encasing intersected by a small slit (capacitor), thus, breaking a galvanic link through the microwave lines. This was crucial for the described experiments as without this precaution, 50 Hz and 1 kHz harmonics, routinely generated by computers, spectrum analyzers, oscilloscopes and other devices, interfered with the very sensitive oscillations of the single fluxon. This effect, not strongly visible on simple voltage-current characteristics, was devastating for spectra measurements as it deforms the very spectral line of fluxon radiation.

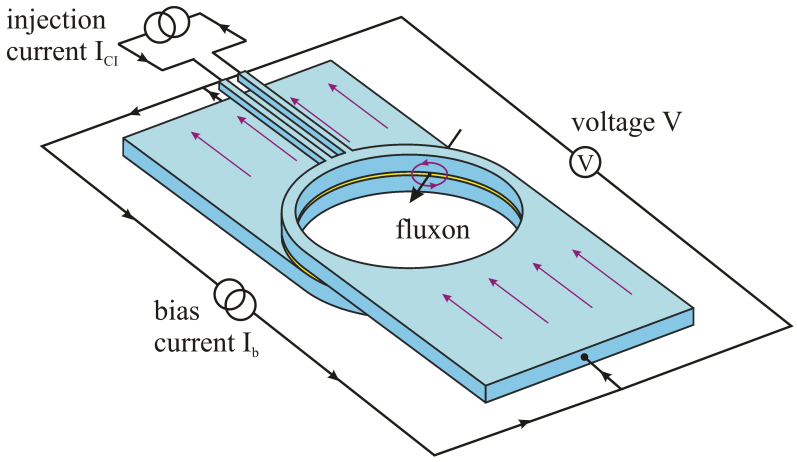

Figure 3.11: Principal schematic for measuring a current-voltage characteristic of a long annular Josephson junction with current injectors.

3.2 Experimental results

In this section results on the experiments with a single fluxon in an annular Josephson junction are presented. These results include dc measurements of resonant zero-field steps (ZFS) of fluxon oscillations inside the AJJ, direct detection of microwave radiation of the fluxon and investigation of a fine structure of ZFS, studies of a linewidth of fluxon radiation, a phase-locking of the single fluxon using an external microwave source and fluxon phase-noise measurements. The main aim of this work is to provide a necessary knowledge and techniques to implement fluxon readout for superconducting qubits.

3.2.1 Zero-field step measurements

Recording a current-voltage characteristic is the most basic approach to measure a Josephson junction. It allows to immediately estimate the critical current I_c, the normal state resistance R_N and some other derived parameters of the Josephson junction (critical current density,

damping, plasma frequency). As it was discussed in Chapter 2, the presence of a fluxon inside the annular Josephson junction also gives rise to a finite-voltage vertical step in the IV characteristic which allows to make swift testing of samples and proceed with more sophisticated techniques and studies.

DC measurements

First measurements of a zero-field step (or a fluxon resonant step) were performed for the sample shown in Fig. 3.4 with the low critical current density $j_c \sim 30$ A/cm^2. A schematic for the first experiments is shown in Fig. 3.11. It is a simple four-point setup for detecting a voltage across the AJJ while feeding a bias current through it. This allows to observe a supercurrent step at zero voltage (see black curve in Fig. 3.12) with the critical (switching) current of about $I_c \simeq 700$ μA and a normal state resistance $R_N \simeq 9$ Ω.

By applying a certain permanent electrical current through the current injectors in the top electrode of the AJJ, it is possible to create a fluxon inside the AJJ. This corresponds to a drastic decrease of the switching current as the junction switches to the finite-voltage state immediately as the fluxon starts moving. Fluxon movement is reflected on the current-voltage characteristic as a small vertical finite-voltage step as shown in Fig. 3.13.a) for a fixed injection current $I_{CI} = 2.18$ mA.

Microwave measurements

First experiments for detection of a microwave radiation from annular Josephson junctions were performed with the use of a cryogenic X-band microwave amplifier with a noise temperature of about $T_{noise} = 15$ K, a room temperature amplification cascade (when it was necessary) and a FSUP26 spectrum analyzer. The result of the first measurements is shown in Fig. 3.14. In the lower part of Fig. 3.14 there are measured spectra for different bias points, while the upper part shows the result of frequency conversion into voltage using the second Josephson relation $V = \nu_{fluxon} h/2e$. Figure 3.13,b) shows the comparison between the direct voltage measurements and the results of the microwave frequency detection approach. As it is seen, the precision of frequency

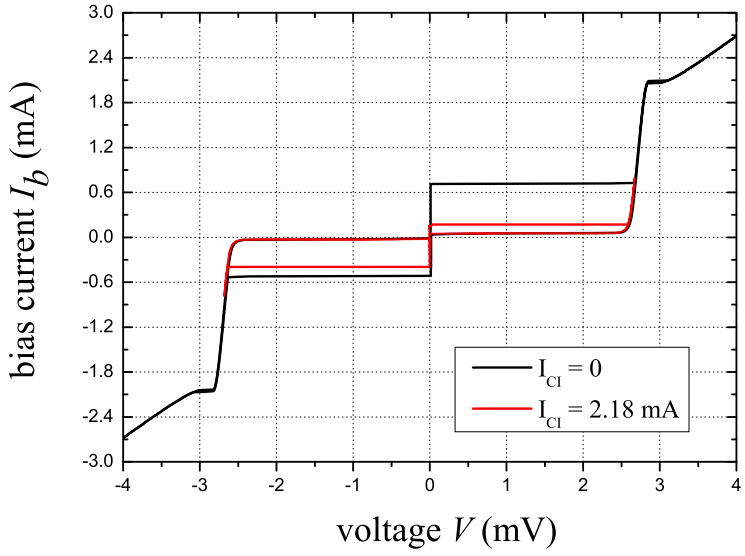

Figure 3.12: Basic current-voltage characteristics of a Josephson junction. The black line corresponds to the case with no injection current $I_{CI} = 0$, while the red one corresponds to the case with $I_{CI} = 2.18$ mA and an injected fluxon.

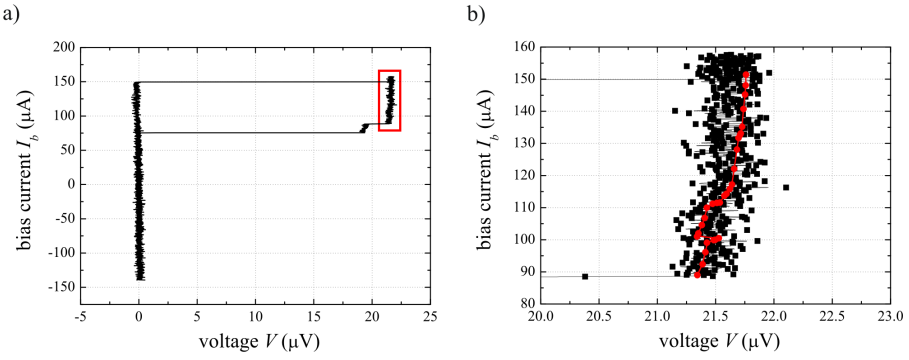

Figure 3.13: a) The experimental zero-field step measured by the four-point method. The area highlighted by the red rectangle is shown in greater detail in part b). **b)** Zoom of the zero-field step area. The red line shows the reconstructed ZFS measured in the frequency domain.

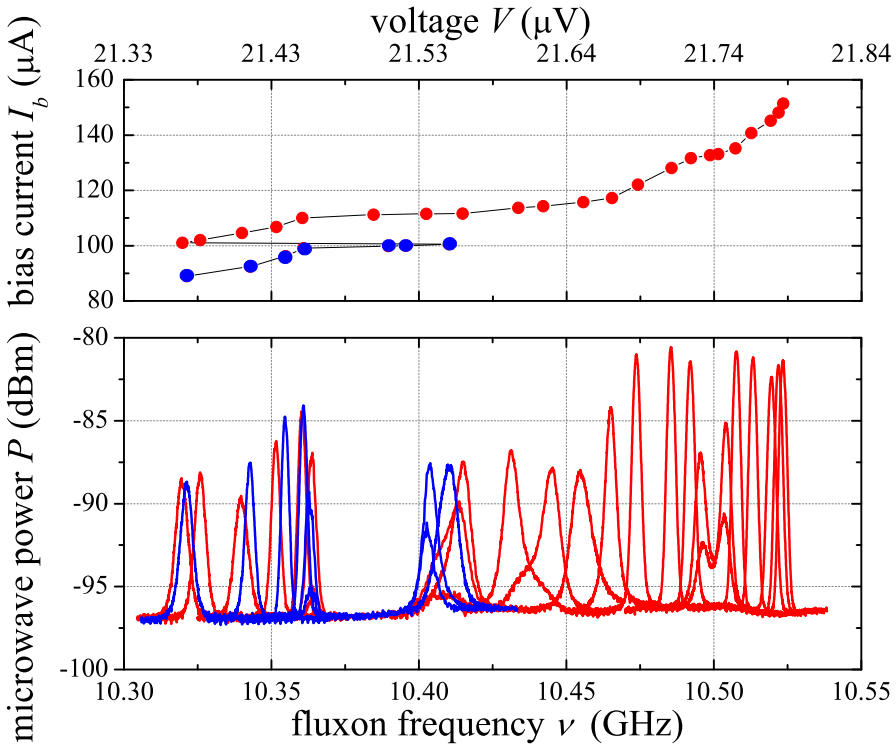

Figure 3.14: Experimental zero-field step and the spectral line-shapes for the corresponding bias values. Red and blue dots denote two "branches" of the zero-field step. Fluxon switches from the blue branch to the red one jumping backwards in frequency while increasing the bias current.

measurements (or, by other words, the level of noise) is much higher (lower) than that for a direct voltage measurement.

Figure 3.15 shows an another example of spectra of the single fluxon radiation from the AJJ along with a respective recalculated ZFS branch. Complicated fluxon dynamics in the AJJ becomes obvious from looking at these graphs (Figs. 3.14,3.15) with many strange peculiarities of the ZFS's fine structure. Some of them can be analyzed and understood but some remain mysterious. Generally, most of the presented peculiarities are possible to simulate using the full perturbed sine-Gordon 2.18 equation with addition assumptions about the biasing electrodes and other inhomogeneities in the AJJ. Such an approach is cumber-

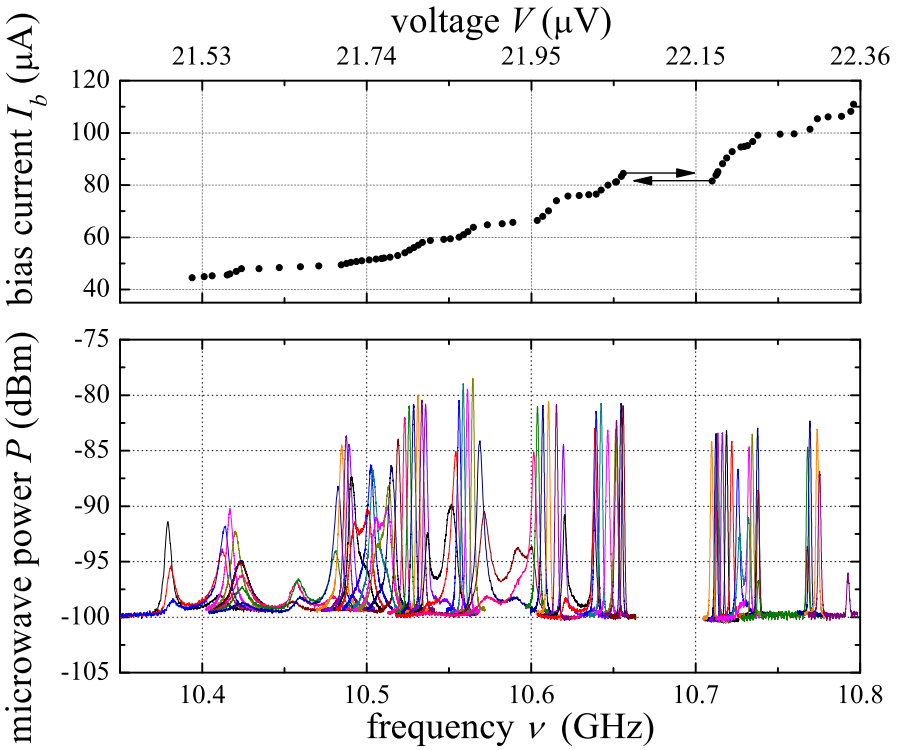

Figure 3.15: Experimental zero-field step and the spectral line-shapes for the corresponding bias values. Different line colors correspond to the different bias points. The lower part of the graph which contains spectra is indicated in dBm vs. GHz. The upper one with the recalculated IV characteristic is indicated in μA vs. μV. The voltage points were extracted as mean frequency values of corresponding peaks (multipeaks) times the Josephson constant.

some and usually does not give too much insight into the physics of obtained results but allows to make some quantitative estimations and even predictions. Similar studies of the fine structure of fluxon zero-field steps were performed in the past via dc voltage measurements [MBM93, BMU96, UMG99, PAU08].

3.2.2 Fine structure of zero-field steps

The previous section demonstrated that it is possible to reconstruct the zero-field step in a long Josephson junction by measuring the frequency of fluxon microwave radiation. The precision of this techniques is by many orders of magnitude better than that of the direct voltage measurements. The fundamental reason behind this fact is that it is always easier (in terms of noise and resolution) to measure a signal at high frequencies since low (or zero) frequencies are always strongly affected by $1/f$ noise.

As shown before, the presented ZFSs have been measured manually in the microwave detection regime which is, obviously, not a fast and a good way to proceed with such kind of measurements. From here and further, measurements are obtained using automatic scripts written in Python programming language. Automatization of microwave measurements allows to routinely measure zero-field steps with unsurpassed precision and reveal interesting fine structure of the former.

Lorentz profile

To study the spectral form of fluxon radiation, it is necessary to build up a theoretic model or, rather, to use an already built one. The single fluxon oscillating in the AJJ under the influence of the fixed bias current γ with the fixed frequency ω_0 can be treated as a linear (harmonic) oscillator if the intensity D of thermal fluctuations is small enough in comparison with $\partial^2\omega_0/\partial\gamma^2$. In other words, a nonlinearity of the fluxon should be small in comparison with the noise amplitude which perturbs the former. Here, we consider only a fundamental fluxon harmonic (neglecting all higher ones). The equation for the simple linear oscillator usually is given by the equation for a generalized coordinate $x(t)$:

$$\frac{d^2x}{dt^2} + \alpha\frac{dx}{dt} + \omega_0^2 x = f(t), \tag{3.6}$$

where $f(t)$ is an external force (in our case this is the homogeneous and constant bias current), and α is the damping parameter. The transfer function $K(\omega)$ of such the system has a well-known form:

$$|K(\omega)|^2 = \frac{A^2}{(\omega^2 - \omega_0^2)^2 + 4\alpha^2\omega^2}. \tag{3.7}$$

Generally, the response of the system $G_A(\omega)$ with transfer function $K(\omega)$ is given by [Ryt88]:

$$G_A(\omega) = |K(\omega)|^2 G_F(\omega), \tag{3.8}$$

where $G_F(\omega)$ is the spectral density of the input force. Introducing fluctuations in our system as the Langevin force, we write:

$$\frac{d^2x}{dt^2} + \alpha\frac{dx}{dt} + \omega_0^2 x = f(t) + \eta(t), \tag{3.9}$$

where $\eta(t)$ is the random process. In case of white noise, the spectral density of the random process is constant $G_F(\omega) = const$, which leads to the following spectral density of the output:

$$G_A(\omega) = \frac{A_0^2}{(\omega^2 - \omega_0^2)^2 + 4\alpha^2\omega^2}. \tag{3.10}$$

This shape is usually called a "Lorentzian" or a Lorentz profile (see Fig. 3.16). It is characteristic for cases of linear or quasi-linear oscillators exposed to white noise. Deviations from the Lorentz profile may be caused by a considerable non-linearity of the oscillator and thus by a deviation of the transfer function from the case (3.10). Another common reason for these deviations, is the change of the spectral density of the fluctuations which happens when the noise becomes quantum-limited or simply non-white (both change the spectral noise power density and therefore the output spectrum).

Advanced samples

For the further measurements, the type of samples under test were changed in favor of structures with greater critical density $j_c = 1$ kA/cm^2 and smaller diameter $2R_1 \simeq 280$ μm. In fact, the real critical current density varied from the designed valued and was found (by measuring additional test Josephson junctions) to be at about $j_c = 800$ A/cm^2. The maximum frequencies of fluxon oscillations in such samples were at about 15 GHz for ambient temperatures much less than the critical temperature of niobium $T_{ambient} \ll T_c$.

We can employ equation (3.10) for fitting the spectrum of fluxon radiation. As we see in Fig. 3.17, for a particular bias point the coincidence

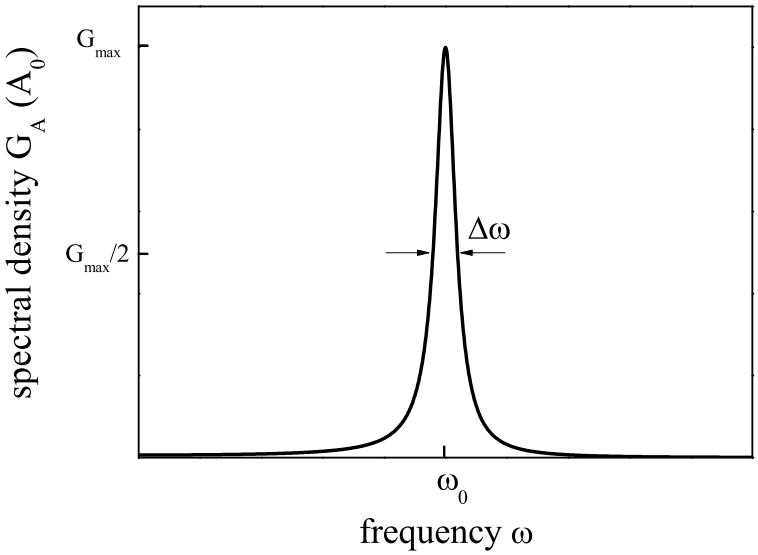

Figure 3.16: Output spectral density of a linear oscillator in the case of white noise influence. The linewidth of the spectral line is $\Delta\omega$.

between the fit and the experimental data is good. This means that fluctuations in our fluxon oscillator are dominated by the thermal noise and the fluxon oscillator by itself is in the quasi-linear regime. This is not true for all bias currents values along the ZFS as it can briefly seen in the previous Figs. 3.14, 3.15 where some spectra can have several maximums and generally can be non-Lorentzian. This can be explained by the emerging nonlinearity in some cases or by the situation when several fluxon attractors happen to be located close to each other separating a single spectrum into several Lorentzians. The typical reason for these attractors is a presence of unwanted inhomogeneities in the AJJ.

The full ZFS of one of the advanced samples is shown in Fig. 3.18 measured at temperature $T = 4.2$ K in the dilution refrigerator.

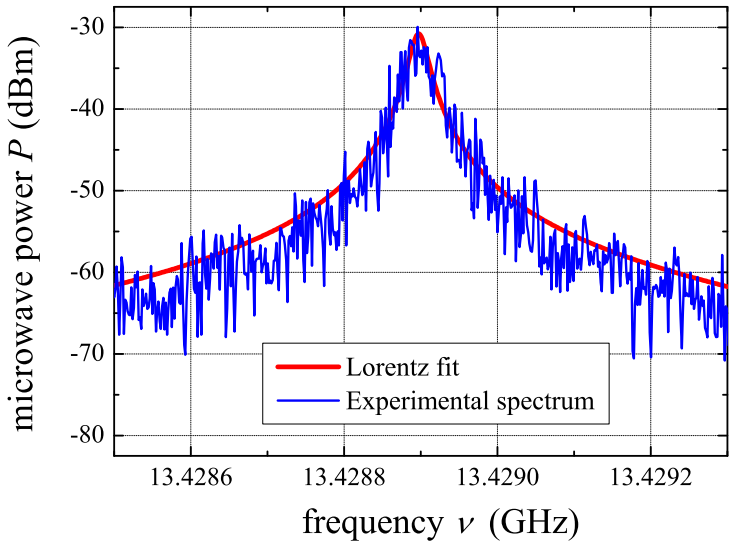

Figure 3.17: Snapshot of fluxon radiation spectrum fitted by the corresponding Lorentzian. The measurement has been performed at an ambient temperature $T = 4.2$ K, for a fixed bias current $I_b = 5.3$ mA and an injection current $I_{CI} = 3.973$ mA.

Fluxons: natural and artificial

One can create a single Josephson vortex inside such a ring-shaped Josephson junction by different means. The most natural one is to cool down the sample several times in a small magnetic field and eventually be lucky enough to trap a single fluxon (the so-called "try and pray" method) [MAK08]. Another approach, as it was already discussed in Chapter 2, is to send a certain dc current through the current injectors embedded into the top electrode (see Fig. 3.1). The latter way is much more reliable than the cooling in magnetic field method and allows to obtain reproducible results. However, it also has some disadvantages - the injection current creates an additional inhomogeneity in the junction's potential and additionally twists the current-voltage characteristics which complicates the analysis of the fluxon dynamics.

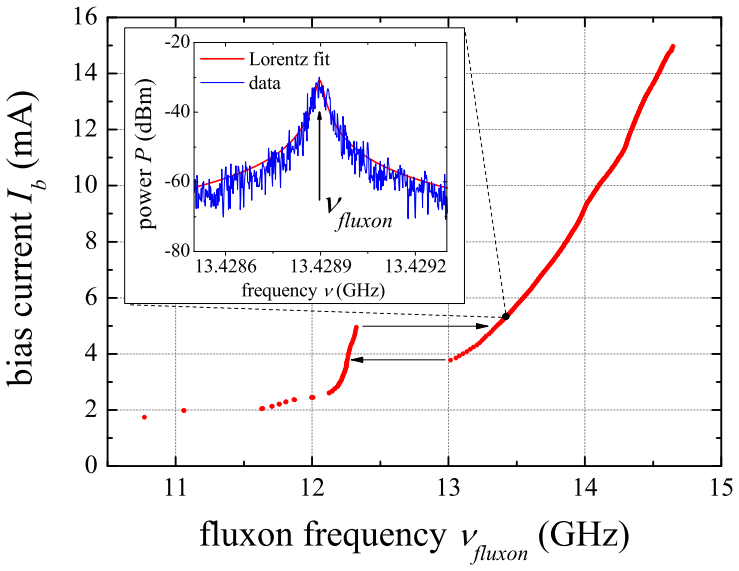

Figure 3.18: Zero-field step measured in the frequency domain for an ambient temperature $T = 4.2$ K and injection current $I_{CI} = 3.973$ mA. The inset shows the sample spectrum for the fixed bias current $I_b = 5.3$ mA with the respective Lorentz fit.

Both approaches have been exploited in order to compare zero-field steps (ZFS) of naturally born and artificially created fluxons.

Measurements: natural fluxon

We use an annular Josephson junction as a medium for a single fluxon (see Fig. 3.1). The sample was simply cooled in a small magnetic field in order to trap a fluxon. To achieve this, the process of cooling below T_c and then heating above the latter, was repeated $10 - 20$ times until a fluxon was caught.

For this particular experiment the He-3 cryostat was used. This cryostat allowed to perform rapid thermal recycling over the niobium critical temperature $T_c \simeq 9$ K because it has an internal vacuum chamber with a heater. For multiple thermal cycling experiments it is a much more

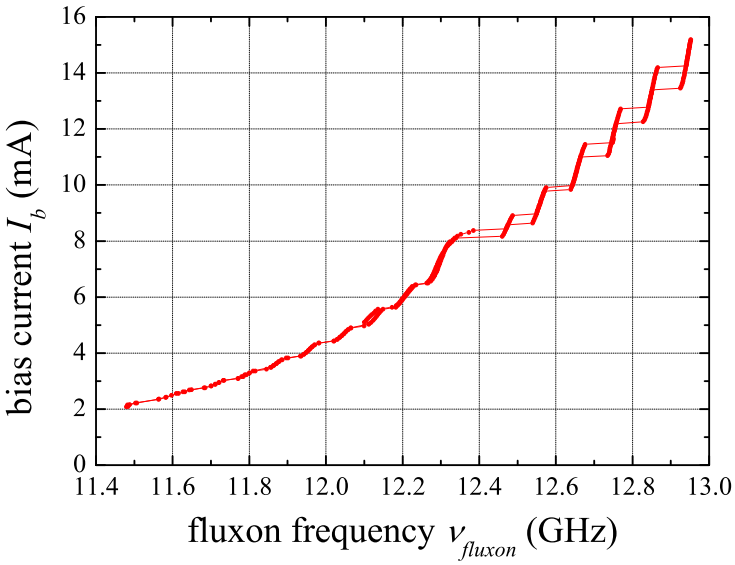

Figure 3.19: Experimental zero-field step of a single trapped fluxon in the AJJ.

convenient design than the dipstick. Also, it allows one to investigate stability issues of ZFSs down to the temperatures of $T \sim 300$ mK to prepare for the experiments in the dilution refrigerator. Of course, on the other hand-side, a certain price was paid because of the complexity handling of this type of cryostat plus severe spatial limitations on wiring, filtering etc. inside the cryostat itself.

Figure 3.19 shows a typical zero-field step of a single fluxon trapped during cooling below T_c in the AJJ. The notable fine structure in the form of many distinct steps in this figure can be explained by the resonant interaction of a moving fluxon with small-amplitude Josephson plasma oscillations generated by the fluxon motion [BMU96, MMF98]. Each vertical step in Fig.3.19 should correspond to a resonant condition $\omega_m = \gamma_m k_m$ (in case of large k_m), where ω_m is the angular frequency of the plasma waves, k_m is the their wave number, γ_m is the fluxon velocity at the resonance, and m is an integer resonance index. The physical mechanism of this resonant condition is similar to phase locking of an

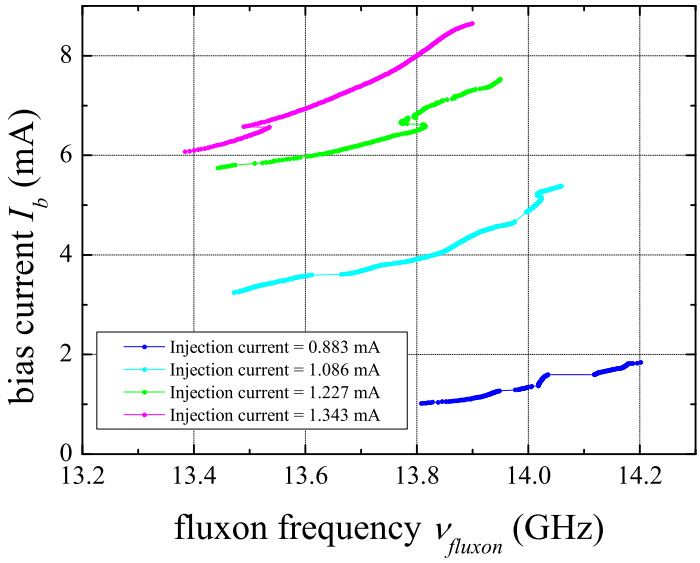

Figure 3.20: Experimental zero-field step of a single fluxon in the AJJ created by the current injection with the corresponding currents, noted in the insert.

oscillator (fluxon) by an external microwave source (plasma waves).

Measurements: artificial fluxon

Figure 3.20 shows the current-voltage characteristics of an "artificial" fluxon created by current injection. Four different curves for different values of the injection current are shown. An interesting observation is, that, in contrast with zero-field steps for the "naturally" trapped fluxon, these curves do not show such a developed fine structure of constant voltage steps as in Fig. 3.19. This fact can be linked with the passive presence of the second fluxon trapped between the current injectors or with an additional noise introduced by the current injectors, so that the inhomogeneity potential fluctuates and the fine structure steps are smeared.

Backbending

The notable "backbending" of the ZFS curve in the Fig.3.20 most likely happens because of two combined reasons. The first one is the nonlinear term $\sim A^2$ in the dispersion relation for the finite-amplitude plasma waves in Josephson junctions $\omega^2 = 1 + k^2 - A^2/8$, where k is the wave-vector, A is the amplitude of plasma waves [UMG99]. The second reason is the presence of the radiation threshold at the fluxon velocity $v_{thr} = \frac{1}{\sqrt{1+(2\pi n/l)^2}}$, below which fluxons do not emit plasma waves ($l = L/\lambda_J$ denotes the normalized circumference of the AJJ, n is the integer wave index). According to Mkrtchyan and Schmidt [MS79], the amplitude of the emitted plasma waves is largest near the radiation threshold. As can be seen from the dispersion relation, an appearance of finite-amplitude radiation at a certain bias point renders $A \neq 0$ and thus decreases the frequency ω. This explains the backbending nature taking into account that the fluxon oscillation frequency, in this case, is locked to the frequency of plasma waves.

Comparison

Figure 3.21 shows a comparison of data obtained for "natural" and "artificial" fluxons. Striking difference is the absence of the fine structure in the second case. This can be caused by the presence of the second static fluxon created by the injection current. Normally, it is situated in-between the injection electrodes and does not move and therefore does not give any direct contribution to the observed current-voltage characteristics. However, this fluxon may also interact with plasma waves and thus may disrupt (or change) the fine structure of ZFS. The intuitive explanation of this may be obtained from a simple model considering moving fluxon, plasma waves, and the static fluxon. While the moving fluxon can easily be locked by the plasma modes due to its dynamic freedom (*i.e.* it can change its velocity and place in space relatively easy), the static fluxon cannot do it. It is permanently trapped in the narrow area between the injectors and can undergo only very slight oscillations. At the same time plasma modes interact with both fluxons, but the static one cannot tune its oscillation frequency as easily as the dynamic fluxon to the plasma modes. Thus, the static fluxon

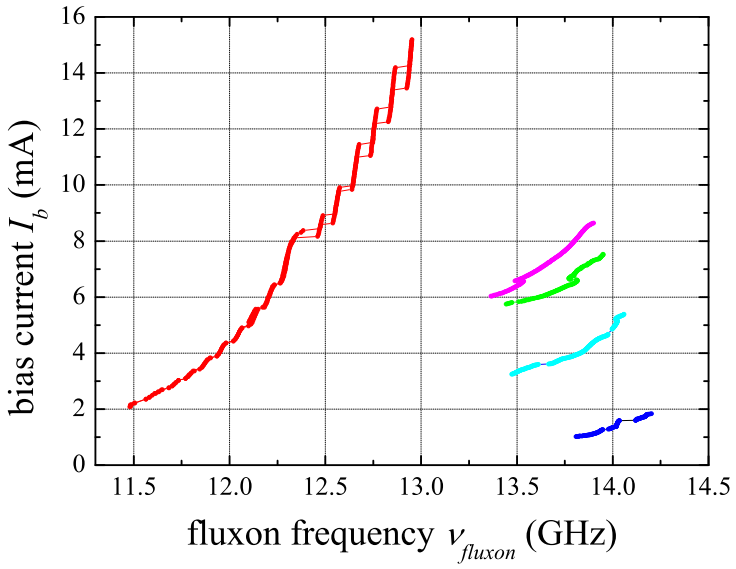

Figure 3.21: Comparison of zero-field steps of a single fluxon in the AJJ for the cases of "natural" and "artificial" fluxons.

may work as a damper for plasma waves in the AJJ effectively reducing their amplitude. However, the given explanation is rather speculative and requires a proper numerical simulation of sine-Gordon equation or an analytic consideration.

Another, more trivial explanation of the smeared fine structure of the zero-field step in the case of "artificial" fluxon is that the presence of the injection current itself provides additional fluctuations of the scattering potential for the fluxon and, thus, smoothen the fine structure.

Also, one might note that the frequency range of the "artificial" fluxon is shifted to higher frequencies in comparison with the "natural" one. This shift may be explained by the injection current itself, which creates a well in the potential profile on the spatial scale of $2\lambda_J$ for the moving fluxon making the oscillation time shorter and, respectively, the oscillation frequency larger.

3.2.3 Radiation linewidth

The linewidth of a spectral peak carries valuable information about fluctuational properties of an investigated system and its quality factor. It allows to extract useful information about the system parameters and noise sources.

Linewdith measurements

To measure the linewidth of fluxon radiation $\delta\nu_{fluxon}$ it is necessary to extract the shape of the spectral line near its maximum and estimate its full width at half-power as it is shown in Fig. 3.16. The simplest way to do so is to record a spectrum using a simple averaging to smooth out the noise and measure a linewidth $\delta\nu$ at the 3 dB down from the maximum value width of the final averaged curve. However, despite the simplicity of such an approach, it contains some critical flaws. The most important one is that if the averaging process is longer than the correlation time of long-term fluctuations τ caused by the technical noise, the resulting shape will be non-Lorentzian and therefore the estimated linewidth $\delta\nu_{fluxon}$ will be ill-defined. To overcome this problem it possible to use an approach developed by L. Bernstein [Ryt88] for measurements with noticeable low-frequency noise: to measure the natural linewidth of a spectral line one has to measure for a time shorter than τ and, thus, avoid distortions by low-frequency fluctuations. To measure the linewidth of fluxon radiation $\delta\nu_{fluxon}$ in the experiments the least squares method was used to fit every single spectral line of fluxon radiation with the Lorentzian curve (3.10) and extracted the 3 dB linewidth of the peaks from the fitting parameters. This has been done on-fly during the measurement process of ZFSs using an automatized Python script. Every experimental curve was measured within 20 ms time on the spectrum analyzer. It was the shortest time possible for our FSUP26.

The first consistent approach for a description of fluxon radiation linewidth accompanied by measurement data was given in the paper by Joergensen et al. [Joe82]. According to their approach, the fluxon linewidth for a fixed point on the zero-field step can be estimated by

the following simple expression:

$$\Delta\nu_{fluxon} = \frac{\pi k_B T_{ambient}}{\Phi_0^2} \frac{R_D^2}{R_S}, \tag{3.11}$$

where R_D is the differential resistance, and R_S is the static resistance. This result can be achieved by assuming that the noise in a long Josephson junction is described by the Nyquist formula [Nyq28, Ryt88] and then using the second Josephson relation to transform voltage fluctuations to the current noise.

Figure 3.22 presents experimental results on measurements of the spectral linewidth of fluxon radiation for the single trapped fluxon (see Fig. 3.19) and the appropriate comparison with theory. Red points denote the experimental data, while the blue ones indicate the predictions using equation (3.11). Differential and static resistances have been calculated using experimental data presented in Fig. 3.19 and assuming $T_{ambient} \simeq 310$ mK. As can be seen, the quantitative discrepancy between the theory curve and the experimental data is huge, though, qualitatively, the shapes of both curves coincide well. This, probably, means that the effective noise temperature in the experiment is much higher than the 310 mK indicated by the He-3 cryostat sensor. However, to fit theory to experiment, the effective temperature should be about 1000 times higher which is very strange as the deviation of $2-3$ times could be possible due to the difference between phonon and electron temperatures but 1000 does not make any sense (superconductivity would disappear at temperatures "only" 100 times higher than the current $T_{ambient}$).

This strange phenomena suggests two things: either we had in our measurements extremely strong external noise which widens the $\Delta\nu_{fluxon}$ or the model proposed in [Joe82] is simply not correct for the single fluxon oscillations in the AJJ.

Filtering and noise issues

To check the aforementioned ideas, some improvements in the experimental setup have been made, in order to bring the noise level down as low as possible. The main change was that the whole room temperature dc electronics was put onto a battery power supply and completely

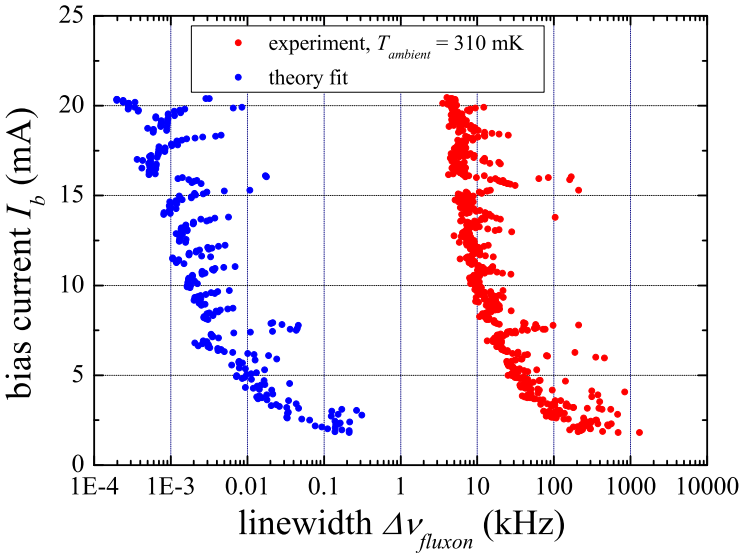

Figure 3.22: Measurements of fluxon ("natural") radiation spectral linewidth and its comparison with theoretical predictions.

galvanically decoupled it from the high frequency electronics in order to get rid of unwanted 50 Hz (common network frequency) and 1 kHz harmonics (typically employed in power transformers in all computers etc.). To check the effect of these changes the measurements of a fluctuation spectrum of fluxon resonant peak by itself have been used. The procedure was the following: the Lorentzian peak from fluxon radiation as it is shown in Fig. 3.17 was routinely recorded. Then, the spectrum analyzer has been set in the time domain regime tracking the single fixed frequency ν_{fluxon} (which was determined and fixed using the previous measurement). Finally, a lengthy trace of power dependence on the fixed fluxon frequency versus time $P_{fluxon}(t)$ for fixed time $T = 100$ s with the typical number of resolution points $N = 30001$ was recorded. The Fourier transformation of the recorded set of data $P_{fluxon}(t)$ provides access into a spectrum of fluctuations at the fluxon frequency itself. At the very beginning, such a spectrum contained many par-

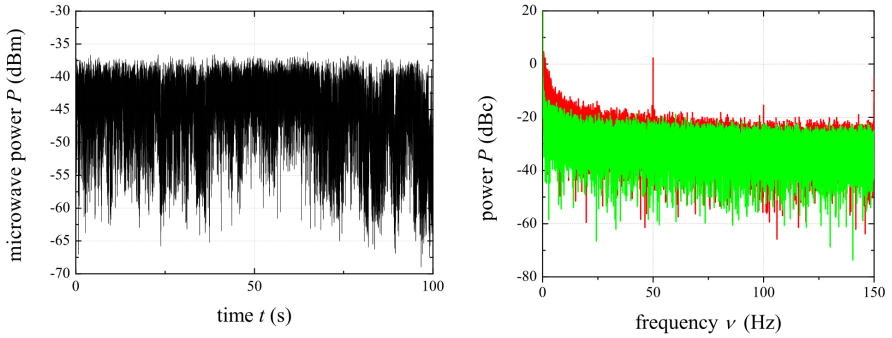

Figure 3.23: The black line shows a typical example of a time trace of power fluctuations at the fixed frequency $\nu = 14.31$ GHz corresponding to the center frequency of fluxon oscillations. The red and the green lines are showing the result of the Fourier transform of a such time trace. The red line is given for an experimental setup with galvanically coupled dc and microwave grounds. The green line illustrates the situation when these two are isolated from each other and additional precautions are made.

asitic peaks (see Fig. 3.23) indicating that there were many different noise sources affecting the fluxon. With every change of the experimental setup a check of the spectrum of fluxon fluctuations has been made in order to find out and to remove all possible parasitic frequencies. At the end, it was possible to achieve a rather clean picture of fluxon fluctuations, removing all low-frequency parasitic peaks as well as lowering general $1/f$ noise (see Fig. 3.23, the comparison of the red and the green lines).

Measurement: dilution refrigerator

After fixing the problem with parasitic signal coupling to the fluxon in the AJJ, the linewidth measurements of fluxon radiation were repeated. This time, the dilution refrigerator setup (see Fig. 3.10) was used for the measurements as it allowed to test a wider range of temperatures and also has better filtering (because it has much more space for filters etc.). The results of typical measurements of ZFSs in the dilution refrigerator is shown in Fig. 3.24 for four typical temperatures.

Linewidth dependencies correspondent to Fig. 3.24 are shown in sub-

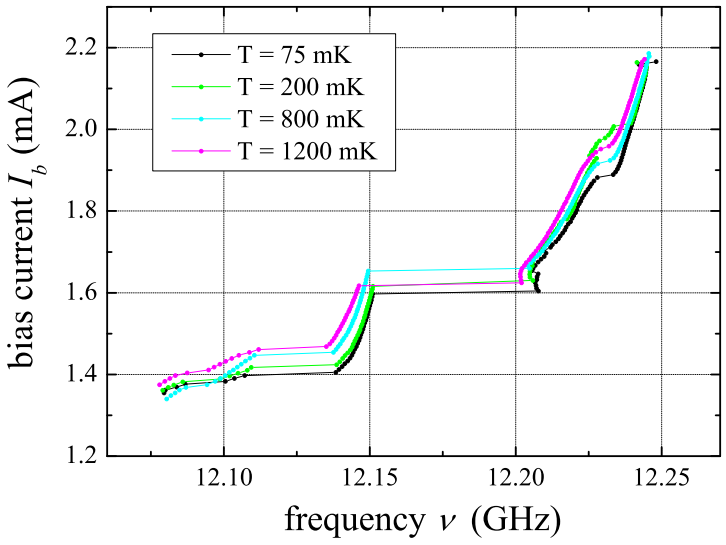

Figure 3.24: Measurements of zero-field steps ("artificial" fluxon is considered here) performed in the dilution refrigerator at different temperatures.

sequent Fig. 3.25. In this figure, a theoretical fit is shown for the temperature $T = 75$ mK using the differential R_D and the static R_S resistances extracted from the previous plot. Again, the qualitative coincidence between the theory and the experiment is good, however, the quantitative one is terrible as the theory values stand aside the measured ones by approximately 3 orders of magnitude. Here we can be sure that this deviation is not caused by any parasitic noise source coupled to the AJJ (see Fig. 3.23). This means that the deviation can be caused by the theory not being appropriate for the studied experimental conditions. One obvious reasons for this discrepancy can be the fact that Joergensen et al. theory does not take in account the surface losses. However, at very low temperatures $T \ll 4$ K, the usual damping term α is known to drop considerably while the major damping the fluxon experiences due to the surface losses. At any rate, we have to state that the problem of the discrepancy between experimental and theoretically predicted linewidth

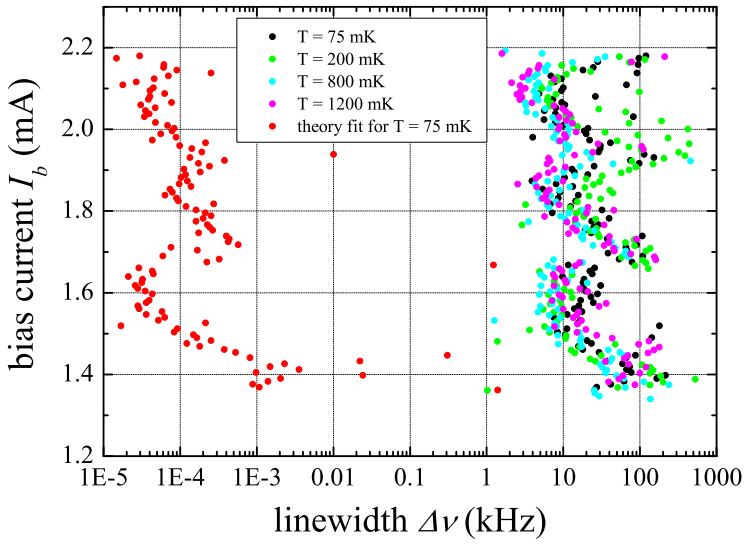

Figure 3.25: Measurements of linewidth of the fluxon radiation in the AJJ in the dilution refrigerator at different temperatures.

remains unsolved and puzzling, and requires further studies.

3.2.4 Phase-locking of a fluxon oscillator

Phase-locking is a very well known technique in radioelectronics. Its main idea lies in the fact that it is possible to stabilize a bad oscillator by connecting it in a special way to a better one. Thus, one suppresses phase fluctuations of the bad oscillator by continuously comparing its signal with the good oscillator (whose phase fluctuations should be much smaller) and generating a so-called *feedback signal*, which is then fed back to the first oscillator and hereby cancel out phase noise. This technique is very powerful and is widely used in almost all modern rf-electronics. In the case of the fluxon oscillator, it can help to stabilize its oscillation frequency and can also be used in a special fashion to readout a superconducting qubit.

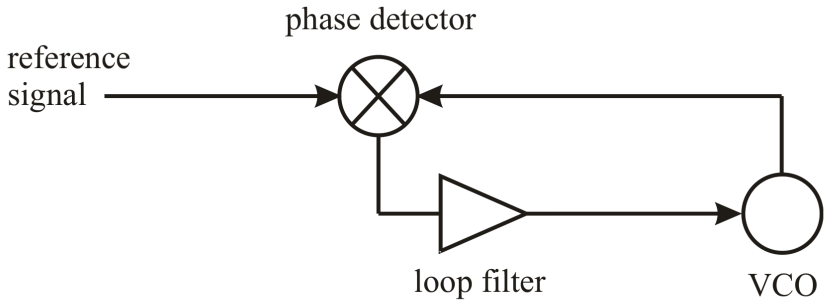

Figure 3.26: Basic phase-lock loop for a voltage-controlled oscillator (VCO).

General scheme and purposes

A phase-lock loop (PLL) usually contains two essential elements (see Fig. 3.26): a phase detector and a voltage-controlled oscillator. The phase detector compares the phase of a periodic reference signal with the phase of the VCO signal and produces a feedback signal proportional to the phase error between these two. Usually, an additional element is also present in most PLLs, which is a loop filter. It allows to filter unwanted frequencies in the feedback signal, amplify it or make another appropriate transformations. The simplest version of the loop filter is a passive low-pass filter or a PID amplifier. The filtered feedback signal is sent back to the VCO changing its frequency in a direction that reduces the phase error between the reference signal and the VCO. When the loop is locked, the control voltage sets the average frequency of the VCO exactly equal to the average frequency of the reference signal. The detailed description of underlying physics can be found in, for example, [Gar05].

Implementation

The experimental scheme for implementing a phase-lock of the Josephson vortex oscillations in the annular Josephson junction to an external

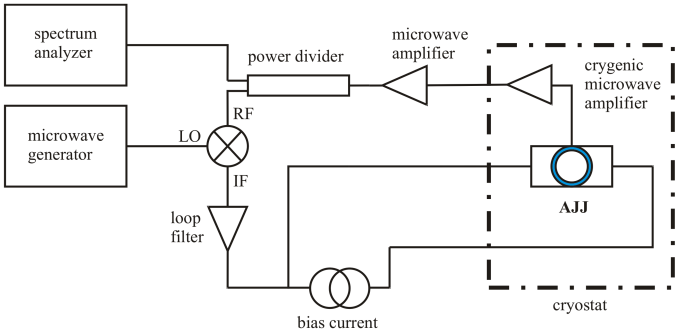

Figure 3.27: Implemented scheme of phase locking the fluxon oscillator. The fluxon radiation from the AJJ is amplified by the chain of amplifiers and fed to the RF port of the harmonic mixer. The reference signal from the external microwave generator is fed to the LO port of the mixer. The IF port provides the difference signal at the frequency $\nu_{IF} = \nu_{LO} - \nu_{RF}$. This feedback signal is filtered loop filter (which can be an active one if needed) and fed back to the bias current line in order to compensate for the fluxon deviations and phase lock it to the reference frequency. The loop filter also usually contains a phase shifter.

signal is shown in Fig. 3.27. A harmonic mixer was used as the phase detector. For first experiments, a simple low-pass filter with a cutoff frequency $\nu_c = 100$ kHz was used as the loop filter.

Surprisingly, the most primitive scheme with the low-pass filter and harmonic mixer already functioned well enough. It allowed us to implement the first phase-locking of the fluxon oscillator. We note that previously the phase-locking of fluxons has been realized only in much high frequency range of several hundreds GHz using a flux-flow oscillator (basically, in the case of a dense chain of moving fluxons) [KS00]. The resulting spectrum are shown in Fig. 3.28 as well as the comparison of the phase-locked signal with the autonomous fluxon spectrum.

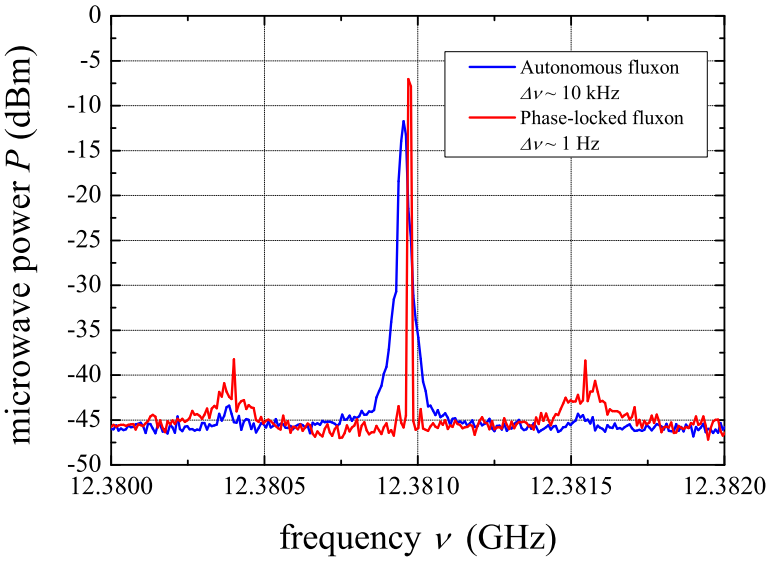

Figure 3.28: Phase-locked fluxon spectrum, indicated by the red line and its comparison with the autonomous fluxon spectrum given by the blue line.

A very characteristic for a phase-locked oscillator plato with two additional smaller peaks appeared (see the red line in Fig. 3.28). The frequency span between these two peaks generally equals to a bandwidth of the PLL and is roughly $\Delta_{PLL} = 1$ MHz here. Notably, the spectral linewidth $\Delta\nu \simeq 1$ Hz of the phase-locked signal is many orders of magnitude less than the linewidth of the autonomous signal $\Delta\nu \simeq 10$ kHz and, generally, is limited only by the linewidth (or phase fluctuations) of the reference signal (precision of the typical modern microwave source is about 1 mHz).

In Fig. 3.29 one can see spectral snapshots of locking of the free fluxon oscillations by the phase-lock loop as it happened on the screen of the spectrum analyzer. Four instances of spectra are shown in Fig. 3.29, each of them corresponding to the specific reference signal frequency approaching the fluxon frequency and marked by arrows. We can see that when the reference signal frequency is far away from the fluxon

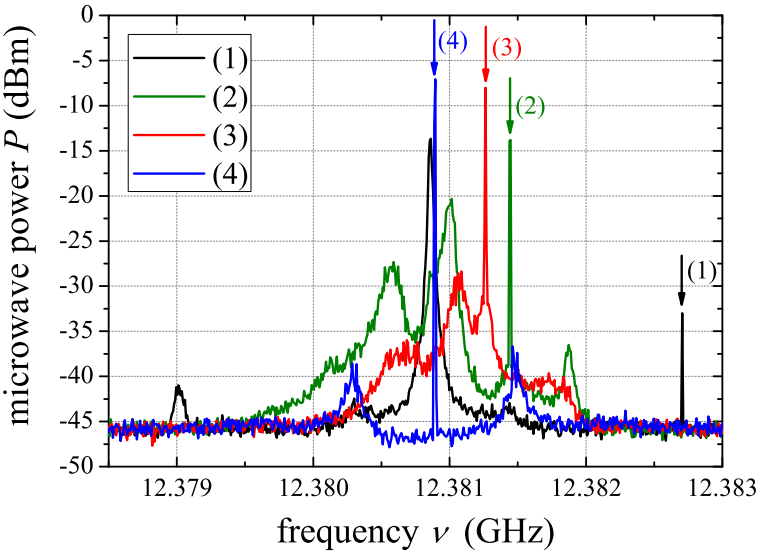

Figure 3.29: Curves (1)-(4) illustrate the phase locking process during approach of the reference frequency (its position is indicated by vertical arrows) to the fluxon frequency.

frequency nothing is happening except emergence of a small symmetric satellite peak (the black line). When the reference frequency approaches closely, at the very border of the PLL bandwidth, the partial synchronization of the fluxon oscillations occurs and the spectral line takes a weird shape given by the green line. The next step closer to the autonomous fluxon frequency increases the synchronization and, as a result, the power of the phase-locked signal grows (the red line). Finally, the blue line illustrates a situation when the reference signal and the autonomous fluxon frequencies are almost equal to each other. The power of the phase-locked signal is maximum here and at least 7 dB higher than the maximum power of the autonomous fluxon oscillations.

For the better performance, for a wider frequency range of the phase-locking, the passive loop filter was replaced by the low-noise preampli-

fier SR560 with an embedded tunable band-pass filter due to the need for an amplification of the feedback signal in a certain bandwidth. A phase shifter before the preamplifier is also very useful for phase-locking (sometimes, indispensable) due to the need to adjust the phase of the feedback signal.

Phase noise

A good way to characterize the quality of an oscillator is to measure its so-called phase noise. It is defined as the power at the offset frequency ν from the carrier frequency ν_0 (which is in our case equals to the fluxon frequency ν_{fluxon}) related to the maximum power of the oscillator. Therefore, the phase noise is measured in dBc which indicates how much power in dB related to the maximum power of the oscillator phase noise has at the certain offset frequency ν. Generally, a good oscillator is characterized by a low phase noise. Therefore, it is reasonable to compare the autonomous fluxon oscillator and the phase-locked one via the phase noise measurements.

To measure the noise one needs to measure microwave power at the offset frequency from the carrier. Fortunately, our spectrum analyzer has an embedded option and all required software to do this automatically which makes the whole measurement process comfortable. The results of experimental measurements of the phase noise for different types of the fluxon oscillator is presented in Fig. 3.30. As it can be seen, the phase noise for locked fluxon is lower than for its free counterpart for $10 - 20$ dB for the whole frequency range.

PLL applications

From the author's point of view, the phase-locking of the fluxon oscillator was by itself an intriguing part of the presented experiments. But as usual, men is interested in the practical applications of any kind of physics. The phase-locked fluxon oscillation in the AJJ, is no exception. One of the possible applications for such scheme was already proposed and developed in Ref. [KV05]. The idea is to use the phase-locked fluxon in the AJJ as a local clock-generator, allowing one to distribute an important clock signal within an RSFQ digital circuit. Our prac-

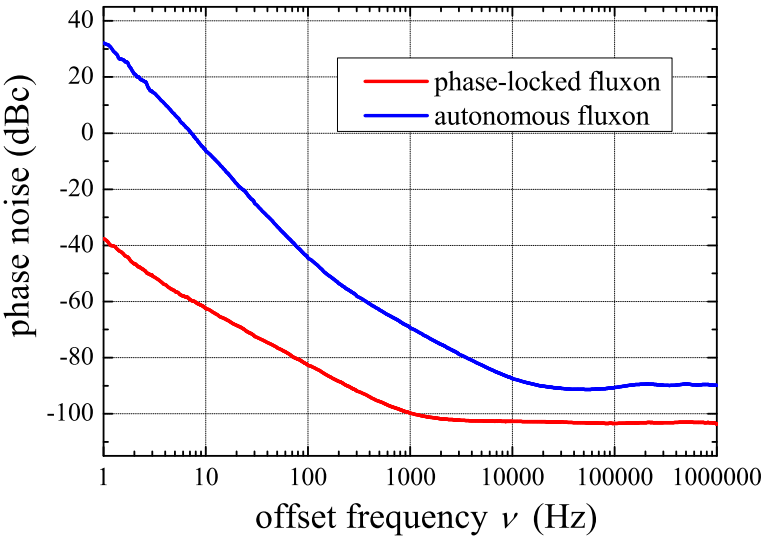

Figure 3.30: Phase noise measurements of the fluxon oscillator.

tical reason to investigate this matter experimentally was to make an improved fluxon readout of a superconducting qubit via implementing the phase-lock of the former. The idea was that by removing a part of the noise from fluxon oscillations (and putting it to the feedback channel), one makes an environment around the qubit linked to the fluxon in the AJJ less noisy and therefore improves the whole readout and coherence times of the qubit. In this scheme, the feedback signal of the PLL loop is designed to carry a useful information about the qubit state.

3.3 Conclusions

In this chapter, the designs and the practical implementations of different annular Josephson junctions for detecting microwave radiation of a single fluxon have been demonstrated. It was shown that it is possible to measure this radiation with the use of a cryogenic low-noise amplifier. The resolution of such measurements is found to be much higher than

the resolution of standard direct voltage measurements of Josephson junctions. This technique has been employed to resolve a fine structure of zero-field steps and measure a corresponding linewidth of fluxon radiation for different bias points. The fine structure of the zero-field step was studied for two different cases: a randomly trapped "natural" fluxon and an "artificial" fluxon created by current injection. We carried out a comparison between these two cases which has shown that the resonant interaction between the fluxon and plasma waves leading to a series of constant voltage (frequency) steps may be disrupted in the case of the "artificial" fluxon.

It was also observed that the linewidth of the fluxon radiation from the AJJ at low temperatures $T < 2$ K is not described well the by the existing theory. This very interesting, rather fundamental problem deserves further investigations. The successful experimental implementation of a phase-locking technique allowed to stabilize (lock) the fluxon oscillations in the AJJ and significantly reduce the phase noise of the latter.

4 Fluxon readout for flux qubits

Nowadays, a classical interface for qubits is an emerging milestone in the development of circuits with multiple solid state qubits. An efficient control and readout of several quantum bits requires a powerful classical computer in order to process the vast amount of real-time measurement data from a quantum counterpart. These days, researchers often use specific programmable electronic boards (so-called FPGA boards) in order to meet the requirements for high processing speed, flexibility and reasonable price. However, in the near future this approach will become inefficient due to the complexity demanded by communication between many qubits and room temperature readout electronics. The fluxon readout for superconducting qubits can potentially fill this gap via merging together superconducting digital logic in the form of RSFQ and the quantum counterpart.

The idea to use fluxons for detecting the state of flux qubits was initially proposed and analyzed in [ARS06]. It was theoretically shown that a ballistic fluxon, weakly coupled to a superconducting flux qubit, can be used to readout the quantum state of the flux qubit [ARS06, HFS07]. An advantage of the fluxon readout over the usual dispersive readout with the use of linear resonators is that the distribution of the electro-magnetic field in the conventional bi-coplanar resonator is such that it perturbs the qubit as long as there are photons inside the resonator. For the fluxon readout, the situation is different. A fluxon interacts (and perturbs) a qubit for a very short time due to its localized nature. This time depends on JTL parameters with typical time scales of about 1 ps. That, potentially, allows to further improve the screening of a quantum circuit from the outer world and hence improve its coherence times.

In the tested approach towards fluxon readout of superconducting

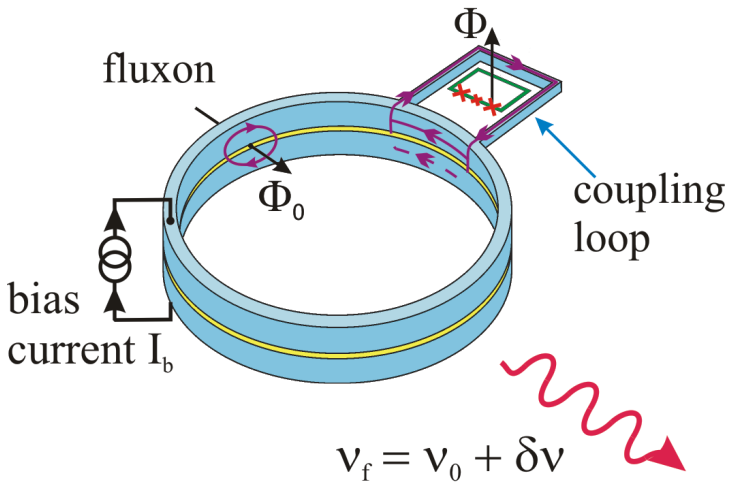

Figure 4.1: Annular Josephson junction with an injected fluxon coupled to a flux qubit homogenously biased by an external current source I_b. The bias electrodes are not shown for better clarity. The purple lines show the flow of the electrical currents forming the fluxon and the current dipole. A fluxon equilibrium oscillation frequency ν_0 is shifted by an amount $\delta\nu$ due to a fluxon scattering on a current dipole produced by a flux qubit. Microwave radiation from the fluxon is received by a microstrip antenna and later fed to a cryogenic amplifier (not shown).

qubits, a flux qubit is placed close to the annular Josephson junction and coupled magnetically to the latter via an additional superconducting coupling loop (see Fig. 4.1). Thus, the fluxon interacts with a current dipole formed by the electrodes of the loop coupled to the qubit. The frequency of fluxon radiation (or its equilibrium velocity) carries information about the state of the coupled qubit. Using the experimental techniques for detecting the fluxon radiation from the AJJ (demonstrated in the previous Chapter 3), one can resolve oscillations of a persistent current in the flux qubit loop as variations of the fluxon radiation frequency. This variations, however, are complicated by the specific interaction between the moving fluxon and the static current dipole. It is possible to analyze such a system via a perturbation theory of the sine-Gordon equation. Using the latter we demonstrate that the frequency shift of the fluxon oscillations depends only on the current

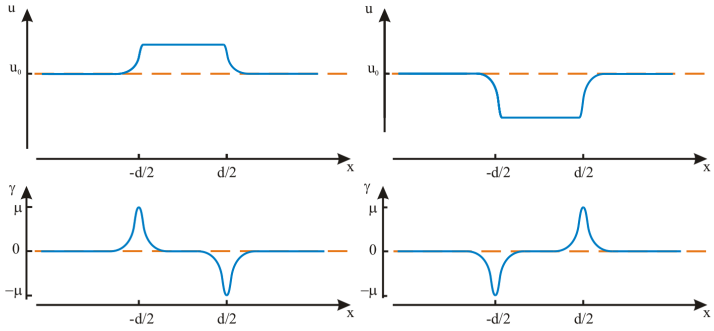

Figure 4.2: Illustration of the ballistic fluxon scattering on the current dipoles with different signs plotted as the dependencies of the fluxon velocity u and the bias current γ versus spatial coordinate x (the left part corresponds to the positive dipole, the right one - to the negative) in the absence of damping and homogeneous bias current. The sign of the dipole (or, simply, what comes first - the dip or the peak) determines the sign of the velocity change and thus the total change of the propagation time (frequency). Note that the deceleration process (negative dipole, the right part of the figure) is always stronger than acceleration one (positive dipole) in the ideal case due to the relativistic correction. This is true only in the aforementioned ideal case.

dipole strength and does not depend on its polarity. This holds for all meaningful fluxon velocities $u > 0.1 \cdot c_0$.

At last, using all the gathered knowledge about the fluxon readout scheme, we were able to resolve the flux qubit quantum transition between the ground and first excited states as the frequency shift of fluxon oscillations. This transition was excited by an additional continuous microwave signal from an external microwave generator at a fixed frequency. An energy spectrum of the superconducting flux qubit was measured using the fluxon readout technique.

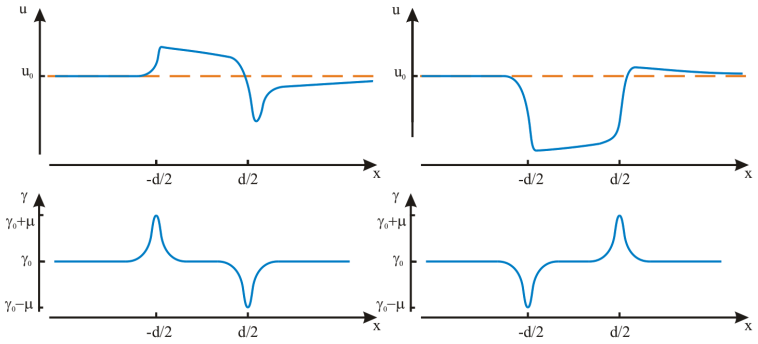

Figure 4.3: Illustration of the ballistic fluxon scattering on the current dipoles with different signs (the right part corresponds to the positive dipole, the left one - to the negative) in the presence of damping and homogeneous bias current γ_0. Now, the resulting change of a total propagation time is not obvious.

4.1 Scattering of a fluxon on a current dipole

To couple a flux qubit to the fluxon inside an annular Josephson junction, it is necessary to engineer an interaction between two orthogonal magnetic dipoles. To facilitate this interaction, we have added a superconducting coupling loop embracing a flux qubit, as shown in Fig. 4.1. The current induced in the coupling loop attached to the AJJ is proportional to the persistent current in the flux qubit. Thus, the persistent current in the qubit manifests itself in the AJJ as a current dipole with an amplitude μ on top of the homogeneous background of bias current. Similar models, but for the static fluxon and the static dipole, were already considered in the past in [MU04, GSK04]. In our case the situation is different as the fluxon moves. When the fluxon scatters on a positive current dipole, it is first accelerated and then decelerated by the dipole poles. In the ideal case of absence of damping and bias current, the sign of frequency change $\delta\nu$ is determined only by the polarity of the dipole (see Fig. 4.2).

In the presence of finite damping and homogeneous bias current, the situation completely changes - as the total propagation time becomes dependent on the complex interplay between bias current, current dipole strength and damping. In this real case, taking into account the damping, which itself dependens on the fluxon velocity, the homogeneous bias current γ_0, the fact that the acceleration and the deceleration now happens on different spatial scales, we obtain an intricate nonlinear system to deal with. The response of this dynamical system on the introduction of the fixed current dipole with the strength μ on top of the homogenous bias current γ_0 can be much more complex than it was for the case of Fig. 4.2.

One of the possible scenarios for the fluxon scattering on the current dipole to happen in the case of damped and biased long Josephson junction is shown in Fig. 4.3. The considered figure was drawn for a case of low bias current $\gamma_0 \sim 0.05$ and $\alpha \sim 0.01$ so that the fluxon velocity is small comparable with the Swihart velocity $u \ll c_0$. Looking at Fig. 4.3 it is not simple to evaluate what frequency change such a scattering process causes as it is needed to calculate a fluxon propagation time T for every phase trajectory and compare them to each other. To do this two parallel approaches were used as described in the further subsections.

4.1.1 Perturbation approach

A classical theoretical description of interaction between the Josephson vortex and the current dipole in the AJJ can be done in terms of the well-known perturbed sine-Gordon equation (PSGE) [MU04, GSK04, MS78]:

$$\frac{\partial^2\varphi}{\partial t^2} + \alpha\frac{\partial\varphi}{\partial t} - \frac{\partial^2\varphi}{\partial x^2} = \gamma - \sin(\varphi) + \mu(\delta(x - d/2) - \delta(x + d/2)), \quad (4.1)$$

with the periodic boundary conditions

$$\varphi(-l/2, t) = \varphi(l/2, t) + 2\pi n, \frac{\partial\varphi(-l/2, t)}{\partial x} = \frac{\partial\varphi(l/2, t)}{\partial x}, \quad (4.2)$$

where n is the number of trapped fluxons, $\gamma = I_b/I_c$ is the normalized bias current, $\alpha = \omega_p/\omega_c$ is the damping parameter, $l = L/\lambda_J$ is the

normalized junction circumference, $\mu = I_\mu/(j_c\lambda_J W)$ is the amplitude of the current dipole and $d = D/\lambda_J$ is the normalized distance between the dipole poles. Direct analytic solution of (4.1) is not an easy task. Therefore, we analyze Eq. (4.1) using the perturbation approach developed in [MS78]. In the limit of small perturbations $\gamma \ll 1, \alpha \ll 1$ and $\mu \ll 1$, the motion of a single fluxon in the AJJ can be described by a system of ordinary differential equations for the fluxon velocity $u(t)$ and its spatial coordinate $X(t)$:

$$\frac{du}{dt} = -\frac{\pi\gamma}{4}(1-u^2)^{3/2} - \alpha u(1-u^2) - \frac{\mu}{4}(1-u^2)\times \\ \times\left[\mathrm{sech}\frac{\mathrm{d}/2-\mathrm{X}}{\sqrt{1-\mathrm{u}^2}} - \mathrm{sech}\frac{-\mathrm{d}/2-\mathrm{X}}{\sqrt{1-\mathrm{u}^2}}\right], \tag{4.3}$$

$$\frac{dX}{dt} = u - \frac{\mu u}{4}\left[(d/2-X)\mathrm{sech}\frac{\mathrm{d}/2-\mathrm{X}}{\sqrt{1-\mathrm{u}^2}} + \right. \\ \left. +(d/2+X)\mathrm{sech}\frac{-\mathrm{d}/2-\mathrm{X}}{\sqrt{1-\mathrm{u}^2}}\right], \tag{4.4}$$

$$u(-l/2) = u(l/2). \tag{4.5}$$

Calculation of phase trajectories

By numerically solving (4.3)-(4.5) as a parametric set of first order differential equations with variables $X(t)$ and $u(t)$ one can calculate an equilibrium trajectory in phase space for fluxon oscillations in the AJJ with the current dipole. The standard procedure was the following: one starts with an initial guess value $u(t=0)$ for the fluxon velocity and $X(t=0) = -l/2$ for the fluxon initial coordinate and then calculates the trajectory $X(t)$ in a time span from 0 to a value T. The value T should be simply large enough so that $X(t_l < T) = l/2$. After this step, the value of fluxon velocity $u(t_l)$ has been evaluated and compared with the initial guess $u(t=0)$. If the difference $\delta u = u(t_l) - u(t=0)$ is larger than a predefined constant $|\delta u| > \delta_0$, the initial guess value is changed according to a special algorithm and the whole calculus is repeated. This procedure is done until the right initial guess is found which corresponds to the condition $\delta u < \delta_0$. Thus, setting δ_0 to be small enough, one can find a solution for the perturbed set of equations (4.3)-(4.5). Taking into account that a perturbation by the current dipole is

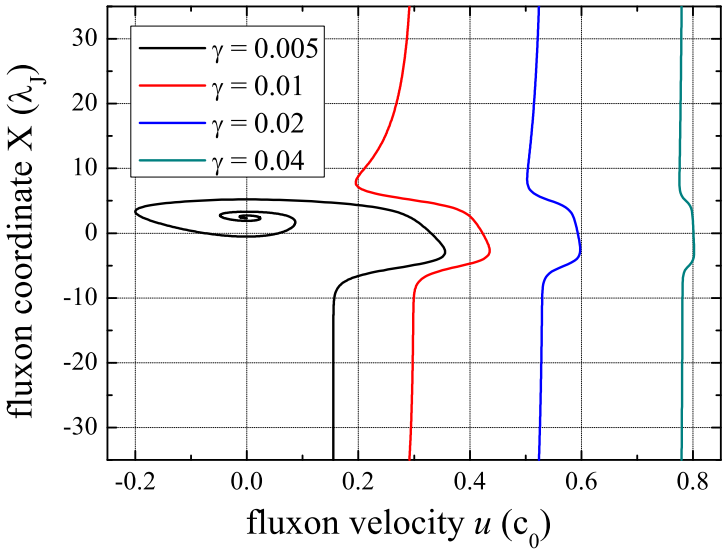

Figure 4.4: Examples of the phase trajectories for the fluxon scattering on the current dipole in the AJJ for the different bias currents. Other system parameters were the following: $\mu = 0.1$, $l = 70$, $\alpha = 0.025$, $d = 10$.

considered to be small, the unperturbed value of fluxon velocity $u_0 = \frac{1}{\sqrt{1+(4\alpha/\pi\gamma)}}$ (2.32) can be safely taken as the initial guess. The precision constant was usually set to about $\delta_0 \sim 10^{-14}$ to achieve the required precision in numerical simulations. The whole programming has been done in Wolfram Mathematica 7.0. The calculation time of a single equilibrium phase trajectory using the described method took about $5 - 10$ seconds and provides a great flexibility and speed in estimating different outcomes for different system parameters.

Examples of the resulting phase trajectories are shown in Fig. 4.4. One can see that the current dipole strongly changes the fluxon velocity locally for the small bias currents $\gamma \sim 0.01$ which eventually can even lead to a pinning of the fluxon at the poles of the current dipole (the black curve in Fig. 4.4). For larger γ, the influence of the current dipole decreases as it should because of the increasing fluxon energy.

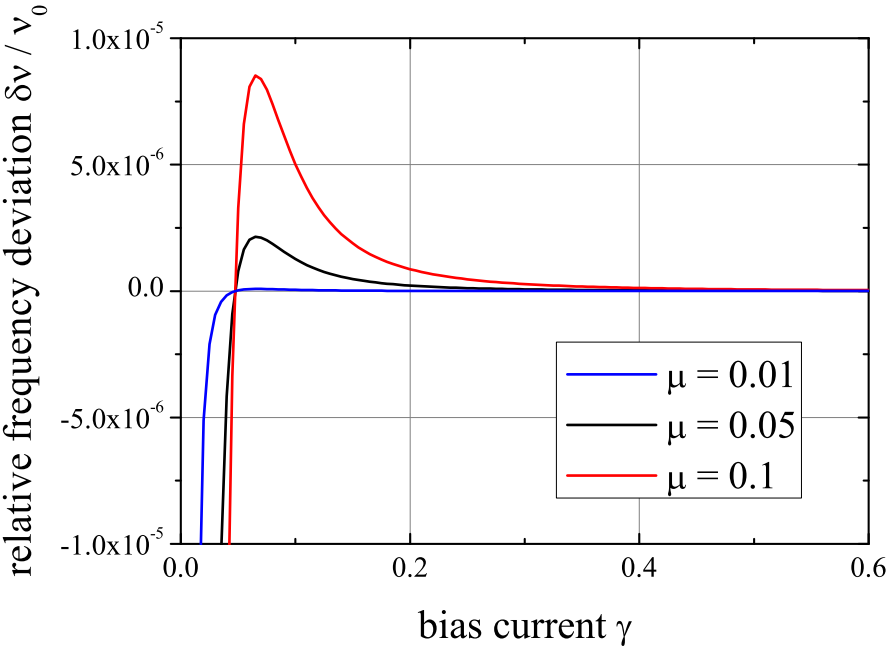

Figure 4.5: Equilibrium frequency deviation of the fluxon in the AJJ due to the scattering on the current dipole with different strengths μ. The other system parameters were the following: $l = 20$, $\alpha = 0.02$, $d = 2$.

Equilibrium frequency deviation

Using the calculated phase trajectories for the fluxon scattering on the current dipole in the AJJ, one can estimate the deviation of fluxon oscillation frequency from the unperturbed case $\delta\nu = \nu_\mu - \nu_0$, where ν_0 is the oscillation frequency for $\mu = 0$. The black line in Fig. 4.5 shows the dependence of the relative deviation $\delta\nu/\nu_0$ versus bias current γ calculated from the perturbation theory for the following set of system parameters: $l = 20$, $\alpha = 0.02$, $\mu = 0.05$, $d = 2$. The deviation $\delta\nu$ is large and negative for small bias currents $\gamma \ll 0.1$, what means that the fluxon is slowed down by the current dipole and eventually can be pinned at the dipole if the bias current is too small. Surprisingly, for larger currents $\gamma > 0.05$, the sign of $\delta\nu$ becomes positive indicating that the current dipole accelerates the fluxon. To understand this phenomenon, we need to look at Eq. (4.3) and notice that the effective

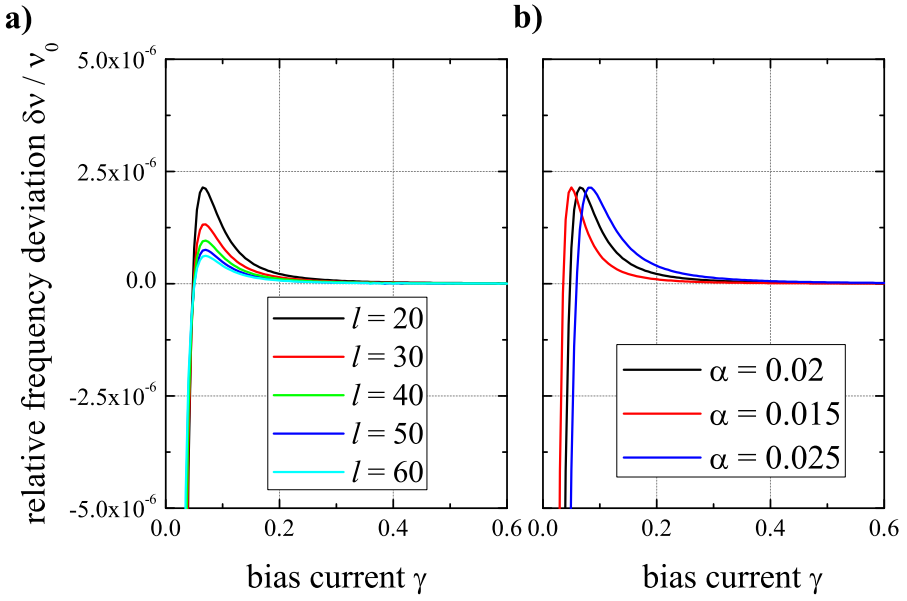

Figure 4.6: Equilibrium frequency deviation (the vertical axis is common for the both graphs) of the fluxon in the AJJ due to the scattering on the current dipole. The system parameters were the following: **a)** $\alpha = 0.02$, $\mu = 0.05$, $d = 2$; **b)** $l = 20$, $\mu = 0.05$, $d = 2$.

damping term $\alpha_e = \alpha u(1 - u^2)$ has a non-monotonic behavior. When increasing the fluxon velocity u, the effective damping is increased for $u \leq 1/\sqrt{3}$ and then starts to decrease. This means that deceleration (acceleration) is favorable for low (high) bias currents.

Figure 4.6 illustrates the dependence of the relative fluxon frequency deviation $\delta\nu/\nu$ versus the damping and the length of the AJJ. Generally, with higher damping the transition point from negative to positive $\delta\nu$ shifts to larger bias currents. The AJJ length influences only the amplitude of the frequency deviation leaving the position of the transition point intact.

4.1.2 Numerical simulation

To verify the results of the perturbation theory, we performed direct numerical simulation of Eq. (4.1) with the delta functions replaced by

the hyperbolic secants in order to smoothen the current distribution:

$$\frac{\partial^2\varphi}{\partial t^2} + \alpha\frac{\partial\varphi}{\partial t} - \frac{\partial^2\varphi}{\partial x^2} = \gamma - \sin(\varphi) + \\ + \frac{\mu}{\pi a_d}\left[\operatorname{sech}\left(\frac{x-d/2}{a_d}\right) - \operatorname{sech}\left(\frac{x+d/2}{a_d}\right)\right]. \tag{4.6}$$

The parameter a_d characterizes the width of current distribution and is $a_d \sim 1$ in the experiment. The prefactor $B = 1/(\pi a_d)$ is chosen to keep the normalization constraint $B\int_{-\infty}^{+\infty}\operatorname{sech}((x-d/2)/a_d)dx = 1$. The simulation of (4.6) with the boundary conditions (4.2) was done with the use of the original modification of the implicit finite-difference scheme [Zha91]. It is based on the reduction of derivatives in (4.6) and (4.2) by finite differences and transforming the whole equation to a set of N linear equations in the form of a quasi-triangular matrix. Matrix inversion was done with the use of methods provided by the Numerical Recipes textbook [PTF07]. The resulting scheme was verified in various ways and used many times before for simulating the PSGE equation [FP07b, FP09, FFU11]. The precision of the numerics was mainly controlled by discretization steps in time Δt and in space Δx. To achieve a precision which can be compared with the results of perturbation theory, these discretization steps should be around $\Delta t \simeq \Delta x \simeq 10^{-5}$ which yields for the typical AJJ length of $l = 20$ and time $T_{max} = 1000$ around $N \simeq 2 \cdot 10^{14}$ points to be calculated. Due to this extreme task the program was rewritten to employ OpenMP techniques and was run on several nodes of the KIT computational cluster HC3 which allowed to rapidly perform all required calculations using parallel computing. "Rapidly" here means that the typical calculation time for a single curve was about $2-3$ days using 3 eight cores nodes (the same task running on a single threaded machine of comparable power would take a couple of months).

The red curve in Fig. 4.7 shows the results of the numerical calculations of Eq. (4.6) with boundary conditions (4.2). As it can be seen in Fig. 4.7, results of the numerical simulations qualitatively agree with the perturbation theory. We see that this agreement is improving for smaller a_d as Eq. (4.6) takes form of Eq. (4.1) in the limit of $a_d \to 0$.

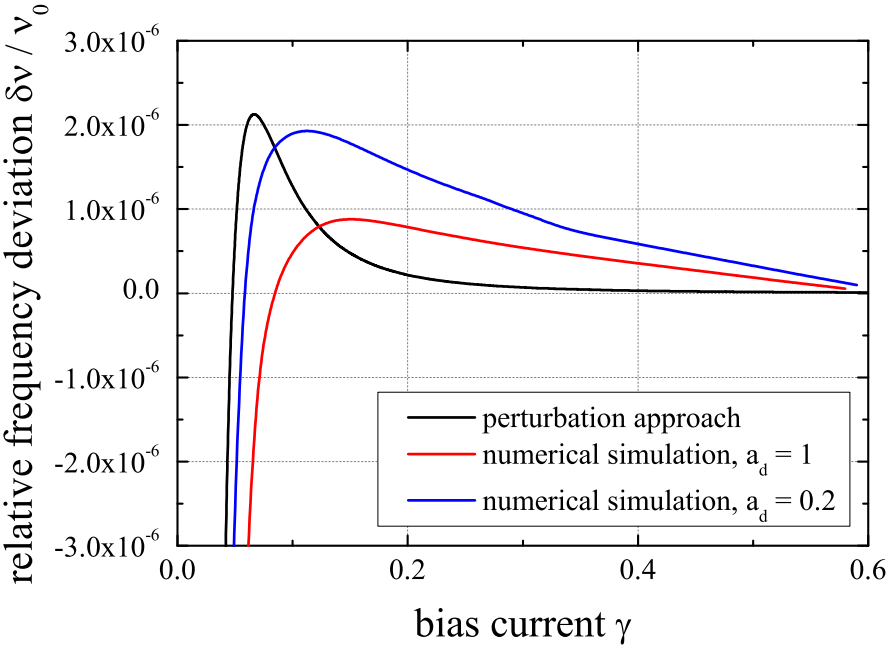

Figure 4.7: Relative frequency deviation from the equilibrium $\delta\nu/\nu_0$ of the fluxon oscillation frequency versus bias current. The black line shows the result of perturbation approach, while the red line depicts results of direct numerical simulations of the PSGE equation (4.6) with $a_d = 1$. The blue curve corresponds to the case with $a_d = 0.2$.

4.1.3 Flux qubit as a current dipole

In the experiments, the current dipole amplitude was controlled by the persistent current in the coupled flux qubit:

$$\mu = \frac{kI_p}{j_c \lambda_J W}, \tag{4.7}$$

in the absence of offset current $\mu_0 = 0$. The proportionality coefficient $k = M/L_{CL}$ was determined by a mutual inductance between the qubit and the coupling loop M, and by a self-inductance of the coupling loop. A persistent current I_p of the ground state in the flux qubit can be calculated by a numerical simulation of its Hamiltonian [Orl99].

The fluxon response to the persistent current in the flux qubit loop is depicted in Fig. 4.8 by the red curve. It was calculated for a fixed

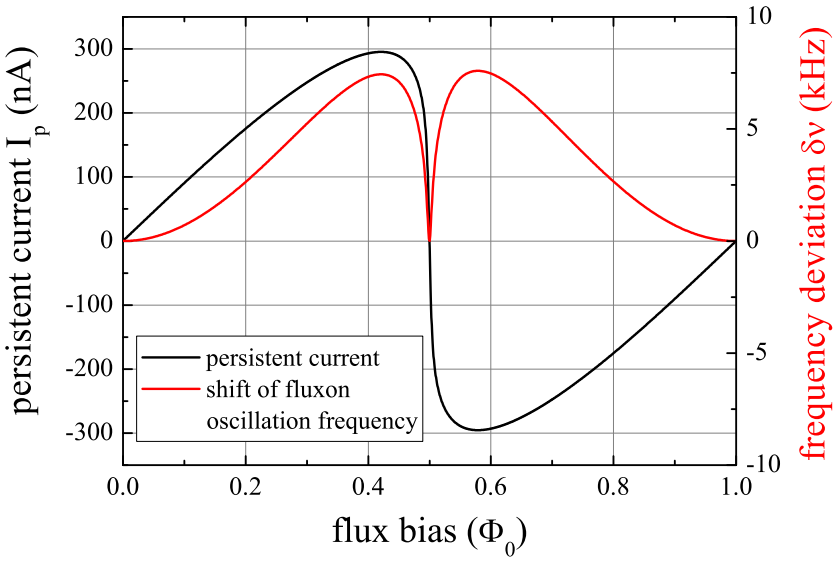

Figure 4.8: Persistent current for a ground state of the flux qubit versus magnetic frustration (black line). The red line shows the corresponding fluxon shift calculated using the perturbation theory for the following parameters: $\gamma = 0.2$, $l = 20$, $\alpha = 0.02$, $\mu_{max} = 0.05$.

bias current $\gamma = 0.2$, $l = 20$, $\alpha = 0.02$, $\mu_{max} = 0.05$ using the presented perturbation theory (4.3)-(4.5). The response is indicated in kHz assuming $\nu_0 \sim 13$ GHz (as it corresponds in experiment to the bias current $\gamma \sim 0.2$). Noticeably, the response signal $\delta\nu$ is approximately proportional to the amplitude of the persistent current and stays positive despite the change of the sign of I_p. The asymmetry of deviation $\delta\nu$ for the positive and negative branches of I_p is less than 3%. This means that the fluxon scattering is nearly independent of the polarity of the current dipole. It depends dominantly on the bias γ and the absolute amplitude of the current dipole μ.

The surprising independence of the fluxon scattering on the dipole polarity can be explained noticing that the dipole length d is much larger than the characteristic size of the fluxon at relativistic velocities, the contributions of the separate dipole poles to $\delta\nu$ is additive and

is not dependent on their order. For small bias currents (small fluxon velocities) or small dipole lengths, when d is comparable with the fluxon size, $\delta\nu$ becomes dependent on the dipole sign.

4.2 Experimental results

In this section the experimental results on the fluxon readout are presented. They consist of measurements of the fluxon radiation frequency shift versus flux bias through the coupled superconducting flux qubit. This flux bias was created by a current through the control line (see Fig 4.9). Further presented results include spectroscopy measurements of the flux qubit.

Four different samples with deposited qubits will be considered in the respective measurements. The first two of them (#1 and #2) have been implemented with weak coupling, the other two (#3 and #4) were strongly coupled.

4.2.1 Fluxon and flux qubit: weak coupling

The coupling between the fluxon in the AJJ and the flux qubit can be estimated in terms of the maximum dipole the qubit can create in the AJJ. The first sample #1 (whose optical photo with the electric schematics is shown in Fig 4.9) had a maximum estimated current dipole amplitude of about $\mu_{max} \simeq 3 \cdot 10^{-5}$. One can calculate this value from (4.7) assuming the mutual inductance $M \simeq 6 \cdot 10^{-12}$ H, the coupling loop self-inductance $L_{CL} \simeq 1.7 \cdot 10^{-10}$ H, the maximum persistent current $I_p \simeq 300$ nA, the critical current density $j_c \simeq 800$ kA/cm^2, the Josephson length $\lambda_J \simeq 12$ μm, and the AJJ width $W \simeq 5$ μm. This case is considered as the *weakly* coupled qubit.

It is needed to note that this classification of coupling is not intended to be linked with quantum information processing standard definitions on strong and weak coupling.

Sample and flux qubit

The annular Josephson junction shown in Fig. 4.9 was fabricated using photolithography and a standard Nb/AlO_x/Nb trilayer process with

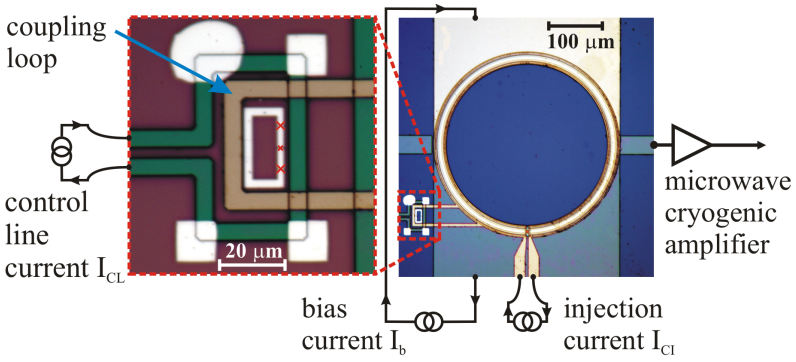

Figure 4.9: Optical photograph of the chip with the annular Josephson junction on the right part and experimental set-up schematics. The left part shows a zoom into the area with the flux qubit with a coupling loop (yellow loop) and control line (green loop). Red crosses indicate the positions of three Josephson junctions in the flux qubit loop. Sample #1.

a critical current density $j_c \simeq 1$ kA/cm^2. The estimated Josephson penetration depth is $\lambda_J \simeq 12\,\mu$m, the Josephson plasma frequency $\omega_p/2\pi \simeq 124$ GHz, and the estimated damping parameter $\alpha \simeq 0.02$. The circumference of the junction $L = 880$ μm determines the frequency of the radiation corresponding to a single fluxon moving with the Swihart velocity c_0 to be at about 15 GHz. The width of the AJJ was $W = 2\mu$m and its fluxon free critical current $I_c = 23$ mA.

The flux qubit was made using a standard aluminum shadow evaporation process [Dol77, Moo99] and was deposited after the niobium structures were fabricated. Estimated parameters for the Josephson junctions in the flux qubit loop were the following: critical current $I_c = 380$ nA, alpha factor $\alpha_q = 0.54$, ratio of Josephson and charging energies $E_J/E_C = 830$. The post-deposition of all aluminum qubits was done in KIT Campus Nord facilities by Anastasia Shcherbakova. Figure 4.9 presents the optical photograph of the first flux qubit (on the left part). To resolve the samll Josephson junctions in the flux qubit in detail a scanning electron microscope (SEM) was used due to their small lateral sizes ($\sim$ 200 nm). Figure 4.10 provides the examples of such SEM images.

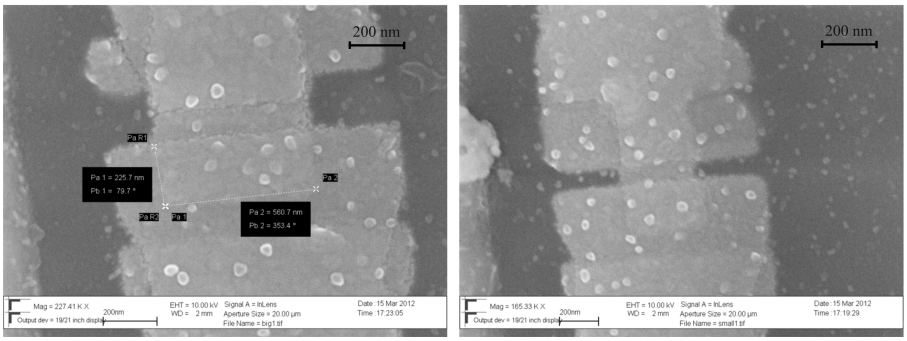

Figure 4.10: Scanning electron microscopy pictures of Josephson junctions intersecting the flux qubit loop. On the left hand side the normal junction is shown. The right picture illustrates the α-junction. Sample #1.

Fluxon frequency shift

The fluxon radiation was detected as described in the Chapter 3 using the dilution refrigerator experimental set-up. The zero-field resonance step for this particular sample at liquid helium temperature is shown Fig. 4.11.

To experimentally test the qubit readout scheme discussed above, the temperature was lowered to $T \simeq 70$ mK, well below the superconducting transition temperature T_c of aluminum forming the qubit. The long junction was biased at a fixed current I_b. Then, we varied the current through the control line I_{CL} in order to change the magnetic flux through the flux qubit. The experimental curve showing the reaction of the fluxon to the magnetic flux through the flux qubit are presented in Fig. 4.12. The periodic modulation of the fluxon frequency versus magnetic flux through the qubit corresponds to the changing of the persistent currents in the qubit as Fig. 4.12 suggests. We did not observe clear and narrow peaks at the half flux quantum point, most probably due to excess fluctuations. Emerging dip-like peculiarities can be noted at presumed half flux quantum points which suggest that the dips may be there, covered by noise and insufficient resolution. Further improvements of the experimental setup are required to resolve these dips. The presented measurement curve has a convex profile which in-

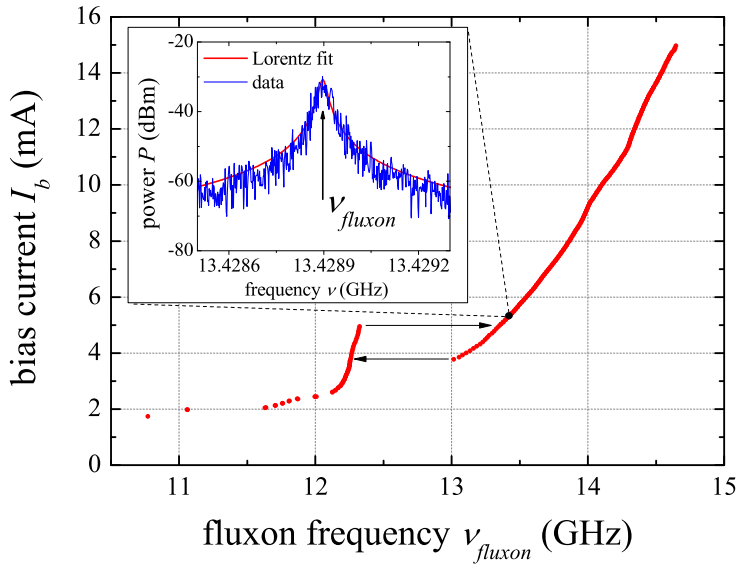

Figure 4.11: Zero-field step measured in the frequency domain for the ambient temperature $T = 4.2$ K and injection current $I_{CI} = 3.973$ mA. The inset shows the sample spectrum for the fixed bias current $I_b = 5.3$ mA with the respective Lorentz fit. Sample #1.

dicate that indeed the deviation of frequency $\delta\nu$ is positive, consistent with predictions made by the perturbation approach and the numerical simulations.

Advanced samples

For the first sample, clear indications of the qubit interaction with the fluxon in the AJJ were observed. However, the quality of the aluminium film forming the flux qubit was questionable from the very beginning and absence of narrow qubit dips in Fig. 4.12 also suggested that something might be wrong with the qubit itself. Therefore, additional qubits have been fabricated with the use of an UHV evaporation chamber with a much better vacuum and, thus, a much better quality and reproducibility of the final aluminum flux qubits. The same type

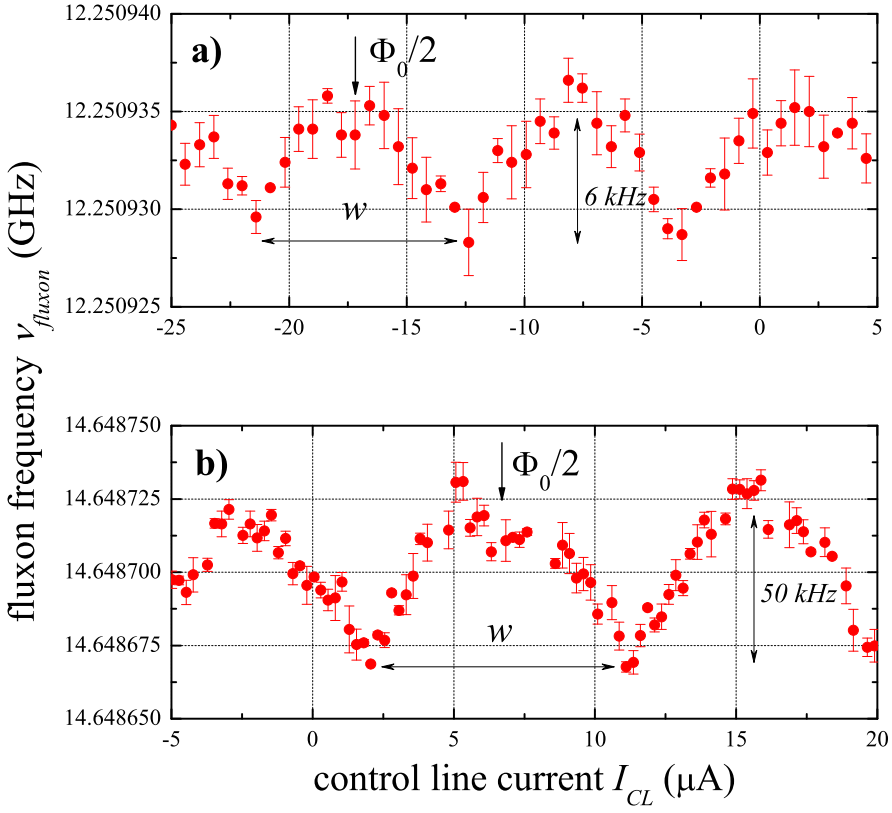

Figure 4.12: Variations of the fluxon frequency ν_{fluxon} versus the current through the control line I_{CL} (the flux bias) due to the coupling to the flux qubit. a) The bias current $I_b = 12.0$ mA, in the normalized units $\gamma = 0.521$. b) The bias current $I_b = 1.1$ mA, in the normalized units $\gamma = 0.048$. Sample #1.

of samples with annular Josephson junctions was used as it was shown in Fig. 4.9. The design parameters of those qubits were a bit different: critical current $I_c = 500$ nA, alpha factor $\alpha = 0.63$, ratio of charging and Josephson energies $E_C/E_J = 0.0034$. In order to decrease the low-frequency fluctuations in the experimental setup, the whole dc room-temperature electronics were switched to a battery supply as described before in Section 3.2.3. The latter change was crucial and allowed to observe clear indications of fluxon-qubit interactions.

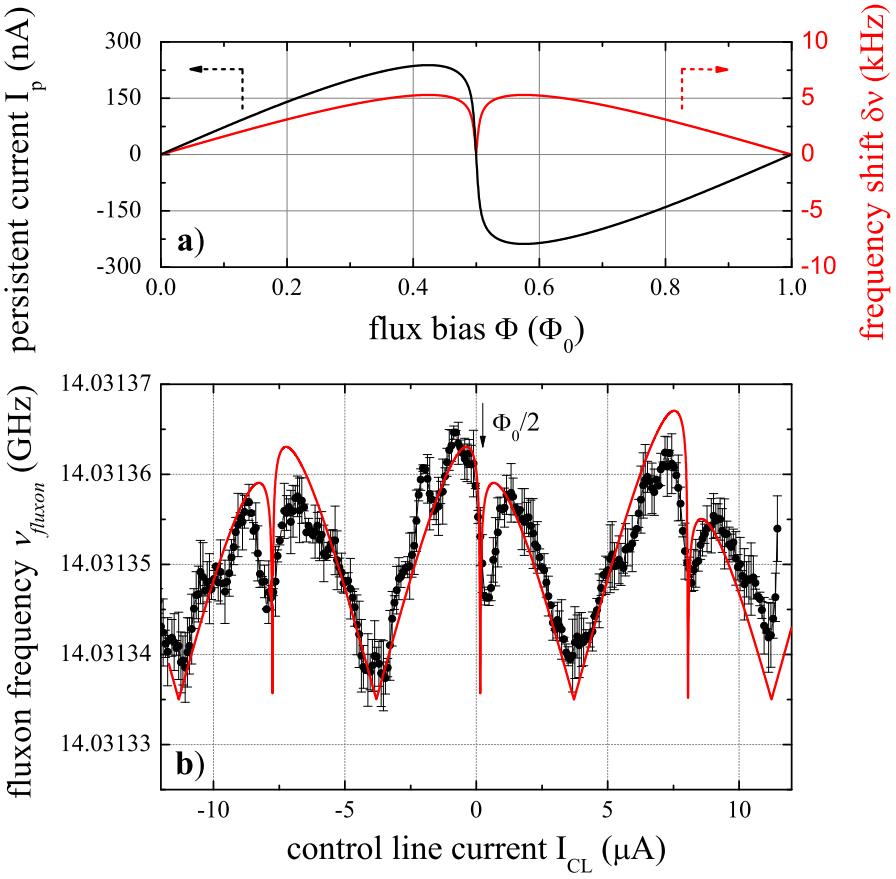

Figure 4.13: a) Theoretical persistent current I_p of the ground state of the flux qubit versus magnetic frustration (black line) calculated for our flux qubit parameters. The red line shows the expected fluxon frequency shift in kHz for $\gamma = 0.4$. **b)** The experimentally measured modulation of the fluxon oscillation frequency due to the coupling to the flux qubit. Black dots show the measured mean frequency of fluxon oscillations. Every point consists of 100 averages; bias is $\gamma = 0.39$. The red line shows the corresponding fit. Sample #2.

For the sample #2 with the "advanced" qubit, Fig. 4.13.b) shows the experimental shift of the fluxon oscillation frequency due to the coupling to the flux qubit at the fixed bias current $\gamma = 0.39$. We measured a Lorentzian radiation peak of fluxon oscillations in the AJJ for fixed values of I_{CL} and then determined the mean frequency ν_f for which the radiation power was maximal. The narrow flux qubit peaks are clearly seen in the presented figure. To fit our experimental data with theory, we take into account the parasitic coupling between the control line current and the fluxon leading to an additional linear shift of ν_f versus I_{CL}. The corresponding fit is presented by the red line in Fig. 4.13.b showing fairly good agreement between theory and experiment. Smaller irregular peaks visible in Fig. 4.13.b are low-frequency fluctuations, most probably arising from trapped Abrikosov vortices in the superconducting leads of the AJJ. Presumably, these Abrikosov vortices are also responsible for the parasitic flux offset in Fig. 4.13.b as this offset varied for different cooldowns.

To speed up the measurement process and decrease the noise, we switched to zero-frequency span and measured the power at the fixed frequency $\nu_f + 50$ kHz. Figure 4.14.b) shows the results of such measurements around $\Phi \sim \Phi_0/2$. A sharp dip is clearly visible at a flux bias of $\Phi_0/2$ as well as two other smaller symmetric satellites around it. These satellites occur when the energy splitting E_{01} between the ground and excited states of the qubit coincides with the fluxon oscillation frequency ν_f. This leads to a change of the persistent current in the qubit for two values of flux bias Φ shown by the black line in Fig. 4.14.a). The theoretical fit of the data for the fluxon resonance frequency $\nu_f = 14.031$ GHz is presented by the red line in Fig. 4.14.b). At resonance, pumping at the fluxon frequency should lead to Rabi oscillations in the flux qubit between its ground and excited states and, therefore, the measured signal reflects a mixture of the ground and the first excited states. This operation is similar to resonant interaction between qubit and resonator in a cavity QED setup.

It is important to note that, in real experiments, the values of maximum current dipole is usually of the order $\mu_{max} \sim 10^{-5}$ which is much smaller than the discussed values $\mu_{max} \sim 0.05$. The problem here lies in the fact that the effective differential resistance $R_d = \partial\nu/\partial\gamma$ differs a

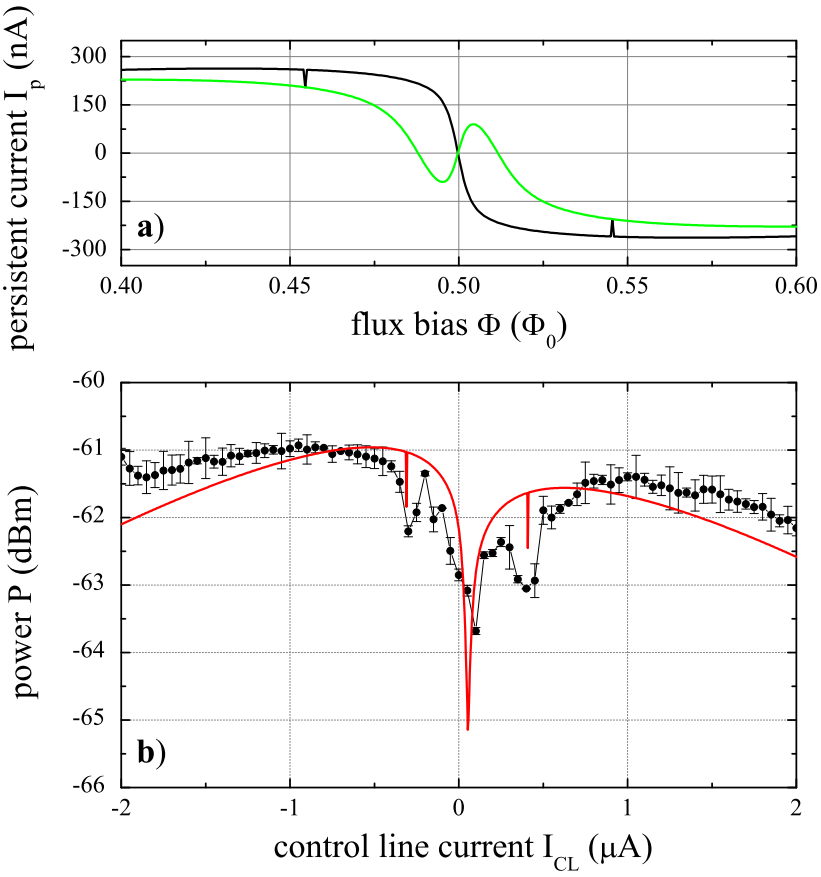

Figure 4.14: **a)** The theoretically expected persistent current I_p for the ground state of the flux qubit versus magnetic flux (black line). The spikes indicate presumed transitions to the first excited state at flux bias points corresponding to $E_{12} = 14$ GHz flux qubit energy splitting. The green line shows the expected persistent current I_p for the first excited state. **b)** Modulation of the fluxon's oscillation frequency due to the coupling to the qubit, measured in the power domain. Measured power P relates to the power at the fixed frequency offset +50 kHz from the fluxon mean oscillation frequency ν_f. Every point consists of 10 averages with video filter bandwidth of 10 Hz. The red line depicts the corresponding theory fit. Sample #2.

lot between the experiment and the theory. This is due to the presence of the fine structure in the experimental zero-field steps. At the same time, the differential resistance affects strongly the sensitivity of the fluxon frequency shift due to the scattering on the current dipole. The theoretical value of R_d can be easily calculated using equation (2.32):

$$R_d^T = \frac{1}{l}\frac{\partial u}{\partial \gamma} = \frac{16\alpha^2}{l\pi^2\gamma^3(1+(4\alpha/\pi\gamma)^2)^{\frac{3}{2}}}. \tag{4.8}$$

The experimental value of differential resistance R_d^E can be extracted from the zero-field measurements in the frequency domain. The ratio between these two R_d^E/R_d^T can vary a lot. For typical good working points, the experimental R_d^E is much larger than the theoretically expected values and the sought-for ratio turns to be large $R_d^E/R_d^T \sim 10^3$. So, one can estimate the effective current dipole amplitude as $\mu_{max}^e = \mu_{max} \cdot R_d^E/R_d^T \sim 0.05$ for the typical working points of the fluxon readout. The corresponding amplitude of the fluxon frequency modulation due to the current dipole scattering is about 10 kHz which lies in the same range with the measured values of 20 kHz. This approach of using the effective current dipole amplitude is a purely phenomenological one but allows to achieve a reasonable quantitative agreement between the theory and the experiment.

Flux qubit spectroscopy

As the last step, we performed microwave spectroscopy of the qubit. We applied an additional continuous excitation tone from an external microwave source at the frequency ν_e and swept the control line current between two resonant dips due the excitation of the qubit (as it was discussed earlier). The output from microwave source was typically set at a constant power $P_e \simeq -15$ dBm, which corresponds to approximately -90 dBm of the microwave power at the excitation antenna. The first reasonable measurement results for fluxon readout of flux qubits were obtained by the frequency detection method (rather unreliable in comparison with the amplitude detection). These results are presented in Fig. 4.15.a) and are related to the sample #1. One can see a couple of traces marked by dark-green pixels on the spectrum. These traces correspond well to the theoretical fits for the flux qubit with the following

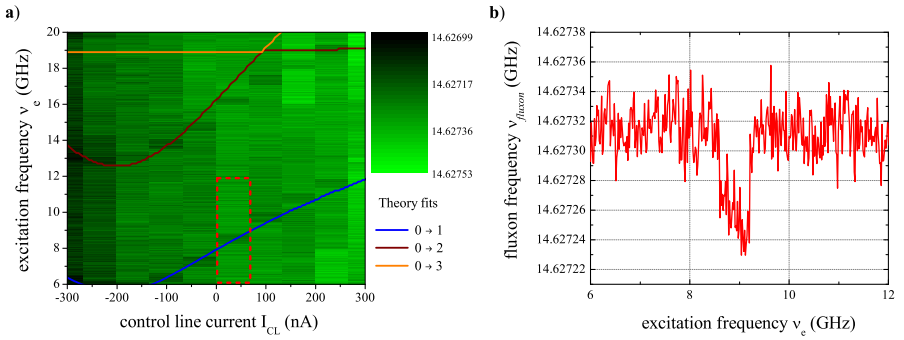

Figure 4.15: First spectroscopic measurements of a flux qubit. **a)** Fluxon response on the microwave excitation applied to the flux qubit. Color scale corresponds to the detected frequency. The flux qubit spectrum can be seen as the trace of dark-green spots. The solid colored lines depict the corresponding fit for transitions between quantum levels in the flux qubit. **b)** The cross section of the spectrum made for the region underlined by the red box. The characteristic dip in the fluxon frequency for certain excitation frequency corresponds to qubit transition from the ground to the first excited state. Sample #1.

parameters: critical current $I_c = 380$ nA, alpha factor $\alpha = 0.54$, ratio of charging and Josephson energies $E_J/E_C = 0.0012$. A cross section of this spectrum for a fixed flux bias also shown in Fig. 4.15.b) in order to illustrate a particular transition from the ground to the first excited state in the flux qubit due to the resonant excitation by the external microwave signal.

The frequency detection method is inherently slower and less reliable (more noisy) than the amplitude one. So, for later qubit scans the latter was mostly used. The color-plot of $P(\nu_e, I_{CL})$ is shown in Fig. 4.16, corresponding to the sample #2 (Fig. 4.14 illustrates modulation of the fluxon frequency versus the flux bias for the same sample). The signal of the fluxon readout for every flux bias point without microwaves was subtracted from the actual response with microwaves to get rid of an unwanted background slope. One can clearly recognize the hyperbola of the flux qubit spectrum [Moo99] as a white-blue curved line between 2 and 10 GHz, with the minimal energy splitting $\Delta \simeq 2.7$ GHz. We can

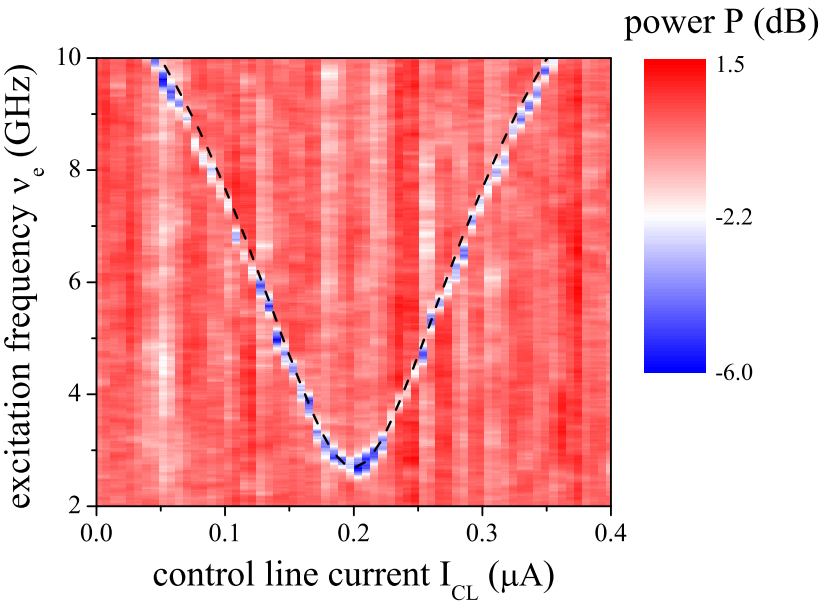

Figure 4.16: Fluxon response on the microwave excitation applied to the flux qubit. Color scale corresponds to the detected power. Measured power P relates to the power at the fixed frequency offset +50 kHz from the fluxon mean oscillation frequency ν_f. Every point consists of 10 averages with video filter bandwidth of 1 Hz. The flux qubit spectrum can be clearly seen as the blue curved trace. The black dashed line depicts the corresponding fit of the flux qubit. Sample #2.

very well fit the measured spectrum by the theoretical curve (shown by the black dashed line in Fig. 4.16) for the following parameters: critical current $I_c = 320$ nA, alpha factor $\alpha_q = 0.58$, ratio of charging and Josephson energies $E_J/E_C = 0.0034$.

The results of both presented measurements are the same (though, the quality of the second is much better). However, the first one is very useful from the instructive point of view as it shows the direct experimental frequency shift of the fluxon in the AJJ due to the quantum level transition in the flux qubit.

4.2.2 Fluxon and flux qubit: strong coupling

In the strongly coupled case (samples #3 and #4) the inductances are different (the coupling loop is significantly shorter and the qubit, overall, is closer to the JTL): $M \simeq 7 \cdot 10^{-12}$ H and $L_{CL} \simeq 6 \cdot 10^{-11}$ H. Other parameters stay the same except for the maximum persistent current in the flux qubit $I_p \simeq 400$ nA. The corresponding maximum current dipole is about $\mu_{max} \simeq 1 \cdot 10^{-4}$. The initial idea for employing such coupling was, of course, that a larger coupling should also provide a larger qubit signal.

Fluxon frequency shift

The measurements of the fluxon frequency shift versus the flux bias through the qubit was done in the same way as described before. Fig. 4.17 depicts the dependence of the measured microwave power at the fixed frequency offset +50 kHz from the fluxon mean oscillation frequency ν_f. One can notice that the linear slope observed in this figure is much larger than before for the samples with weak coupling. This, obviously, happens because the control line is more strongly coupled directly to the fluxon than before. But the most interesting feature here is that we did not observe any qubit-like peculiarities around the presumed half-flux quantum point (marked by the arrow in Fig. 4.17). However, a strange symmetric peak-dip structure was found around $\sim \Phi_0/4$ point (underlined by the black dashed line). A crazy idea to explain this can be that, by some reason, the point where the transition energy between the ground and the first excited states are minimal (the frustration point) E_{12} is shifted. The reason for this can be that the strongly coupled fluxon magnetically perturbs the qubit so much that it effectively shifts the working point of the latter.

One might ask why the whole curve is not shifted then by the same amount as the flux qubit symmetry point did. A possible answer might be that while the fluxon is far from the qubit (which is true for around 95 % of total time) there is no interaction (and perturbation) between them. Therefore, the current dipole strength is controlled by the unperturbed persistent current in the qubit loop (plus the direct effect from the control line current itself). When the fluxon scatters on the flux

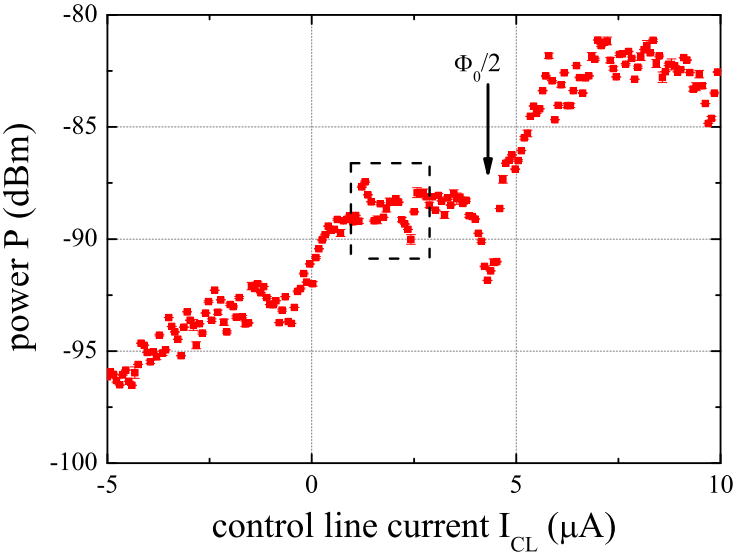

Figure 4.17: Modulation of the fluxon oscillation frequency due to the coupling to the qubit, measured in the power domain. Measured power P relates to the power at the fixed frequency offset +50 kHz from the fluxon mean oscillation frequency ν_f. Every point consists of 10 averages with video filter bandwidth of 10 Hz. The area underlined by the black dashed line shows is a presumable flux qubit working point. Sample #3.

qubit, it feels the flux qubit mostly as the unperturbed current dipole. It does not feel the shift of the flux qubit state which is induced by itself. However, when the fluxon shifts the flux bias point of the qubit exactly in resonance with the resonance frequency of the latter - there is a finite probability that the qubit will instantly absorb a photon generated by the fluxon motion and change its state from the ground to the first excited one. Then the qubit stays in this state for the time equal to its energy relaxation time T_1. This new state corresponds to another persistent current and, thus, to another current dipole amplitude which is reflected in the measurements (see Fig. 4.17, the dashed line box). Of course, this idea is rather "hand-weaving" and requires a proper theoretical proof to become a valid argument.

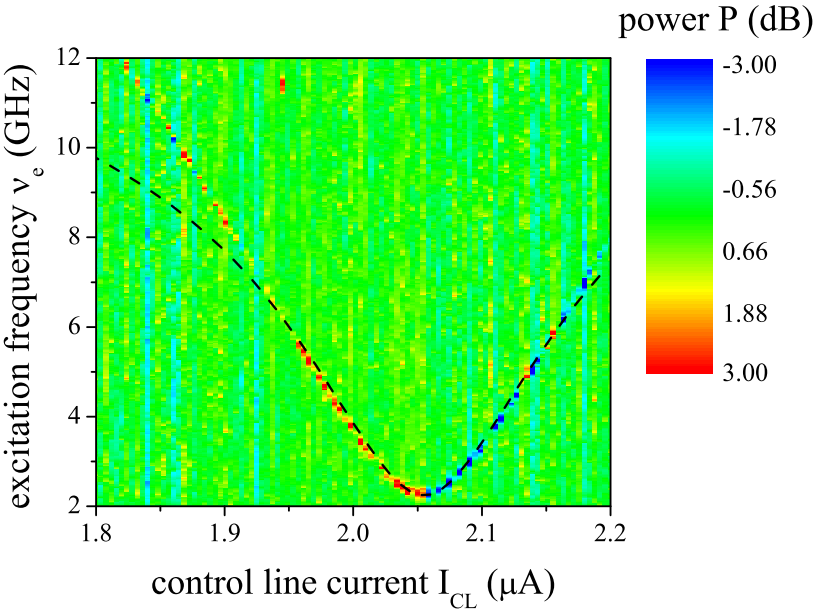

Figure 4.18: Fluxon response on the microwave excitation applied to the flux qubit strongly coupled to the AJJ. Color scale corresponds to the detected power. Measured power P relates to the power at the fixed frequency offset +50 kHz from the fluxon mean oscillation frequency ν_f. Every point consists of 10 averages with a video filter bandwidth of 1 Hz. The flux qubit spectrum can be clearly seen as the red-blue curved trace. The black dashed line depicts the corresponding fit of the flux qubit. Sample #3.

Flux qubit spectroscopy

To check the hypothesis described above one can do a very simple thing: sweep the control line current I_{CL} in between the peak and the dip, and apply an additional continuous excitation tone at the fixed frequency ν_e from the external microwave generator. Basically, it means to do the standard spectroscopy measurements around the shifted working point.

Figure 4.18 shows the result of such measurements. One can see a very clear spectrum of the flux qubit indicated by the curved blue-red line. Interestingly, the signal sign of the qubit transition line changes from positive to negative when crossing the shifted half flux quantum point. It is possible to fit the given spectrum by the standard flux qubit theory

(the black dashed curve) for the following fitting parameters: critical current $I_c = 320$ nA, alpha factor $\alpha_q = 0.58$, ratio of charging and Josephson energies $E_J/E_C = 0.0034$. The correspondence between the theory and the experiment is good around the frustration point while a clear difference develops with larger detuning. This deviation might be also a result of strongly non-adiabatic interaction between the qubit and the fluxon.

The presented results on the strongly coupled Josephson vortex in the AJJ are not fully understood at the moment. As it was said, there is no proper theoretical description of strongly non-adiabatic perturbation and excitation of the flux qubit by the propagating fluxon. However, the experiment suggests that even in such a regime it is possible to readout the state of the qubit as demonstrated above.

4.2.3 Back-action

A back-action may be a serious problem for many experiments. Physically, it is a perturbation caused by the measurement set-up or a particular device to the system under test. This becomes especially important while dealing with quantum objects as quantum bits. Basically, it is impossible by the laws of quantum mechanics to acquire some knowledge about the coherent quantum state without destroying it or, at least, perturbing it in different ways. The ultimate goal in qubit experiments is to measure a given quantum bit with the minimum back-action.

Magnetic flux back-action

In the case of flux qubit inductively coupled to the fluxon oscillator, the back-action can be defined by the magnetic flux Φ_{ba} through the qubit loop which is created by the propagating Josephson vortex. First of all, let us consider the situation of the flux qubit coupled with the AJJ by the coupling loop as shown in Fig. 4.9. We consider that some part of the magnetic flux, produced by the Josephson vortex, couples to the superconducting loop and thus generates the screening current I_{CL}. This current is proportional to the part of the vortex flux caught by the coupling loop and inverse proportional to the geometric inductance of the coupling loop $I_{CL} = \Phi_{CL}/L_{CL}$. As there is no ground plane here,

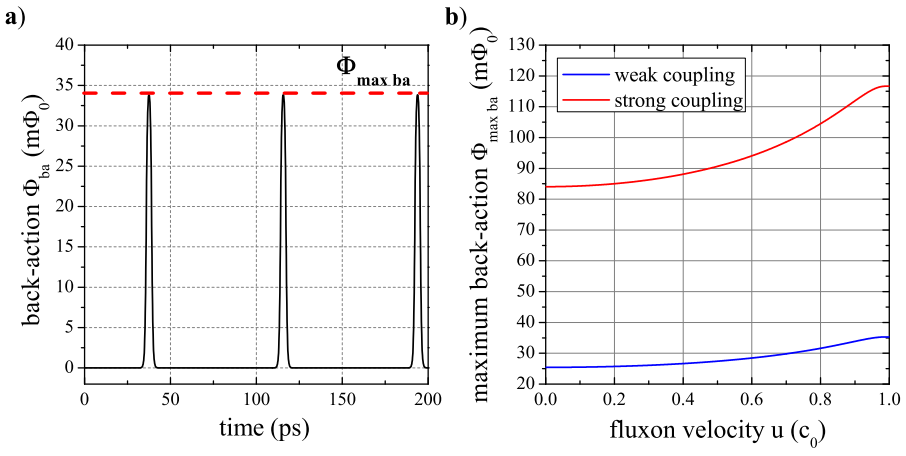

Figure 4.19: a) Time domain profile of magnetic flux through the qubit for the fluxon velocity $u = 0.9$. **b)** The dependence of a maximum back-action versus fluxon velocity. The backaction here is indicated in $\mathrm{m}\Phi_0 = 10^{-3} \cdot \Phi_0$.

our system is symmetric along the vertical axis perpendicular to the plane of the structure. To estimate Φ_{CL} we can make a reasonable simplification considering that half of the total flux generated by the fluxon goes through the coupling ring. These two assumptions allows one to estimate $\Phi_{CL} = \Phi_f/2$. Calculation of the fluxon generated magnetic flux inside the ring is straightforward and can be done using the fact that the spatial derivative of the Josephson phase defines the magnetic field component $\varphi_x = B$. The part of the fluxon which is "inside" the coupling ring ("inside" means here - between the electrodes in the top bias lead forming the coupling loop, see Fig. 4.1 or Fig. 4.9) creates magnetic flux equals to:

$$\Phi_f = A \int_0^l \varphi_x(x, v) dx, \tag{4.9}$$

where A is the constant of proportionality. Using the normalization condition:

$$\Phi_0 = A \int_{-\infty}^{+\infty} \varphi_x(x, v) dx, \tag{4.10}$$

we can find this constant to be $A = \Phi_0/\pi$. Thus, we know everything to estimate the screening current inside the coupling loop:

$$I_{CL} = \frac{\Phi_0}{2\pi L_{CL}}(\varphi(x+l,v) - \varphi(x,v)). \tag{4.11}$$

The last step is to calculate the back-action flux as $\Phi_{ba} = I_{CL}M$ where M is the mutual inductance between the coupling loop and the flux qubit. At the end, normalizing Φ_{ba} to the flux quantum Φ_0, the sought-for quantity takes the following form:

$$\Phi_{ba} = \frac{M}{2\pi L_{CL}}(\varphi(x+l,v) - \varphi(x,v)). \tag{4.12}$$

Now, one can, using FastHenry3 or any other program suitable for finite-element calculations of inductances, evaluate the mutual inductance M and the self-inductance L_{CL} and, then, calculate the total back-action of the propagating Josephson vortex to the flux qubit in terms of magnetic flux. Fig. 4.19 illustrates the magnetic back-action of the propagating fluxon to the flux qubit calculated with the use of (4.12). In the time domain, the fluxon creates spikes of magnetic flux through the qubit as shown in Fig. 4.19.a). A maximum height (maximum back-action flux) of these spikes can be used to define Φ_{maxba} and used further to study the dependence of Φ_{maxba} versus the fluxon velocity u. As follows from Fig. 4.19.a), the maximum back-action Φ_{maxba} grows with the fluxon velocity u and saturates when the latter approaches the Swihart velocity $u \to c_0$. Back-action saturates for higher velocities because once the fluxon magnetic profile shrinks less than the size of the dipole D (or, the width of the coupling loop), it transfers all its magnetic flux Φ_0 to the coupling loop. Obviously, the fluxon cannot generate flux greater than single flux quantum Φ_0.

Phase perturbation

Estimations of the back-action to the flux qubit in terms of magnetic flux is simple and straightforward, however, it gives us no information how fast the qubit loses its coherence due to this perturbation. To estimate this back-action coherence time, first of all, one needs to calculate the phase deviation of the qubit per one fluxon revolution in the AJJ.

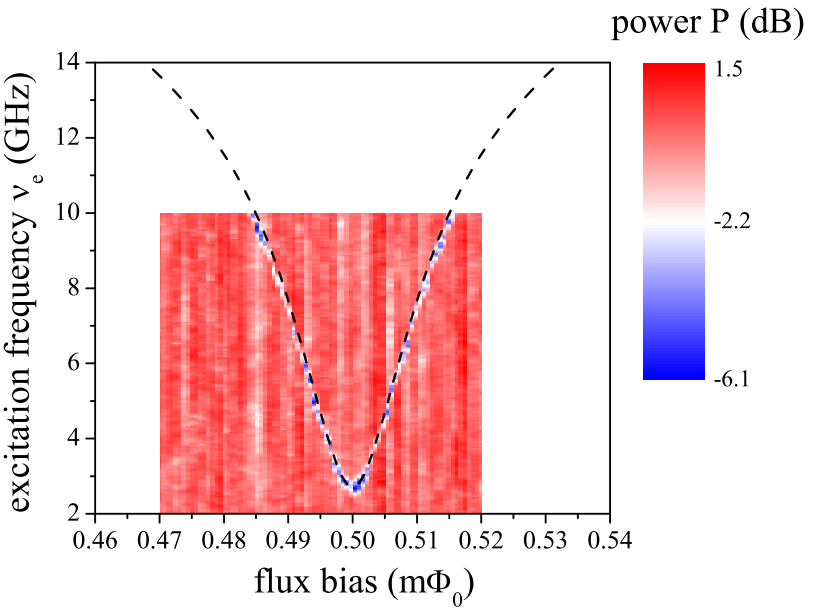

Figure 4.20: Measured flux qubit spectrum for the weakly coupled case (with the horizontal axis denoting the flux bias renormalized to Φ_0 units). Sample #2.

This phase shift can be defined as:

$$\delta\phi = \phi(t) - \phi_0 = \int_0^\tau \frac{E_{12}(t) - E_0}{\hbar} dt, \tag{4.13}$$

where $E_{12}(t)$ is the time-dependent (because of the fluxon back-action) energy splitting between the first excited and the ground states in the qubit, and E_0 is the energy difference in the unperturbed case. Generally, the fluxon magnetic back-action shifts the qubit working point by the amount of Φ_{ba}, thus changes $E_{12}(t)$ and introduces the certain phase perturbation $\delta\phi$ to the qubit state. The estimated maximum back-action flux Φ_{ba} is less than 35 mΦ_0 (for the weakly coupled case) and around 120 mΦ_0 (for the strongly coupled case). The magnetic backaction here is measured in m$\Phi_0 = 10^{-3} \cdot \Phi_0$. Assuming that all reasonable measurements of qubits have been made for the pretty large bias currents $\gamma > 0.2$, where the estimated fluxon velocities lie close to the Swi-

hart velocity $u \simeq c_0$, one can approximate integral $\int_0^\tau E_{12}(t)dt \simeq \tau \cdot E_s$, where E_s denotes a shifted by the amount of Φ_{maxba} working point of the flux qubit. This shifted energy can be simply estimated from the typical experimental spectrum of the flux qubit (see Fig. 4.20). The interaction time of the fluxon with the qubit is estimated to be of the order $\tau \sim 3$ ps in the experiment.

The total dephasing time per fluxon revolution is $\delta\phi \simeq 2 \cdot 10^{-3} \cdot 2\pi$ for the weak coupling and $\delta\phi \simeq 8 \cdot 10^{-2} \cdot 2\pi$ for the strong coupling. This means that the qubit dephasing time due to the fluxon back-action will be around $T_{ba} \simeq 35$ ns for the weak coupling, and $T_{ba} \simeq 8$ ns for the strong coupling.

Generally, these numbers on dephasing time are rather small. However, one should remember that the fluxon back-action can be easily improved by at least 2-3 orders of magnitude by simply scaling down the critical current density of the JTL and by increasing the length of the coupling loop (basically, putting the qubit farther away from the JTL), and, thus, the self-inductance of the coupling loop L_{CL}. Lowering the JTL's width W or decreasing the dipole length D, and increasing L_{CL} at the same time would also improve the back-action, leaving the signal strength of the fluxon readout at the same level.

Non-adiabatic excitations

Since the fluxon profile becomes abrupt for relativistic velocities $u \sim c_0$ (see Fig. 4.21.a)), it can potentially excite a qubit due to its non-adiabatic photon emission. In other words, the fluxon spectrum at high velocities broadens as its magnetic profile tends to an ideal delta-function (see Fig. 4.21.b)). However, the power of an emerging broad plato of non-adiabatic frequencies in Fig. 4.21.b) is relatively small in comparison with the power at fundamental fluxon frequency. The difference between them is at least 100 dB. The fluxon emitted power on the main frequency can be estimated as a product of the bias current and the voltage at the working point $P_f \simeq \alpha I_{bias} \cdot V$. As for the typical working point, $I_{bias} \sim 10$ mA, $V \sim 20$ μV and $\alpha \sim 0.02$, so the total emitted power per second is about $P_f \sim 4 \cdot 10^{-9}$ W. This roughly corresponds to 10^5 photons at the fundamental frequency of about 14 GHz

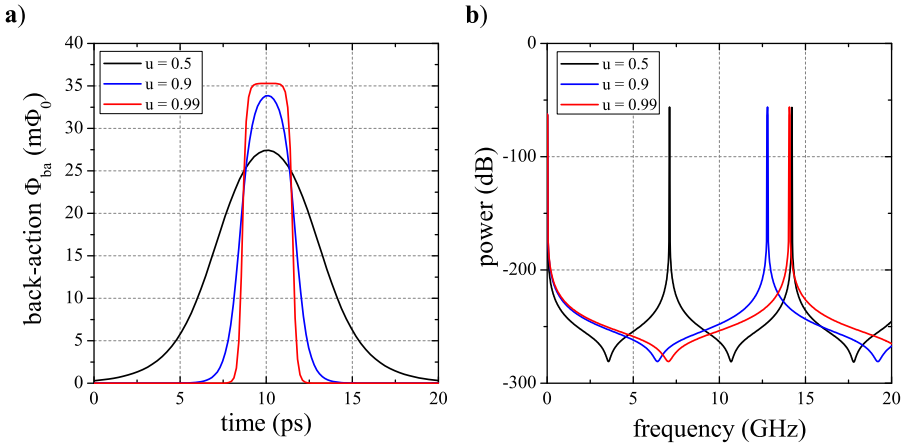

Figure 4.21: a) Lineshapes of fluxon magnetic back-action for different fluxon velocities u. Calculated with the use of (4.12). **b)** The results of a Fourier transformation of the periodic fluxon back-action on the flux qubit for different fluxon velocities u.

per fluxon revolution in the AJJ and leads to absence of non-adiabatic photons (as there is simply not enough power available to support their existence).

One should also take into account the inductive coupling strength k between the qubit and the fluxon. The latter typically decreases strongly with frequenc. So, non-adiabatic excitations at GHz frequencies should not happen (unless there are a lot of photons at the certain frequency - as it happens at the fluxon oscillation frequency ν_{fluxon}). Ultimately, the experimental spectra performed for fluxon velocities $u \sim 0.99 \cdot c_0$ (see Fig. 4.15,4.16,4.18) do not show any notable signs of non-adiabatic excitations.

In the future, it can be interesting to consider this problem in details, looking at the exact frequency dependent coupling between the fluxon and the qubit. This question contains not only a negative side of avoiding unwanted excitations but also can be useful, from the general point of view, for experimental studies of highly non-adiabatic interactions between the classical fluxons and the quantum bits. One can also try to use the oscillating fluxon in the AJJ as a microwave source to

manipulate the qubit.

4.3 Conclusions

In conclusion, we demonstrated the coupling of an oscillating single fluxon in an annular Josephson junction to a flux qubit. Using the possibility to detect the microwave radiation of the fluxon oscillations in the AJJ, we detected the fluxon frequency variations induced by the persistent current in the flux qubit coupled to the AJJ. We thus implemented a microwave generator controlled by the flux qubit. It was observed that the scattering of the fluxon on a current dipole can lead to acceleration of the fluxon, regardless of a dipole polarity. The perturbation theory and direct numerical simulations qualitatively well describe this phenomenon. The tested fluxon readout scheme is compatible with Rapid Single Flux Quantum (RSFQ) superconducting logic and can also be useful for applications where fast, weakly perturbing magnetic signal detection is needed.

The persistent current in the flux qubit was detected as a shift of the fluxon oscillation frequency. Resolution of the measurement scheme is high enough to measure transitions between quantum states as shown by the acquired energy spectrum of the flux qubit. The sensitivity of this readout can be significantly improved in various ways (and the fluxon back-action can be decreased), for instance, by lowering the critical current density j_c or decreasing the width W of the long Josephson junction, as both increase the current dipole strength and therefore the fluxon frequency shift. Our results prove the possibility of detecting quantum states by classical fluxons and, thus, open the way to applying RSFQ technique in the field of superconducting quantum computing.

Zusammenfassung und Ausblick

Diese Doktorarbeit präsentiert experimentelle Befunde zur Entwicklung eines neuen Auslesemechanismus von Fluss-Qubits mittels Fluxonen. Dieses basiert auf der Detektion von ausgesandten Mikrowellen eines Fluxons, welches sich in einem ringförmigen Josephson-Kontakt (RJK) bewegt. Die Resonanzfrequenz zeigt dabei eine charakteristische Abhängigkeit vom Ruhestrom durch den Kontakt, die so genannte resonante Nullfeldstufe. Die erreichte Präzision übersteigt die von der direkten Spannungsmessung um einige Ordnungen und erlaubt es ohne weiteres, die Feinstruktur der Nullfeldstufen aufzulösen. Des Weiteren liefert der hier beschriebene Ansatz auch die Möglichkeit zur Untersuchung faszinierender, nicht-linearer Dynamik des getriebenen Fluxons im RJK bei Benutzung konvertioneller Mikrowellenmethoden, wie die Phasenregeltechnik, die Resonanzbreite und die Phasenrauschenuntersuchungen (Kapitel 3). Uns ist es gelungen, das System von ungewollten Rauschen und Fluktuationen zu befreien und das Ziel, das als Stromdipol gekoppelte, supraleitende Flussqubit auszulesen, zu realisieren (Kapitel 4).

Analytische und numerische Untersuchungen an einem entsprechenden Modell des zirkulierenden Fluxons im RJK in der Gegenwart eines Stromdipols haben viele unerwartete und nicht offensichtliche Resultate offenbart. Wie in Kapitel 4 beschrieben, kann eine Streuung eines Fluxons an einem Stromdipol dazu führen, dass dieses beschleunigt wird. Zusätzlich stellt sich heraus, dass das Fluxonverhalten bei einem großen Ruhestrom nicht von der Polarität des Dipols abhängt. Numerische Simulationen und die Analyse der Störungstheorie basierend auf der gestörten Sine-Gordon-Gleichung beschreiben dieses Phänomen nicht nur theoretisch sehr gut, sondern stimmen auch quantitativ mit den gemessenen Daten überein.

Mittels der Detektierung der ausgesandten Mikrowellen des zirkulieren-

den Fluxons im RJK wurde auch die resonante Anregung des gekoppelten Flussqubit untersucht. Das Qubitspektrum in Abhängigkeit vom angelegten Fluss wurde durch die gemessene Frequenzänderung des Fluxons aufgezeichnet. Einer der größten Vorteile des hier beschriebenen Systems ist seine Kompatibilität mit der supraleitenden, digitalen RSFQ-Logik (rapid singlefluxquantum), die möglicherweise in zukünftigen Quantencomputern eine wesentliche Rolle spielen könnte. Die potentiell hohe Zeitauflösung des Qubitauslesens und die Möglichkeit, das Fluxon als eine lokale Mikrowellenquelle zur Steuerung des Qubits zu nutzen, sind dabei auch von großem Interesse, wenn auch diese Anwendungen noch weitere Forschung erfordern.

Als die Herausfordernen des Qubitauslesens erwiesen sich die relativ hohe Wärmeentwicklung und die nicht zu vernachlässigende Rückkopplung an das Qubit. Allerdings gibt es auch viele Ansätze für Verbesserungen. Die Naheliegenden sind die Reduzierung der kritischen Stromdichte des RJK und die Vergröerung des Abstandes zwischen dem Qubit und dem RJK, dass sowohldie Erwärmung als auch die Rückkopplung unterdrückt. Andere Mölichkeiten wären die Verkleinerung der Lateralachse des RJK oder die Verwendung eines Wellenleiters bestehend aus vielen diskreten Josephson-Kontakten anstelle eines Kontinuierlichen wie in diesem Experiment.

Man muss auch anmerken, dass unsere Fluxonen eher dem klassischen als dem Quantenbereich zuzuordnen sind. Die Verwendung desFluxonsals quantenmechanisches System zur kohärenten Wechselwirkung mit oder sogar als Qubits, wie theoretisch [KI96, KWU02] und auch experimentell [WLU03, PKU10] beschrieben, ist eines der aufregendsten und herausforderndsten zukünftigen Projekte.

Conclusion and Outlook

This thesis presents experimental studies on developing of a novel fluxon readout for superconducting flux qubits. It includes an experimental scheme for detecting the microwave radiation of an oscillating fluxon in an annular Josephson junction and, thus, recovering a characteristic dependence of fluxon frequency versus bias current, a so-called resonant zero-field step. The precision of this approach is many orders of magnitude higher than the precision of direct voltage measurements and allows one to easily resolve a hidden fine structure of the zero-field steps. At the same time, the given approach provides an opportunity to study the fascinating nonlinear dynamics of the driven fluxon in the annular Josephson junction (AJJ) using various techniques typical for radio-electronics: the phase-locking technique, the radiation linewidth and the phase-noise studies (Chapter 3). Altogether, these studies allowed one to rectify the system from the unwanted noise and fluctuations and perform the sought-for fluxon readout scheme for a superconducting flux qubit coupled as a current dipole to the annular Josephson junction (Chapter 4).

Analytical and numerical studies of a toy model of the oscillating fluxon in the AJJ in the presence of the fixed current dipole showed several highly unexpected and nontrivial results. As it was shown in Chapter 4, the scattering of the fluxon on a current dipole can lead to an acceleration of the fluxon. Additionally, for high bias currents the fluxon response turns out not to depend on the dipole polarity. A perturbation theory based on the perturbed sine-Gordon equation and direct numerical simulations of the latter qualitatively well describe this phenomenon. The experimental data are in a good agreement with the theoretical predictions.

By means of detection of the fluxon oscillating frequency in the AJJ coupled to the flux qubit, a resonant excitation of the latter was in-

vestigated. A spectrum of the flux qubit was measured via detecting a frequency shift of the fluxon oscillations versus a flux bias through the qubit. The major advantage of the used scheme is its compatibility with the Rapid Single Flux Quantum (RSFQ) superconducting digital logic which can be useful for large scale quantum computers in the future. A potential high-time resolution of the fluxon readout and possibilities to use the fluxon as a local microwave drive for the qubit are also of the interest, though, they require additional experimental improvements.

One of the main drawbacks of the given readout is its relatively large heating and a notable back-action on the measured flux qubit. However, there is plenty of room for battling these problems. The most straightforward way to do this is to reduce the critical current density of the annular Josephson junction and increase the distance between the qubit and the AJJ, lowering the heating and the back-action at the same time. Other ways can be implemented via reducing a lateral width of the AJJ or switching to discrete Josephson transmission lines instead of the continuous ones used in the presented experiments.

It is worth noting that the fluxon readout in our experiments was operated in the classical rather than quantum regime. Employing fluxons to interact with or act as qubits in the quantum regime, as discussed theoretically [KI96, KWU02] and also detected experimentally [WLU03, PKU10], would be very exciting and challenging in the future.

References

[AB63] V. Ambegaokar, A. Baratoff, *Tunneling between superconductors*, Phys. Rev. Lett. **10**, 468 (1963).

[And10] S. Anders et al., *European roadmap on superconductive electronics - status and perspectives*, Physica C **470**, 2079-2126 (2010).

[AR63] P.W. Anderson, J.W. Rowell, *Probable observation of Josephson superconducting tunneling effect*, Phys. Rev. Lett. **10**, 230-232 (1963).

[ARS06] D.V. Averin, K. Rabenstein, and V.K. Semenov, *Rapid ballistic readout for flux qubits*, Phys. Rev. B **73**, 094504 (2006).

[BAZ00] P. Binder, D. Abraimov, A.V. Ustinov, S. Flach, Y. Zolotaryuk, *Observation of breathers in Josephson ladders*, Phys. Rev. Lett. **84**, 745-748 (2000).

[BCS57] J. Bardeen, L.N. Cooper, J.R. Schrieffer, *Microscopic Theory of Superconductivity*, Phys. Rev. **106**, 162-164 (1957).

[BMU96] P. Barbara, R. Monaco, A.V. Ustinov, *Model for the fine structure of zero field steps in long Josephson tunnel junctions and its comparison with experiment*, Jour. of Appl. Phys. **79**, 327-333 (1996).

[BP82] A. Barone and G. Paterno, *Physics and Applications of the Josephson effect*, J. Wiley (1982).

[CFL72] J.T. Chen, T.F. Finnegan, D.N. Langenberg, *Anomalous DC current singularities in Josephson tunnel junctions Physica* **55**, 413-420 (1972).

[CL72] J.T. Chen, D.N. Langenberg, *Fine structure in the anomalous d.c. current singularities of a Josephson tunnel junction*, *LT 13* **3**, 289-292 (1972).

[CRL99] W. Chen, A.V. Rylyakov, V. Patel, J.E. Lukens, K.K. Likharev, *Rapid single flux quantum T-flip flop operating up to 770 GHz*, IEEE Trans. Appl. Supercond. **9**, 3212-3215 (1999).

[CNM03] I. Chiorescu, Y. Nakamura, C.J.P.M. Harmans, and J.E. Mooij, *Coherent quantum dynamics of a superconducting flux qubit* Science **299**, 1869 (2003).

[CW08] J. Clarke, F.K. Wilhelm, *Superconducting quantum bits*, Nature **453**, 1031-1042 (2008).

[DiV00] D.P. DiVincenzo *The physical implementation of quantum computation*, Fortschritte der Physik **48**, 771 (2000), `http://arxiv.org/abs/quant-ph/0002077`.

[DJ89] P.G. Drazin, R.S. Johnson, *Solitons: an introduction*, Cambridge University Press (1989).

[Dol77] G.J. Dolan, *Offset masks for lift-off photoprocessing*, Appl. Phys. Lett. **31**, 337 (1977).

[FD73] T.A. Fulton, R.C. Dynes, *Single vortex propagation in Josephson tunnel junctions*, Solid St. Commun. **12**, 57-61 (1973).

[Fey82] R.P. Feynman, *Simulating physics with computers*, Int. J. Theor. Phys. **21**, 467Ů488 (1982).

[FF] `http://www.ipht-jena.de`.

[Fis64] M. D. Fiske, *Temperature + magnetic field dependeces of Josephson tunneling supercurrent*, Rev. Mod. Phys. **36**, 221 (1964).

[FLS65] R.P. Feynman, R.B. Leighton, and M. Sands, *The Feyman Lectures on Physics* Vol.**3**, Chap.21 Addison-Wesley, (1965).

[FPT73] C.M. Falco, W.H. Parker, S.E. Trulling Observation of a phase-modulated quasiparticle current in superconducting weak links, Phys. Rev. Lett. **31**, 933-936 (1973).

[Fri44] H.T. Friis, *Noise Figures of Radio Receivers*, Proceedings of the IRE **32**, 419Ű422 (1944).

[Gar05] F.M. Gardner, *Phaselock techniques*, Wiley (2005).

[GSK04] E. Goldobin, N. Stefankis, D. Koelle, R. Kleiner, *Fluxon-semifluxon interaction in an annular long Josephson 0-pi junction*, Phys. Rev. B. **70**, 094520 (2004).

[HFS07] A. Herr, A. Fedorov, A. Schnirman, E. Il'ichev, and G. Schon, *Design of a ballistic fluxon qubit readout*, Supercond. Sci. and Tech. **20**, S450 (2007).

[Hug04] R. Hughes et al., *A quantum information science and technology roadmap*, `http://qist.lanl.gov/qcomp_map.shtml` (2004).

[Hyp] `www.hypres.com`.

[Il'02] E. Il'ichev et al., *Characterization of superconducting structures designed for qubit realizations*, Appl. Phys. Lett. **80**, 4184-4186 (2002).

[Joe82] E. Joergensen et al., *Thermal fluctuations in resonant motion of fluxons on a Josephson transmission line: theory and experiment*, Phys. Rev. Lett. **49**, 1093 (1982).

[Jos62] B.D. Josephson, *Possible new effects in superconductive tunnelling*, Phys. Lett. **1**, 251-253 (1962).

[JPU12] M. Jerger, S. Poletto, P. Macha, U. Hüner, E. Il'ichev, A. V. Ustinov, *Frequency division multiplexing readout and simultaneous manipulation of an array of flux qubits*, Appl. Phys. Lett. **101**, 042604 (2012).

[KI96] T. Kato, M. Imada, *Macroscopic quantum tunneling of a fluxon in a long Josephson junction*, J. Phys. Soc. Jpn. **65**, 2963-2975 (1996).

[KS00] V.P. Koshelets, S.V. Shitov, *Integrated superconducting receivers*, Super. Sci. Tech. **13**, R53-R69 (2000).

[KV05] D.E. Kirichenko, I.V. Vernik, *High quality on-chip long annular Josephson junction clock source for digital superconducting electronics* IEEE Trans. Appl. Supercond. **15**, 296-299 (2005).

[KWU02] A. Kemp, A. Wallraff, A.V. Ustinov, *Josephson vortex qubit: design, preparation and read-out*, Phys. Stat. Sol. (b) **233**, 472-478 (2002).

[KYV98] V.V. Kurin, A.V. Yulin, I.A. Shereshevskii, N.K. Vdovicheva, *Cherenkov radiation of vortices in a two-dimensional annular Josephson junction*, Phys. Rev. Lett. **80**, 3372-3375 (1998).

[Lik12] K.K. Likharev, *Superconductor digital electronics*, Physica C **482**, 6-18 (2012).

[Lik86] K.K. Likharev, *Dynamics of Josephson junctions and circuits*, Gordon and Breach (1986).

[LU08] A. Lukashenko, A.V. Ustinov, *Improved powder filters for qubit measurements*, Rev. Sci. Instr. **79**, 014701 (2008).

[MAK08] R. Monaco, M. Aaroe, J. Mygind, R.J. Rivers, V.P. Koshelets, *Spontaneous fluxon production in annular Josephson tunnel junctions in the presence of a magnetic field*, Phys. Rev. B **77**, 054509 (2008).

[Mar09] J.M. Martinis, *Superconducting phase qubits*, Quantum Inf. Process. **8**, 81-103 (2009).

[MBM93] R. Monaco, P. Barbara, J. Mygind, *Fine structures on zero-field steps in low-loss Josephson tunnel-junctions*, Phys. Rev. B **47**, 12292-12295 (1993).

[MMF98] N. Martucciello, J. Mygind, V.P. Koshelets, A.V. Shchukin, L.V. Filippenko, *Fluxon dynamics in long annular Josephson tunnel junctions*, Phys. Rev. B **57**, 5444-5449 (1998).

[Moo99] J.E. Mooij et al., *Josephson persistent-current qubit*, Science **285**, 1036 (1999).

[MS79] G.S. Mkrtchyan, V.V. Shmidt, *On the radiation from inhomoheneous Josephson junction*, Solid St. Commun. **30**, 791-793 (1979).

[MS78] D.W. McLaughlin and A.C. Scott, *Perturbation analysis of fluxon dynamics*, Phys. Rev. A **18**, 1652-1680 (1978).

[MMS01] Y. Makhlin, G. Schön, A. Shnirman, *Quantum-state engineering with Josephson-junction devices*, Rev. Mod. Phys. **73**, 357-400 (2001).

[MU04] B.A. Malomed, A.V. Ustinov, *Creation of classical and quantum fluxons by a current dipole in a long Josephson junction*, Phys. Rev. B **69**, 064502 (2004).

[NPT99] Y. Nakamura, Y.A. Pashkin, J.S. Tsai, *Coherent control of macroscopic quantum states in a single-Cooper-pair box*, Nature **398**, 786-788 (1999).

[Nyq28] H. Nyquist, *Thermal activation of electric charge in conductors*, Phys. Rev. **32**, 110 (1928).

[Orl99] T.P. Orlando et al., *Superconducting persistent-current qubit*, Phys. Rev. B **60**, 15398-15413 (1999).

[PAU08] J. Pfeiffer, A.A. Abdumalikov, M. Schuster, A.V. Ustinov, *Resonances between fluxons and plasma waves in underdamped Josephson transmission lines of stripline geometry*, Phys. Rev. B **77**, 024511 (2008).

[PFL72] N.F. Pedersen, T.F. Finnegan, D.N. Langenberg, *Magnetic field dependence and Q of the Josephson plasma resonance*, Phys. Rev. B **6**, 4151-4159 (1972).

[PKU10] A.N. Price, A. Kemp, D.R. Gulevich, F.V. Kusmartsev, A.V. Ustinov, *Vortex qubit based on an annular Josephson junction containing a microshort*, *Phys. Rev. B* **81**, 014506 (2010).

[PTF07] W.H. Press, S.A. Teukolsky, W.T. Vetterling, B.P. Flannery, *Numerical recipes: the art of scientific computing*, Cambridge University Press (2007).

[Raj82] R. Rajaraman, *Solitons and instantons*, North Holland, New York (1982).

[RGS12] C. Rigetti, J. M. Gambetta, S. Poletto, B.L.T. Plourde, J.M. Chow, A.D. Córcoles, J.A. Smolin, S.T. Merkel, J. R. Rozen, George A. Keefe, M.B. Rothwell, M.B. Ketchen, M. Steffen, *Superconducting qubit in a waveguide cavity with a coherence time approaching 0.1 ms*, Phys. Rev. B **86**, 100506 (2012).

[Ryt88] S.M. Rytov, *Introduction to statistical radiophysics*, Springer (1988).

[SA03] V.K. Semenov, D.V. Averin, *SFQ control circuits for Josephson junction qubits*, IEEE Trans. Appl. Supercond. **13**, 960 (2003).

[Say01] C. Sayrin et al„ *Real-time quantum feedback prepares and stabilizes photon number states* Nature **477**, 73 (2011).

[Sch97] V.V. Schmidt, *The physics of superconductors*, Springer Berlin (1997).

[Sho97] P. Shor, *Polynomial-time algorithms for prime factorization and discrete logarithms on a quantum computer*, SIAM J. Comput. **26**, 1484-1509 (1997).

[Sim49] R.N. Simons, *Coplanar waveguide circuits, components and systems*, Wiley (1949).

[SVD06] I. Siddiqi, R. Vijay, M. Metcalfe, E. Boaknin, L. Frunzio, R.J. Schoelkopf, M.H. Devoret, *Dispersive measurements of superconducting qubit coherence with a fast latching readout*, Phys. Rev. B **73**, 054510 (2006).

[Swi61] J.C. Swihart, *Field solution for a thin-film superconducting strip transmission line* J. Appl. Phys. **32**, 461 (1961).

[Tin75] M. Tinkham, *Introduction to superconductivity*, McGraw-Hill (1975).

[UMG99] A.V. Ustinov, B.A. Malomed, E. Goldobin, *Backbending current-voltage characteristic for an annular Josephson junction in a magnetic field*, Phys. Rev. B **60**, 1365-1371 (1999).

[Ust02] A.V. Ustinov, *Fluxon insertion into annular Josephson junctions*, Appl. Phys. Lett. **80**, 3153 (2002).

[UstNP] A.V. Ustinov, *Solitons in Josephson junctions*, unpublished book.

[Vij12] R. Vijay et al., *Stabilizing Rabi oscillations in a superconducting qubit using quantum feedback*, Nature **490**, 77-80 (2012).

[VSC01] L.M. Vandersypen, M. Steffen, G. Breyta, C.S. Yannoni, M.H. Sherwood, I.L. Chuang, *Experimental realization of Shor's quantum factoring algorithm using nuclear magnetic resonance*, Nature **414**, 883-887 (2001).

[Whi87] G.K. White, *Experimental techniques in low-temperature physics*, Oxford University Press (1987).

[WLU03] A. Wallraff, A. Lukashenko, J. Lisenfield, A. Kemp, M.V. Fistul, Y. Koval, A.V. Ustinov, *Quantum dynamics of a single vortex*, Nature **425**, 155 (2003).

[WSS05] A. Wallraff, D.I. Schuster, A. Blais, L. Frunzio, J. Majer, M.H. Devoret, S.M. Girvin, R.J. Schoelkopf, *Approaching unit visibility for control of a superconducting qubit with dispersive readout*, Phys. Rev. Lett. **95**, 060501 (2005).

[WUV00] A. Wallraff, A.V. Ustinov, V.V. Kurin, I.A. Shereshevsky, N.K. Vdovicheva, *Whispering vortices*, Phys. Rev. Lett. **84**, 151-154 (2000).

[YN05] J.Q. You, F. Nori, *Superconducting circuits and quantum Information*, Phys. Today **58**, 42-47 (2005).

[Zha91] Y. Zhang, Ph.D. thesis, Chalmers University of Technology, (1991).

List of publications

[FP07a] K.G Fedorov, A.L. Pankratov, *Influence of fluctuations on the dynamic properties of distributed Josephson junctions*, J. Commun. Technol. El.+ **7**, 114-118 (2007).

[FP07b] K.G Fedorov, A.L. Pankratov, *Mean time of the thermal escape in a current-biased long-overlap Josephson junction*, Phys. Rev. B **76**, 024504 (2007).

[FPS08] K.G Fedorov, A.L. Pankratov, B. Spagnolo, *Influence of length on the noise delayed switching of long Josephson junctions*, Int. J. Bifurcat. Chaos **18**, 2857Ű2862 (2008).

[FP09] K.G Fedorov, A.L. Pankratov, *Crossover of the Thermal Escape Problem in Annular Spatially Distributed Systems*, Phys. Rev. Lett. **103**, 260601 (2009).

[FFU11] K.G Fedorov, M.V. Fistul, A.V. Ustinov, *Pinning of charge and flux solitons in disordered Josephson junction arrays*, Phys. Rev. B **84**, 014526 (2011).

[FSU12a] K.G Fedorov, S.V. Shitov, H. Rotzinger, A.V. Ustinov, *Non-reciprocal microwave transmission through a long Josephson junction*, Phys. Rev. B **85**, 184512 (2012).

[FSU12b] K.G. Fedorov, A. Shcherbakova, R. Schäfer, A.V. Ustinov, *Josephson vortex coupled to a flux qubit*, Appl. Phys. Lett. **102**, 132602 (2013).

[FSU13] K.G. Fedorov, A. Shcherbakova, M.J. Wolf, D. Beckmann, A.V. Ustinov, *Fluxon readout of a superconducting qubit*, Preprint at `http://arxiv.org/abs/1304.0645`.